Nonlinear Wave-Wave Interactions in the Brain

A thesis submitted for the degree of
Doctor of Philosophy

by

Mariya Ferdousi

School of Physics
University of Sydney
Australia

July 2019

Declaration of originality

To the best of my knowledge, this thesis contains no copy or paraphrase of work published by another person, except where duly acknowledged in the text. This thesis contains no material which has been presented for a degree at the University of Sydney or any other university.

Mariya Ferdousi

Included papers and attribution

Listed below are details of the papers on which Chapters 2−3 are based.

Chapter 2 **Nonlinear harmonic generation in the corticothalamic system**
M. Ferdousi, T. Babaie Janvier, and P. A. Robinson,
Published in *Journal of Theoretical Biology*, 2018.

I was primarily responsible for this work, with an overall contribution of about 80%.

Chapter 3 **Nonlinear Wave-Wave Interactions in the Brain**
M. Ferdousi, T. Babaie-Janvier, and P. A. Robinson,
Submitted to *Journal of Theoretical Biology*, 2019.

I was primarily responsible for this work, with an overall contribution of about 80%.

Some of the results of this thesis were presented or accepted for the presentation at the following conferences:

Nonlinear Wave Interactions in the Corticothalamic System
M. Ferdousi, T. Babaie-Janvier, and P. A. Robinson,
Presented at the *11th Australasian Workshop on Neuro-Engineering and Computational Neuroscience*, Sydney 2018.

Nonlinear Wave Interactions in the Brain
M. Ferdousi, T. Babaie-Janvier, and P. A. Robinson,
Presented at the *School of Physics Symposium, University of Sydney*, Sydney 2018.

Nonlinear Harmonic Generation and Wave-Wave Interactions in the Brain
M. Ferdousi, T. Babaie-Janvier, and P. A. Robinson,
Presented at the *Organization for Human Brain Mapping (OHBM)*, Vancouver 2017.

Nonlinear Harmonic Generation and Wave-Wave Interactions in the Brain
M. Ferdousi, T. Babaie-Janvier, and P. A. Robinson,
Presented at the *Brain and Mind Centre Symposium*, Sydney 2017.

Acknowledgements

I would first and foremost like to thank my supervisor Peter Robinson for his guidance, care, patience, and support throughout my PhD candidature; without him this work would not have been possible. His strong support throughout the years has played a large role in bringing this thesis to completion and I am grateful to have had the opportunity to work with such a motivating supervisor. I would also like to thank my auxiliary supervisor, Tahereh Janvier-Babaie for her guidance and discussion in my projects. I would like to thank Svetlana Postnova and Paula Sanz-Leon for helping me in MATLAB course, Romesh Abeysuriya and James Roberts for discussion in my research project.

I am thankful to the entire complex system group for their support during my thesis. I would also like to thank my colleagues Guozhang, Yuxi, Brandon, Marilia, Mukta apu, Kevin, Nipa apu, Tara, and Xian. I also would like to thank Cindy for her help and care from the beginning of my PhD to the end.

During my PhD program, I was financially supported by an Australian Research Council Laureate Fellowship, Postgraduate Research Support Scheme (PRSS), and a yearly top-up from the Center for Integrative Brain Function, all of which helped to provide facilities for my work.

I would like to thank my entire family for giving me continuous support and I am grateful to my beloved father, mother, Nihad apu, Mushira, Rabu viya, Yusuf, Shayla Apu, and my grandmother. Thank you to my all friends, relatives, and housemates (Specially Anindita apu, Nitu, Linta, Nastaran) who have supported me in so many ways. Special thanks go to Deeba apu (she was always with me and till now she give me support in any situation), Samira apu, Rumi apu, Sohel, Saima, Farhan for their affection, and inspiration during these years in Sydney. I would not have made it to this point without them.

Finally, I would like to thank Almighty Allah for giving me the opportunity to finish my thesis, Alhamdulillah.

Abstract

The brain is a complex system that exhibits linear and nonlinear dynamics at different timescales. On length scales of a few tenths of a millimeter to the entire brain, neural field theory (NFT) is a physiologically based established model of brain activity that has successfully reproduced many features of linear and nonlinear brain dynamics such as those measured with electroencephalography (EEG) and steady state visually evoked potentials (SSVEPs) on EEG. In this thesis we use a neural field model of the cortex and thalamus to study a range of linear and nonlinear brain dynamics, particularly wave-wave interactions and harmonic generation in large scale brain activity.

Chapter 1 introduces the relevant physiological background of the brain dynamics, brain and neuron structure, methods of measuring brain activity, an overview of brain modeling with particular focus on the neural field model used in this study, and nonlinear activity in the brain.

Chapter 2 focuses on deriving the nonlinear power spectrum and analyzing nonlinear contribution in normal sleep and wake states. The nonlinear power spectrum is analytically calculated by convolving the linear power spectrum with itself and other factors. Our neural field model verified strong nonlinear effects during normal brain activity such as sleep spindles, where the strongest nonlinearities arise in the thalamic relay nuclei, which validates the prior prediction in this brain state. Nonlinearities in alpha and beta peaks have long been debated and our analysis finds significant nonlinear contributions of 55% and 46% at the alpha and beta peaks, respectively in the power spectrum for typical parameters.

Chapter 3 explores the nonlinear dynamics in steady state visual evoked potentials (SSVEPs) that exhibits wave-wave processes such as harmonic and subharmonic generation, wave-wave coupling, entrainment, and generation of sum and difference frequencies due to wave-wave coalescence and decay. Two

sine drives are employed in SSVEPs to analyze the driven nonlinear dynamics more clearly, without the complicating effects of a background spectrum. The nonlinear power spectrum for a driven system is calculated analytically. The theory predicts an approximately quadratic relationship of the power in the fundamental peak to the amplitude of the periodic stimuli. The power scaling of sharp, dominant peaks is found to be consistent with the quadratic scaling prediction made by the theory.

A brief summary of the thesis and the possibilities for future work are provided in Chapter 4.

Contents

Chapter 1

Introduction

The brain, the most complex organ in the body, is a dynamic system that displays linear and nonlinear dynamics from macroscale to microscale. To understand brain activity, it is required to study physiological dynamics, structural and functional integration of the brain. The focus of this thesis is to understand nonlinear brain phenomena, particularly wave-wave interactions and harmonic generation in large scale brain activity by using a physiologically based corticothalamic model.

This chapter presents an overview of the background material needed to understand the modeling work in this thesis. Section 1.1 provides a brief overview of the relevant parts of the brain. Then Sec. 1.2 describes methods for measuring brain activity. Section 1.3 outlines the models of brain activity. Section 1.4 discusses linear and nonlinear brain activity and nonlinear applications.

1.1 Physical aspects of the brain

This section presents a brief overview of major regions of the brain in Sec. 1.1.1 and discusses the detailed structure of a neuron along with its functions and properties in Sec. 1.1.2.

1.1.1 Brain Structure: large-scale

The brain, together with the spinal cord, forms the central nervous system (CNS). The general structure of the brain includes the forebrain (prosencephalon),

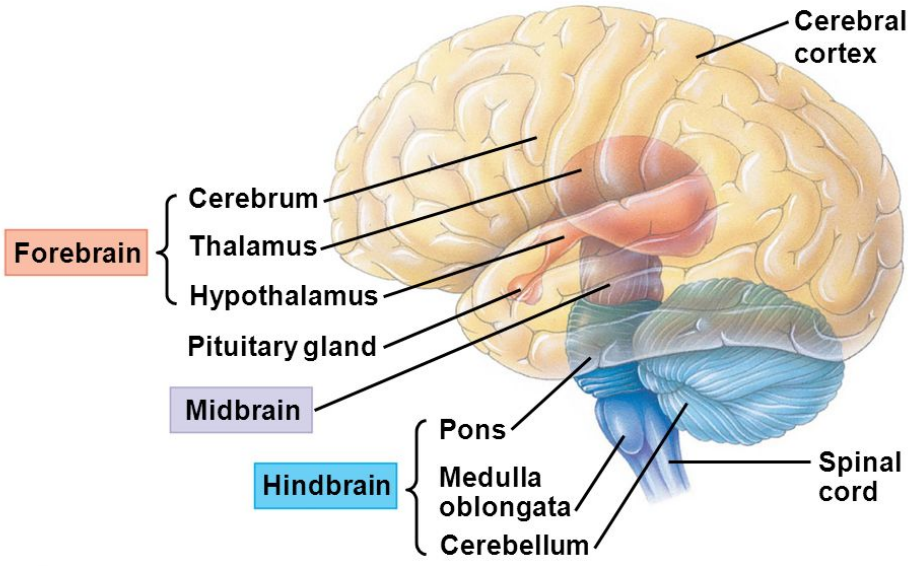

Figure 1.1: Major regions of the brain, showing the forebrain, midbrain, and hindbrain. Image adapted from http://geoface.info/fabe/e5578cdb87b3/central-and-peripheral-nervous-sys-d46636.

which includes the cerebral cortex and diencephalon; the midbrain (mesencephalon), which contains the tectum and tegmentum; and the hindbrain (rhombencephalon), which contains the medulla, pons, and cerebellum (Haines, 2006, Kandel et al., 2000, Nolte, 2009) as seen in Fig. 1.1.

The cerebrum is the largest part of the brain and consists of two hemispheres connected by a large bundle of neural fibers called the corpus callosum (Kandel et al., 2000). Each hemisphere contains: basal nuclei, which participate in regulating motor performance; gray matter, which contains the majority of neural cell bodies, and white matter which is composed of myelinated axons that connect neuronal populations (Kandel et al., 2000).

The cerebral cortex is the outer layer of the cerebrum as shown in Fig. 1.1 with a thickness of $2-4$ mm and a six-layered structure (Kandel et al., 2000, Mignard and Malpeli, 1991). Each layer of the neocortex is distinguishable by its histology, which in turn reflects its anatomical organization (Kandel et al., 2000). The cerebral cortex plays an important role in information processing,

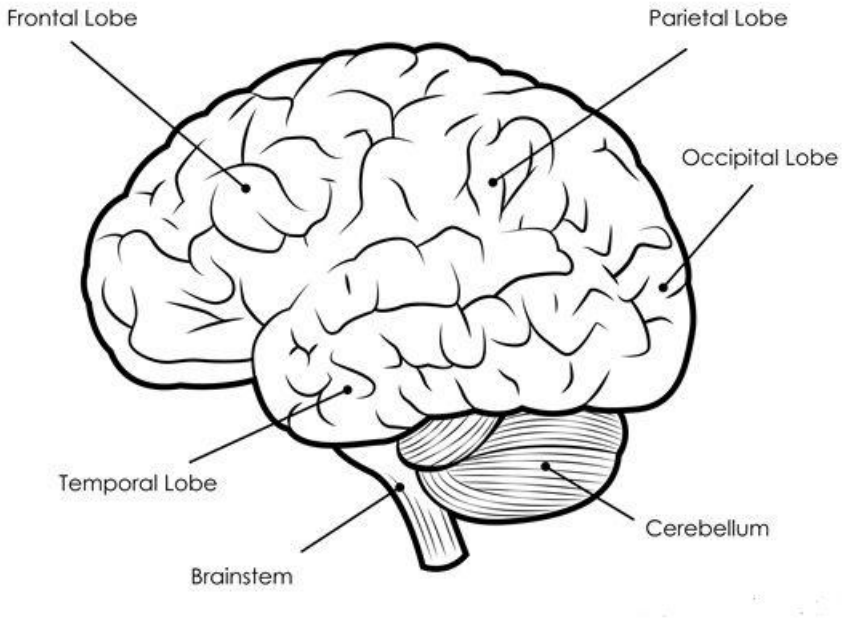

Figure 1.2: The four lobes of the cerebral cortex: frontal, parietal, temporal, and occipital lobes. Image adapted from https://www.timvandevall.com/science/human-brain-diagram.

language processing, and decision making in the brain.

The cerebral cortex is divided into four lobes: frontal, parietal, temporal, and occipital as shown in Fig. 1.2. Each lobe has specific tasks and receives different kinds of inputs from the periphery and specific regions of the CNS (Siegel and Sapru, 2006). The frontal lobe, at the top of the brain, is associated with thinking, learning, and control of movement (Kandel et al., 2000, Purves et al., 2012). The parietal lobe, located behind the frontal lobe, is involved with general sensation, feeling, forming a body image, and relation of the body image to extrapersonal space (Kandel et al., 2000, Purves et al., 2012). The temporal lobe, located at the bottom of the cortex, is involved in auditory processing, while the occipital lobe, at the back of the brain, processes visual information (Kandel et al., 2000, Purves et al., 2012).

The diencephalon lies near the center of the brain and contains the hypothalamus and the thalamus (as seen in Fig. 1.1), both of which consist of groups of

smaller nuclei (Kandel et al., 2000, Nolte, 2009). The hypothalamus is the bridge between the endocrine system and nervous system and plays key roles in many important functions of the body such as the body temperature, the sleep-wake cycle, and the circadian rhythm (Afifi and Bergman, 2005, Kandel et al., 2000, Nolte, 2009). It also plays an important role in the hormonal balance of the body by governing the release of hormones (e.g., oxytocin, somatostatin) into the bloodstream (Haines, 2006, Nolte, 2009).

The thalamus is surrounded by the thalamic reticular nucleus, which is a thin sheet of neurons whose primary role is to inhibit neural activity in the thalamus. The thalamus acts as a relay for sensory input (excluding olfaction) and signals related to motor function and is thus critical for the interaction of the brain with the outside world (Kandel et al., 2000, Nolte, 2009, Purves et al., 2012). The ascending thalamocortical projections send sensory information to the cortex, and the descending corticothalamic projections return feedback to the thalamus (Afifi and Bergman, 2005). Thus the thalamus and its incoming and outgoing projections play an important role in preprocessing sensory information.

The cone-shaped part of the brain connected to the spinal cord is the medulla (as shown in Fig. 1.1). The pons, above the medulla, conveys information about movement and sensation from cerebrum to cerebellum. The midbrain, pons, and medulla are referred to together as the brainstem which is continuous rostrally to the diencephalon, while caudally it is continuous with the spinal cord. It is responsible for essential functions such as respiration, digestion, regulating body temperature, hormone levels, sleep, relay of motor, and sensory information to and from the spinal cord (Kandel et al., 2000, Nolte, 2009, Purves et al., 2012).

Above the brainstem is the cerebellum (also shown in Fig. 1.1) which is a dense body of cells at the back of the brain, containing more nerve cells than the rest of the brain combined. It is highly specialized, with coordination of fine motor control being its primary function (Kandel et al., 2000, Nolte, 2009, Purves et al., 2012).

1.1.2 Structure and activity of neurons

Brain cells are mainly of two types, glia and neurons. Glial cells surround neurons and are responsible for various supporting roles in the brain (Barres,

2008) including regulation of extracellular ion levels and removal of waste products (Allen and Barres, 2009). A type of glial cells called Schwann cells myelinate the neuronal axons to speed up the propagation of electrical action potentials. Glial cells also support slow calcium signaling and are thought to play a key role in synapse formation and plasticity (Purves et al., 2012). Neurons are the basic functional units of the nervous system and they are information messengers. Each neuron (i) receives information from the environment or other nerve cells, (ii) processes information, and (iii) sends information to the other neurons or effector tissues (e.g., muscles).

Histologically, there are many different types of neurons in the brain. Neurons in the brain have various morphologies, with large variations in cell bodies, dendritic trees, and axons. In this thesis we consider cortical excitatory and inhibitory neurons and thalamic reticular and relay neurons in our model. Most cortical excitatory neurons are pyramidal and have a triangular soma, a single axon, and a very extensive dendritic tree. Cortical inhibitory neurons are locally projecting neurons that release different neurotransmitters such as gamma-aminobutyric acid (GABA) or glycine. Thalamic reticular neurons are GABAergic and provide an inhibitory innervation to the relay cells of the thalamus (Sherman and Guillery, 2001). Thalamic relay neurons send efferents to the cortex and reticular thalamus and also receives reciprocal afferents (Sherman and Guillery, 2001).

We now provide an overview of the basic structure of a typical neuron and its functioning (Kandel et al., 2000). The main components of the neuron are shown in Fig. 1.3. It is divided into three basic sections: (i) dendrites that receive signals from other neural cells and relay them to the cell body; (ii) cell body (soma), which is the central body of the cell that contains the nucleus and is responsible for generating brief signals in the form of voltage spikes called action potentials at the axonal hillock; and (iii) the axon that propagates the integrated signal to specialized endings called axon terminals that host synapses, which are the points of contact with the dendritic trees of other neurons (Kandel et al., 2000, Purves et al., 2012).

The cell is surrounded by a membrane that is about 5 nm thick and studded with transporter proteins, and penetrated by ion channels. The ion channels can open and close to allow ions to move down concentration gradients between

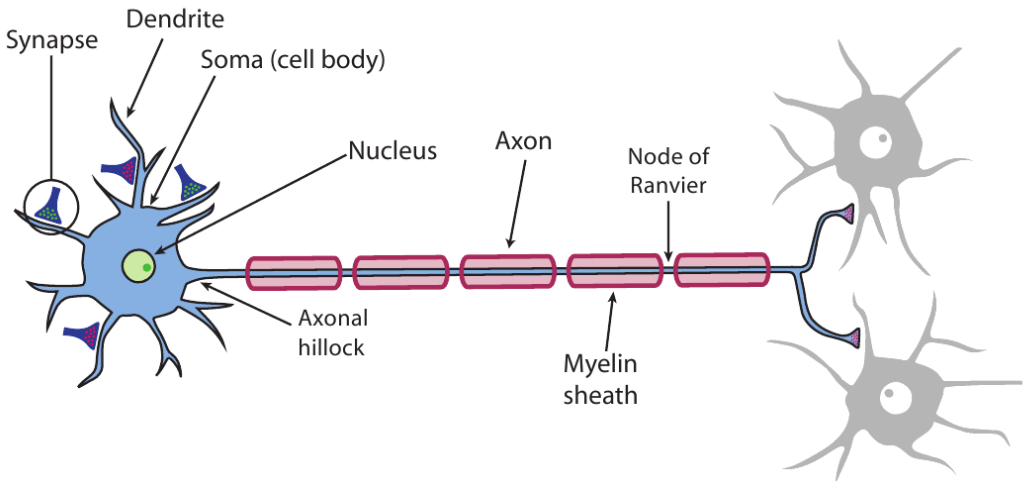

Figure 1.3: Basic structure of a neuron. Incoming signals are received by the dendritic tree through synapses and at the end of the axon, the signal reaches synapses that connect to other neurons. Image adapted from Nolte (2009).

the interior and exterior of the cell (Bear et al., 2001). When not active, the neuron has a constant steady-state voltage across its membrane called the resting membrane potential with an internal potential of about -65 mV relative to the extracellular medium, depending on the type of neuron (Kandel et al., 2000, Purves et al., 2012). The resting membrane potential is maintained by the combined Na^+-K^+ pump that moves Na^+ out of the cell and K^+ into the cell (Kandel et al., 2000, Purves et al., 2012).

Transmission of information from one neuron to another occurs via chemical and electrical interactions at the synapses as shown in Figs 1.4 and 1.5. Synapses form the connections between neurons, at the interface between axon and dendrite (the main case), between pairs of dendrites, or between axon and soma. There are two types of synapses, electrical synapses and chemical synapses. The majority of synapses in the brain are chemical synapses consisting of a presynaptic element, a postsynaptic element, and the synaptic cleft (a gap of approximately 40 nm between the presynaptic and postsynaptic membranes).

Synaptic transmission begins with the arrival of a presynaptic action potential at the axon terminal where the presynaptic terminal becomes depolarized and activates the Ca^{2+} channels and allows Ca^{2+} to enter into the cell. The

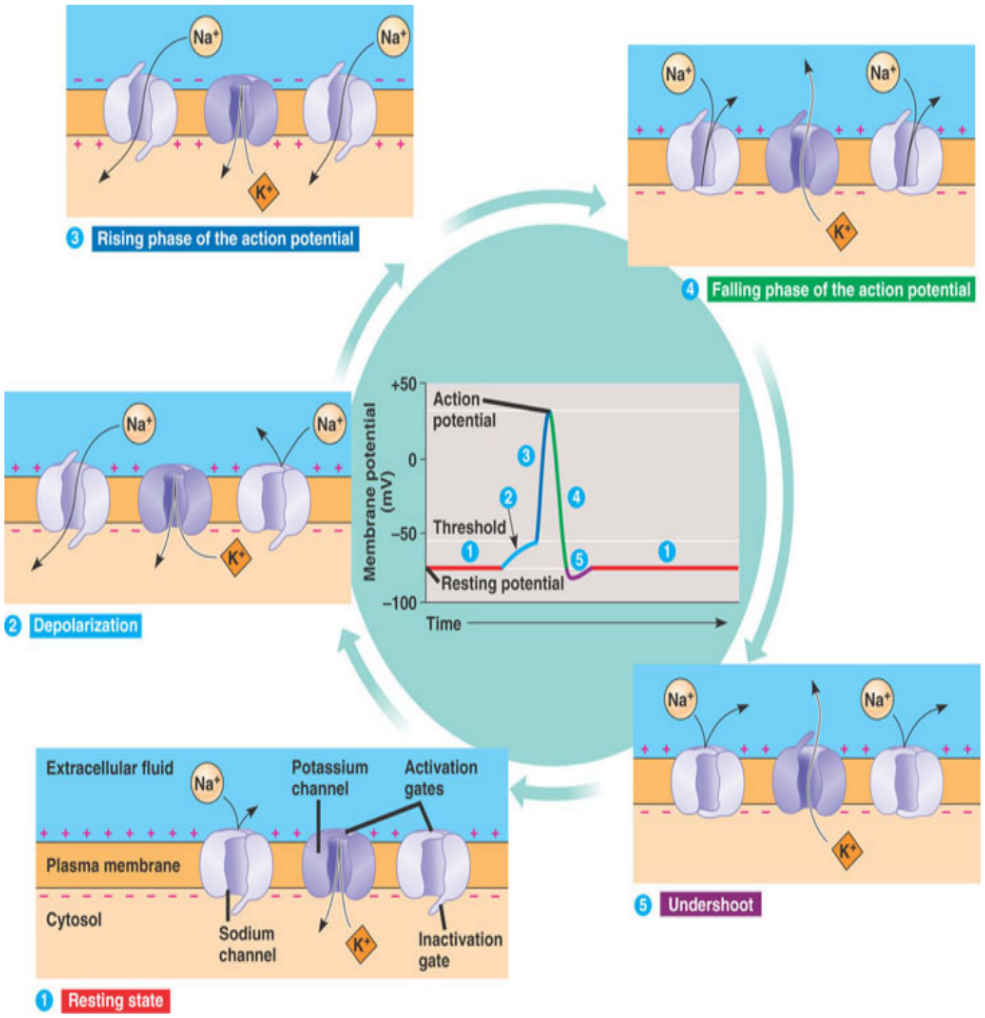

Figure 1.4: Different phases of the action potential and their subsequent changes in ion channel, marked through 1−5. (1) Na^+ and K^+ ion channels are closed and the resting membrane potential is maintained. (2) Stimulus opens the voltage-gated Na^+ channel and depolarizes the membrane. When the depolarization reaches the threshold it triggers an action potential. (3) Depolarization activates the Na^+ channel, causing the sharp rise of the membrane potential. (4) Na^+ channel is closed and K^+ channel is opened, causing the decrease of the membrane potential. (5) Closing both ion channels and reopening the ion pump brings the membrane potential to its resting state. Image adapted from Campbell et al. (2006).

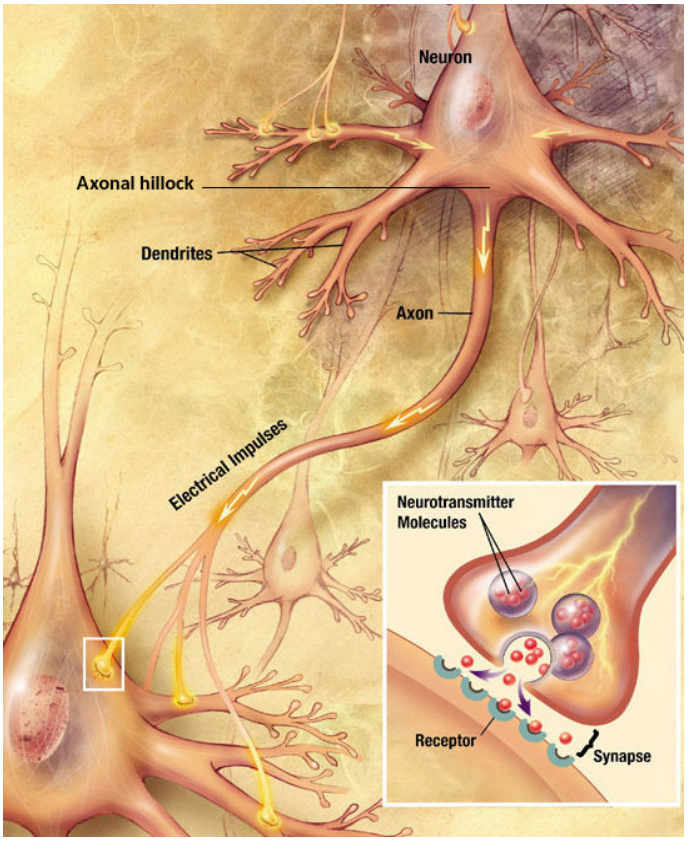

Figure 1.5: A signal propagating down an axon to a receiving neuron across synapse. The inset shows a closer look at the connection between neurons and how neurotransmitters move from neuron to neuron. Image adapted from https://en.wikipedia.org/wiki/Neuron.

resulting inflow of Ca^{2+} allows synaptic vesicles to fuse with the presynaptic plasma membrane and release neurotransmitter chemical into the synaptic cleft to bind to and activate postsynaptic receptors (Haines, 2006, Kandel et al., 2000). The neurotransmitter molecule is either destroyed or recycled to the presynaptic terminal.

When a neurotransmitter binds to its receptor on a dendrite, the result is opening or closing of ion channels on the postsynaptic membrane (Haines, 2006, Phyllis, 1970). Depending on the synapse and specific receptor, the presynaptic release of neurotransmitter can induce an excitatory effect if the synapse causes the postsynaptic potential to increase, known as excitatory postsynaptic

poincreasingtential, or an inhibitory effect if it causes the postsynaptic potential to decrease, known as inhibitory postsynaptic potential (Haines, 2006, Phyllis, 1970). The postsynaptic potential changes in the dendritic tree are propagated to the soma and then integrated at the soma. This gives rise to a voltage change at the soma as it charges (Freeman, 1975, Koch, 1999).

Generation of an action potential begins when the membrane potentialincreasing increases above a critical threshold. The membrane potential crosses a critical threshold on the order of -55 mV and an action potential is generated at the axonal hillock (Kandel et al., 2000, Purves et al., 2012). At this point, Na^+ channels open in the axon hillock and allow a large quantity of Na^+ to enter the cell. An action potential is an "all-or nothing" phenomenon because once the threshold potential is reached, the neuron completely depolarizes.

This results in the membrane potential increasing rapidly, up to a maximum of about +40 mV. At this point, K^+ channels open, causing an outward flow of K^+ ions that again lowers the membrane potential. The membrane potential becomes hyperpolarized until the resting ion concentrations are restored by the ion pumps (Bear et al., 2001).

The inactivated Na^+ channels cannot be opened again until they return to the steady state; this defining absolute refractory period and the neuron is not responsive to inputs. A relative refractory period then remains after the K^+ channels close, in which the membrane potential is more negative than the resting state. The mechanism of the generation of an action potential is summarized in Fig. 1.4. A typical action potential lasts around 1 ms, with a further 2 ms required for the membrane to come back to the resting potential (Haines, 2006, Kandel et al., 2000). Geneartion of an action potential is also referred to as the neuron 'firing'.

The action potential is propagated from the axonal hillock along the axon towards the axonal terminals to relay information to the next neuron. Fast signal transmission happens in two ways: (i) axons with larger diameters have a higher conduction speed because the resistance of the axon is inversely proportional to the diameter (Bear et al., 2001); (ii) conduction speed is increased by insulating the axon with myelinating Schwann cells (glia) (Purves et al., 2012). For myelinated axons, ion channels are clustered at the nodes of Ranvier, which are periodic breaks in the myelin sheath that regenerate the action potential

through ion flows. The spike amplitude remains approximately the same in this process, and propagates along the axon to the axonal terminal to trigger further neurotransmitter release from synaptic vesicles. This process is then repeated at postsynaptic neuron.

1.2 Electroencephalography

Electroencephalography or EEG is a technique that is used to measure the electrical activity generated by the brain cells via electrodes on the scalp. The electrical activity measured by EEG is divided into spontaneous and evoked subtechniques. This section briefly overviews the relevant phenomena of the spontaneous EEG in Sec. 1.2.1, evoked potentials in Sec. 1.2.2, and power spectrum analysis in Sec. 1.2.3.

1.2.1 Spontaneous EEG

Caton and Beck were the first to report the electric field fluctuations in the animal brain (Caton, 1875). After that, in humans the small fluctuations in electrical field at the scalp produced by the ensemble activity of cortical neurons were first detected by Berger (1929).

EEG shows that brain activity covers a wide range of frequencies, from slow waves ($<$ 1 Hz), delta (1-3.5 Hz), and theta waves (3.5-7.5 Hz) during sleep, alpha waves (7.5-13 Hz), beta waves (13-30 Hz), and gamma waves ($>$ 30 Hz) (Niedermeyer and Lopes da Silva, 1999, Nunez and Cutillo, 1995, Nunez and Srinivasan, 2006). The majority of the electrical activity seen in the EEG is generated by groups of pyramidal neurons. The excitatory pyramidal neurons have large dendritic trees and are spatially aligned perpendicular to the cortical layers. These neurons are the most numerous type and are primarily responsible for the EEG (Buzsáki et al., 2012, Niedermeyer and Lopes da Silva, 1999, Nunez and Cutillo, 1995). The inhibitory neurons are smaller cells that primarily interact locally with nearby cells. These neurons contribute much less to the EEG because they are smaller, not spatially aligned, and less numerous (Niedermeyer and Lopes da Silva, 1999, Nunez and Cutillo, 1995).

When brain cells are activated, local current flows across the cell membrane

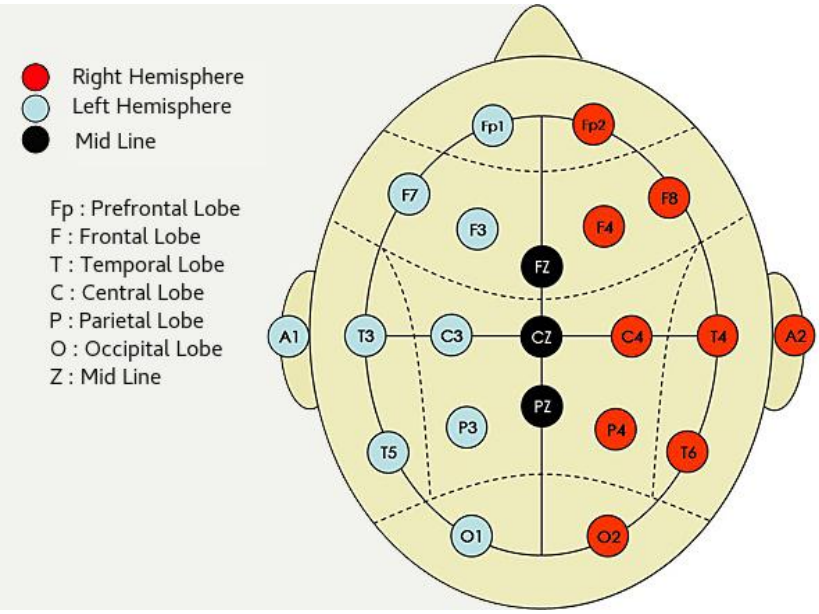

Figure 1.6: Electrode positions on the head as specified by the International 10−20 standard. Electrodes are labeled with their corresponding lobes in the brain. Adapted from Jenkins et al. (2009).

via ion channels. The electrical potential differences are caused by summed excitatory and inhibitory postsynaptic potentials from pyramidal cells and current loops close via the extracellular medium, leading to dipoles (Nunez and Srinivasan, 2006). The resultant effect of the synchronous activity of a large number of aligned electric dipoles can be detected by scalp electrodes producing positive and negative deflections at different regions of the scalp (Lopes da Silva et al., 1974, Nunez and Cutillo, 1995, Teplan, 2002). The potentials result in an externally detectable scalp potential, which is measured via EEG.

An EEG cap with an array of electrodes is placed on the scalp to measure the voltage changes. All voltages are measured relative to a voltage reference and several options are available for EEG (Schomer and Lopes da Silva, 2012). The most common internationally recognized arrangement of electrodes on the scalp is the 10–20 system shown in Fig. 1.6 (Niedermeyer and Lopes da Silva, 1999, Nunez and Cutillo, 1995). In this system electrodes are Fp (prefrontal), F (frontal), T (temporal), C (central), P (parietal), O (occipital), and Z (mid

line). The letters are followed by odd numbers at the left side of the brain and even numbers on the right side.

Signal processing techniques like Fourier transforms, wavelet analysis, and principal component analysis are used to analyze the output of the EEG signals. The EEG has good temporal resolution ($\sim$ 1 ms) but poor spatial resolution ($\gtrsim$ 1 cm) (Niedermeyer and Lopes da Silva, 1999, Nunez and Cutillo, 1995).

1.2.2 Evoked potentials

The evoked potential (EP) is an electrical potential that occurs in the response of the brain to inputs via specific sensory nerve pathways, usually in response to impulsive stimuli (Basar, 1980, Bear et al., 2001, Kandel et al., 2000, Purves et al., 2012). There are three main types of EPs in clinical use: visual, auditory, and somatosensory EPs. Most EP studies employ some kind of averaging across the stimuli. EPs are recorded with an EEG electrode placement. The EEG recordings after each stimulus are averaged together, producing an average EP for that subject (Niedermeyer and Lopes da Silva, 1999). The EEG activity has random phase with respect to the stimulus, whereas the EP is phase-locked to the stimulus and has a large signal-to-noise ratio (Niedermeyer and Lopes da Silva, 1999).

Like the EEG, EPs are widely used to probe brain activity that occurs in response to stimuli and potentially provide a new window on brain processes (Basar, 1980, Niedermeyer and Lopes da Silva, 1999, Rennie et al., 2002, Robinson et al., 2001a). EPs are also used for clinical applications. Visual EPs are used to investigate vision problems as a result of damage to the optic nerve, and somatosensory EPs are studied to find the damage in the connections between the brain and the body (Walsh et al., 2005). Auditory EPs are used to detect hearing problems (Walsh et al., 2005). Besides being useful for diagnosing disorders associated with specific sensory modalities (Macdonell et al., 1989, Nunez and Srinivasan, 2006), EPs can also be used in the diagnosis of depression, dementia, and schizophrenia (Morocutti and Rizzo, 1985, Pfefferbaum et al., 1984).

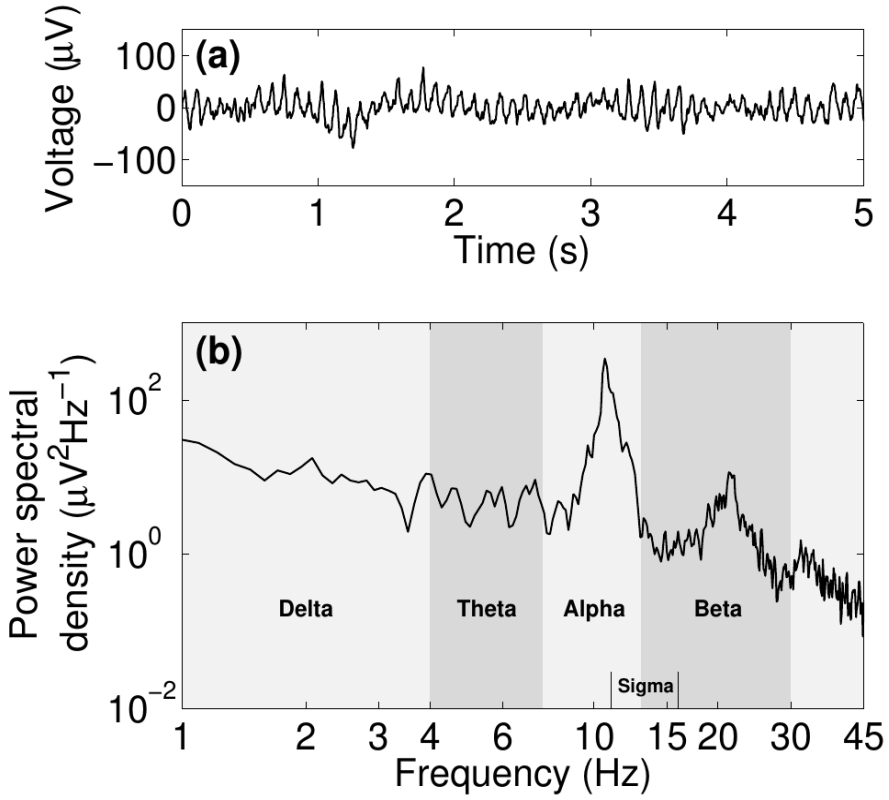

Figure 1.7: EEG example for a healthy human subject in eyes-closed wake state. (a) EEG time series shows a prominent oscillation at ≈ 10 Hz. (b) The EEG power spectrum shows alpha peak at ≈ 11 Hz and the beta peak at ≈ 22 Hz. Image adapted from Abeysuriya (2014).

1.2.3 Power spectrum

Clinical applications of EEG include detection of epileptic seizures and localization of the seizure foci, study of sleep and its disorders in humans, measuring general brain function, determining the depth of anesthesia, and detection of Alzheimer's disease (Niedermeyer and Lopes da Silva, 1999, Nunez, 1974, Vespa et al., 1999). EEGs are a rich source of data and can be analyzed in a number of different ways. Power spectrum analysis is one of the standard methods for the study of EEG signals in both linear and nonlinear systems. The power spectrum reflects the distribution of signal power vs. frequency. EEG power spectra can easily distinguish brain activity in different sleep and wake states

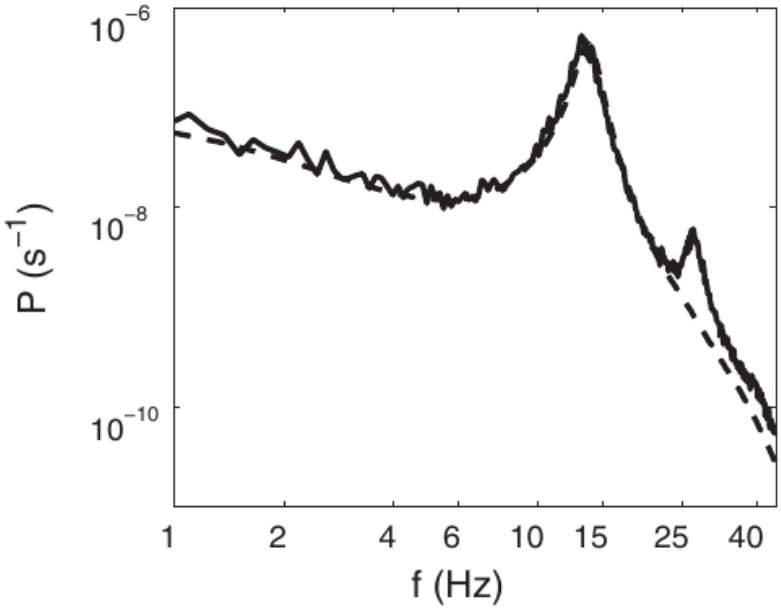

Figure 1.8: EEG power spectrum for sleep spindles with and without nonlinearity indicated by solid and dashed lines, respectively. Image adapted from Abeysuriya et al. (2014a).

(Abeysuriya et al., 2014a, 2015, 2014b, Robinson et al., 2002, 1997).

The two most well known resonant oscillations are the alpha and beta rhythms, which are most prominent during wake with eyes closed. The alpha and beta rhythms are generated as resonances in corticothalamic and intrathalamic loops (Robinson et al., 2004). An example of an EEG power spectrum for an eyes closed wake state is shown in Fig. 1.7 (Abeysuriya, 2014). Aggregated band powers represent a convenient quantitative summary of the EEG, but omit most of the information in the full spectrum.

Another prominent resonant feature of the EEG is that of sleep spindles. Spindles are short bursts of neural activity at $12-15$ Hz that occur between two and five times a minute in sleep stage 2. Spindles last at least 0.5 s and are visible in the EEG at a characteristic frequency of 12–15 Hz (Abeysuriya et al., 2014a, Contreras et al., 1997, Niedermeyer and Lopes da Silva, 1999). An example of a power spectrum showing sleep spindles is seen in Fig. 1.8

(Abeysuriya et al., 2014a). Sleep spindles are generated by interactions between the thalamic reticular and relay populations and then propagate to the cortex (Abeysuriya et al., 2014a, 2015, Robinson et al., 2002, Steriade et al., 1990).

1.3 Brain modeling

The complexity of the brain requires the use of both microscale and macroscale quantitative models to understand its large-scale behavior. There are two general classes of quantitative brain model: neuronal network models that consider individual neurons and continuum models that consider only the ensemble properties of neurons. Models of individual neurons have been an intense area of research since the work of Hodgkin and Huxley (1952) on the giant axon of the squid and its ion currents. Small-scale brain phenomena are easier to explain using neuronal network models, while large-scale phenomena (such as the EEG, fMRI) are more tractable using continuum (mean-field) models. Models of large-scale activity average over microscopic structure to derive continuum descriptions on scales of millimeters to the whole brain.

In this section, an overview of various neural field theory (NFT) models and a corticothalamic neural field model are briefly discussed in Secs 1.3.1 and 1.3.2, respectively.

1.3.1 NFT models

Neural-field models (Amari, 1977, Beurle, 1956, Breakspear et al., 2006, Bressloff and Cowan, 2002, Coombes, 2005, Deco et al., 2008, Freeman, 1975, Jirsa and Haken, 1996, Lopes da Silva et al., 1974, Nunez, 1974, Robinson et al., 1997, Steyn-Ross et al., 2005, Wilson and Cowan, 1973, Wright and Liley, 1994, 1996) are based on mean-field analysis in which individual neural properties are averaged over sub-millimeter scales to describe the dynamics of the neural populations. There has been a long history of neural field based modeling. Beurle (1956) first introduced a neural field model, followed by Griffith (1963, 1965). However, the populations included were purely excitatory and had no refractoriness. Later, Wilson and Cowan (1972, 1973) included inhibitory and exhibitory neurons in addition to refractoriness. In modern terminology the

Wilson-Cowan model (1972, 1973) is a neural field model due to fact that they include spatially-extended activity.

Lopes da Silva et al. (1974) developed a 1D continuum model that included synaptic effects and generated alpha-band activity. This model has been used to study seizures (Wendling et al., 2002, 2000), visual evoked potentials (Jansen and Rit, 1995, Jansen et al., 1993), and recently for EEG and MEG neuroimaging data (David and Friston, 2003, David et al., 2005). Nunez contributed considerably to solving the problem of how neuronal activity determines the actual potentials recorded at the scalp by accounting for issues such as volume conduction and cortical geometry that affect EEG and MEG measurements (Nunez, 1974, Nunez and Cutillo, 1995, Nunez and Srinivasan, 2006).

Freeman (1975) contributed many of the theoretical foundations for neural mass models in which interacting neuronal populations are reduced to single points governed by differential equations, analogous to the point mass in classical mechanics. Wright and Liley (1994) developed a spatially discrete model that incorporated nonlinear effects, axonal delays, and dendritic delays. Jirsa and Haken (1996, 1997) built on the Wilson-Cowan and Nunez approaches to develop a neural field model in differential form including space dependent delays due to finite axonal conduction velocity, yielding damped wave propagation in the cortex. Purely cortical models were further developed by Steyn-Ross et al. (2003, 2001, 2005) and Robinson et al. (2003, 2001a, 2002, 2004, 2003a, 2001b, 2003b) used to model neural activity multiple different brain states and transitions between states.

The Robinson et al. model (2001a, 2002, 1997, 1998) includes cortical and thalamic neural populations and explains the behavior of large neural populations in terms of the mean of key properties such as connection strengths, transmission delays, and firing rates. This model (Robinson et al., 2001a, 2002, 1997, 1998) is based on three main quantities for each population: firing rate, voltage, and fields of axonal pulses. The relationships between these three quantities are shown schematically in Fig. 1.9. Each neural population has a soma voltage V_a which is connected to the firing rate Q_a by a sigmoidal function (Wilson and Cowan, 1973). When the average membrane potential is below the threshold value it does not fire, and above that threshold it fires repeatedly (discussed in Sec. 1.1.2). The neural firing rate is approximated depending on

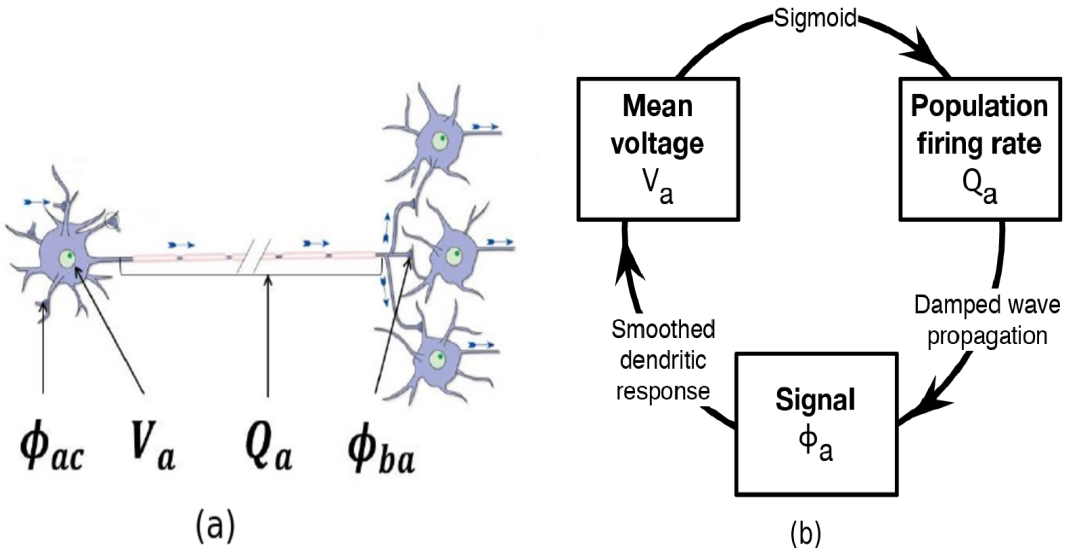

Figure 1.9: Schematic of the neural field model cycle. (a) A neuron with firing rate (Q_a), axonal pulse rate (ϕ_a), and soma volatge (V_a). The signal comes from the presynaptic neuron c and passes through the neuron a to the postsynaptic neuron b. (b) Relationship between the main quantities of the model: the soma voltage V_a in each neural population a, which yields a population firing rate Q_a via a sigmoidal function, generating the field of pulses ϕ_a. The subscript a denotes that multiple populations are involved at each step. Frames (a) and (b) are adapted from Nolte (2009) and Abeysuriya (2014).

voltage as a sigmoidal function of voltage, and the postsynaptic depolarization response.

Each neuron in a neural population has a slightly different threshold voltage which allows the response function resembles a smoothed step function, which corresponds to the sigmoidal function. Action potentials propagate as fields ϕ_a within and between the neural populations when averaged over spatial scales $\sim$0.1 mm. Neural firing Q_a is the source of a field of pulses ϕ_a that quantifies presynaptic signals, and satisfies a damped wave equation (Beurle, 1956, Jirsa and Haken, 1996, Nunez, 1974, Robinson et al., 2004, 1997, 2001b).

Incoming pulses from afferent populations are weighted by connection strengths and each ensuing response contributes to the cell body potential (Robinson et al., 2002, 2001b). The postsynaptic response depends on synaptic

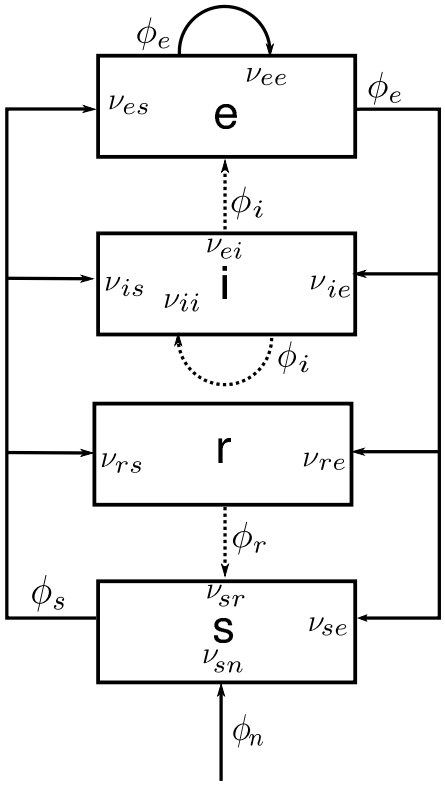

Figure 1.10: The diagram shows connectivities of cortical excitatory (e) and inhibitory (i) populations, plus thalamic reticular (r) and thalamic relay (s) populations and external inputs (ϕ_n). The parameter ν_{ab} quantifies the connection to population a from population b and the ϕ_a are axonal pulse rates (Robinson et al., 2002, 2004). Excitatory connections are shown as solid lines, while inhibitory connections are indicated by dotted lines.

and dendritic dynamics, and is approximated by a second order differential equation parameterized by characteristic rise and decay rates that depend on the neurotransmitters involved (Dayan and Abbott, 2001, Koch, 1999, Robinson et al., 2002, 2001b). The resulting postsynaptic potential of each population is the sum of the contributions from all its afferent populations.

1.3.2 Corticothalamic neural field model

The basic feature of neural field theory (NFT) is that the model equations describing the fundamental components of a neural system (populations of

neurons and connections between them) can be assembled into a range of structures to analyze different brain phenomena. The corticothalamic neural field model generates most signals used to monitor brain activity, in particular EEG signals detected through scalp electrodes (Robinson et al., 2002, 2004, 1997, 1998) (discussed in Sec. 1.2). This model includes four internal populations and their interactions: the cortical excitatory (e) and inhibitory (i) neural populations, plus thalamic reticular (r) and thalamic relay (s) neural populations. A schematic of the model is shown in Fig. 1.10.

The dynamical variables in each neural population a are the mean rate of firing at the cell body Q_a, the propagating axonal fields ϕ_a, and the local mean cell body potential V_a, . An input signal ϕ_n is received by the thalamic relay nucleus and then directed to the relevant cortical areas as shown in Fig. 1.10. The reticular nucleus is innervated by the cortex and the thalamus (Afifi and Bergman, 2005, Sherman and Guillery, 2001). The thalamus has feed-forward connections to the cerebral cortex and cerebral cortex feeds back to the thalamus to complete a thalamo-cortico-thalamic circuit (Sherman and Guillery, 2001). The model includes positive and negative corticothalamic connection strengths, as presented in Fig. 1.10.

The corticothalamic model is used to explain many nonlinear brain phenomena such as harmonic generation, period doubling, spindles in the sleep state, alpha and beta peaks in the wake state, steady state visual evoked potentials (SSVEPs), and entrainment (Abeysuriya et al., 2014a, Ferdousi et al., 2019, Roberts and Robinson, 2008). They have also been applied to the study of various neurological disorders such as Parkinson's disease, epileptic seizures, and coma (Breakspear et al., 2006, Deeba et al., 2018, Müller and Robinson, 2018, Roberts and Robinson, 2012, Robinson et al., 2002, 2004).

Model parameters are constrained by physiological experiments, which is a key strength of the model (Abeysuriya et al., 2014a, 2015, Robinson et al., 2002, 2004). The detail of the corticothalamic neural field model is discussed in later chapters.

1.4 Linear and nonlinear brain activity

Brain activity exhibits both linear and nonlinear behavior as a dynamical system (Stam, 2005). Linear systems can be described by linear equations. Linear systems obey the superposition principle which means the sum of any two solutions is also a solution. Any system near steady state behaves as linear for small perturbations. Our large scale brain activity is linear in normal brain states. The study of linear analysis in the brain is important because linear systems are relatively simple to understand and commonly used methods of EEG, fMRI, and MEG signal analysis make the hypothesis of linearity (Friston et al., 1995, Harrison et al., 2003).

Nonlinear systems exist throughout physics, and are usually studied using nonlinear wave theory (Boyd, 1992, Whitham, 1974) and dynamical systems theory (Freeman and Holmes, 2002). Nonlinear systems present a wealth of complex behaviors, including periodic and chaotic orbits (Freeman and Holmes, 2002), bistability, non-Gaussian statistics (Mendel, 1991), cross-frequency coupling (Boyd, 1992), and synchronization (Pikovsky, 2003).

The study of nonlinear dynamics in the brain is important as it is well established that some brain phenomena are highly nonlinear. These include harmonic generation, period doubling, epileptic seizures, SSVEPs, and entrainment (Breakspear et al., 2006, Deeba et al., 2018, Herrmann, 2001, Roberts and Robinson, 2012). In large scale brain activity, nonlinearity has also been observed in a variety of cases, such as sleep spindle oscillations, strong alpha oscillations, and functional neuroimaging (Abeysuriya et al., 2014a, Ferdousi et al., 2019, Stephan et al., 2008). Nonlinear effects can be driven by neural activity including plasticity, facilitation, refractory effects, depression, and firing-rate nonlinearities (Deco et al., 2008, Freeman, 1975, Koch, 1999, Rennie et al., 1999, 2000), which can cause wave-wave interactions.

The interactions between the dynamics of nonlinear brain oscillations and periodic stimuli contain rich information about brain functions. Despite the wealth of information characterizing the existence of such nonlinear interactions in large scale brain dynamics, the underlying neurophysiological mechanisms remain poorly understood (Herrmann, 2001, Müller and Robinson, 2018, Roberts and Robinson, 2012). To address this, we particularly focus on harmonic

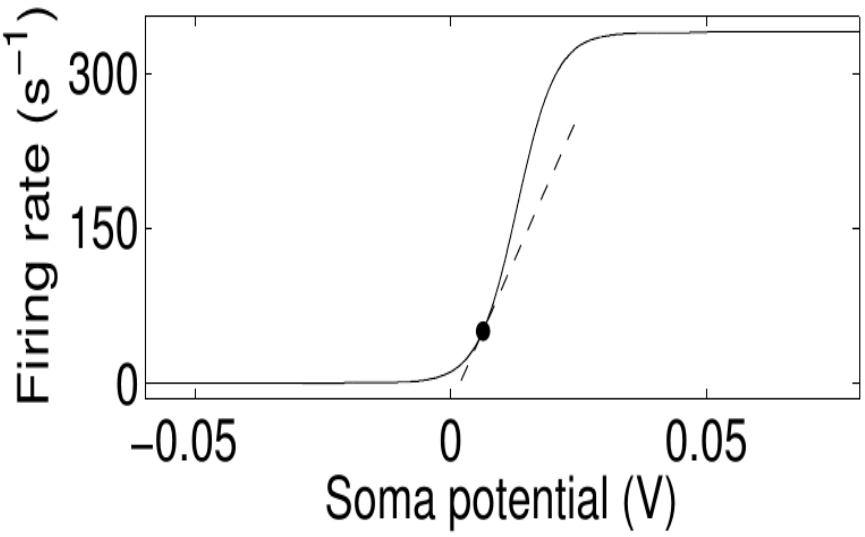

Figure 1.11: Sigmoidal function relates soma potential and firing rate. The dashed line shows the linear approximation in the vicinity of a steady state, pinpointed by the dot. Image adapted from Abeysuriya (2014).

generation in sleep and wake states and wave-wave interactions in SSVEPs in this thesis.

A key nonlinearity in the corticothalamic model (Robinson et al., 2002, 2004, 1997) arises from the sigmoidal response function. The dynamics of the system is presented by employing a linear approximation to the sigmoidal response function near a stable steady state as shown in Fig. 1.11 (Robinson et al., 2002, 2004, Rowe et al., 2004, Stam, 2005, van Albada et al., 2010). This approximation allows linear analysis methods to be used, and analytic evaluation of the power spectrum. The linear predictions of the corticothalamic model reproduce a range of basic phenomena including evoked potentials and the alpha oscillation (Rennie et al., 2002, Robinson et al., 2001a).

1.4.1 Nonlinear applications

One signature of nonlinearity is the generation of new frequency components, such as harmonics. Nonlinear harmonic generation has been found to be significant when driven by sleep spindles, which are strong $12-15$ Hz oscillations

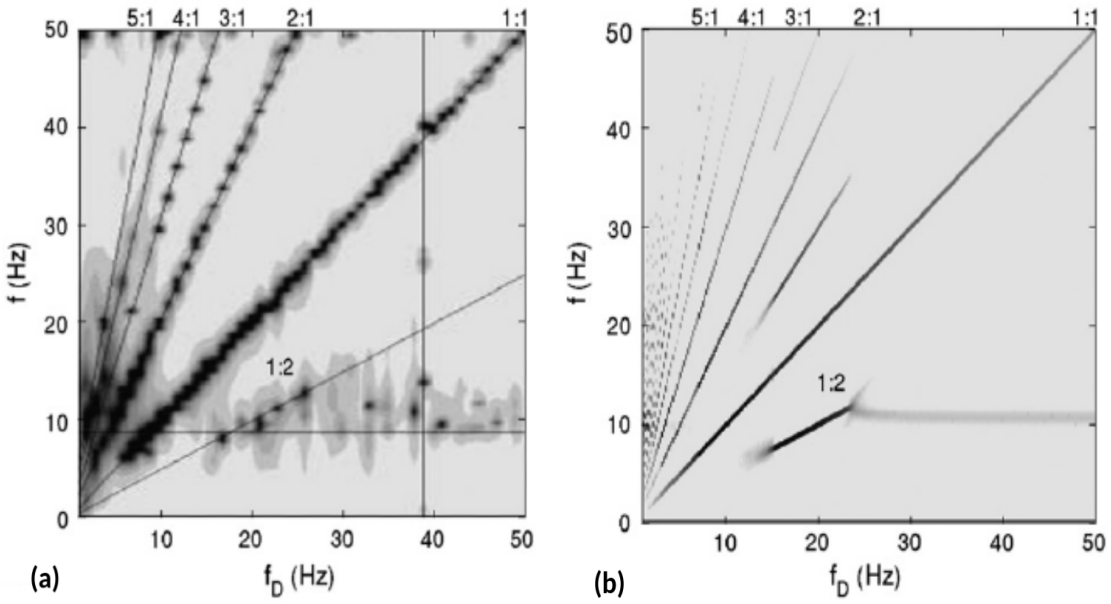

Figure 1.12: Spectral response for $f_D = 0{-}50$ Hz. (a) Responses to the square wave drive frequencies in the experiment of Herrmann (2001). The fundamental (stimulus frequency = response frequency), first, second, third, and fourth harmonics are seen. Alpha ($\approx$ 10 Hz) responds to many stimulation frequencies at intersections with subharmonics. (b). Responses to the sine wave drive frequencies. Image is adapted from Roberts and Robinson (2012).

that usually occur in stage 2 sleep as shown in Fig. 1.8 (Contreras et al., 1997, Niedermeyer and Lopes da Silva, 1999, Stam et al., 1999, Steriade, 2003, Steriade et al., 1985). Sleep spindle harmonics were recently predicted using NFT and later observed in the experiment (Abeysuriya et al., 2014a,b). Nonlinear harmonic generation in sleep and wake states is modeled in Chapter 2.

Stimulus evoked activity also exhibits nonlinearity in certain regimes. SSVEPs are oscillatory brain responses to periodic stimuli observed in the measured EEG (Nunez and Cutillo, 1995). SSVEPs in response to stimuli were first reported by Adrian and Matthews (1934) who also exhibited suppression of the alpha rhythm by attention. The stimulus that causes SSVEPs is often called photic driving or flicker and SSVEPs are considered to be a useful tool to study the neural processes underlying brain rhythmic activities and have been successfully applied in clinical and neuroscience settings (Norcia et al., 2015, Vialatte et al.,

2010). Entrainment and frequency mixing, which involve interactions between stimuli and cortical activity, are also nonlinear features found in SSVEPs (Herrmann, 2001, Rager and Singer, 1998, Regan, 1989, Roberts and Robinson, 2012, Townsend et al., 1975).

SSVEPs are dominated by cortical activity and involve the fundamental frequency of the stimulus as well as its harmonics and subharmonics (Herrmann, 2001, Roberts and Robinson, 2012). The generation of harmonics and subharmonics involve nonlinearities of the visual system that are related to retinal, subcortical, and/or cortical dynamics (Regan, 1989, Roberts and Robinson, 2012). Experiments have measured SSVEP responses at very low stimulus frequencies as well as over a wide range of stimulus frequencies in humans (Herrmann, 2001) and animals (Rager and Singer, 1998). An example of SSVEPs is shown in Fig. 1.12 (Herrmann, 2001), where the fundamental and harmonics (first, second, third, and fourth) of the drive frequency are seen. A strong response of the alpha wave to periodic stimuli, as well as entrainment to a subharmonic of the stimulus frequency are also observed. Similar nonlinear features were theoretically observed by Roberts and Robinson (2012; sum and difference frequencies ($f_D \pm f_\alpha$) were also observed in their work. Nonlinear SSVEP dynamics are modeled in Chapter 3.

1.5 Structure of the thesis

In this chapter, we have briefly reviewed the structure of the brain, EEG measurements of brain activity, linear and nonlinear brain activities, and relevant physiology-based theoretical models (Robinson et al., 2002, 2004) of the brain.

Chapter 2 has a theory of linear and nonlinear spectra and addresses the nonlinear contribution to the spectral peaks. In Chapter 2 we apply the Robinson et al. (2002) corticothalamic neural field model to quantitatively analyze harmonic generation in normal sleep and wake states and nonlinearities in the alpha and beta peaks are quantified. In Chapter 3 we use the same model to analyze nonlinear wave-wave interactions in SSVEPs and the scaling properties of the nonlinear phenomena are studied. Lastly, Chapter 4 provides an overall summary of the outcomes of this thesis and possible future work.

Chapters 2−3 are published, submitted, or in preparation for submission, as individual articles, so there are some overlaps in the content of their introductory sections.

Chapter 2

Nonlinear harmonic generation in the corticothalamic system

Abstract

Neural field theory of the corticothalamic system is applied to quantitatively analyze harmonic generation in normal sleep and wake states. The linear power spectrum is derived analytically via the transfer function and is then convolved with itself and other factors to calculate the nonlinear power spectrum analytically via a recent perturbation expansion. Analysis shows that strong spectral peaks generate a harmonic at twice the original frequency with peak power proportional to the square of that of the original peak. Fits to the data enable absolute normalization to be determined, with the conclusion that the experimentally observed spindle harmonic peak is nonlinear. Using this normalization, the same analysis is applied to the wake state and nonlinear contributions to the alpha and beta peaks are quantified.

2.1 Introduction

Much research has focused on nonlinear brain phenomena such as harmonic generation, period doubling, wave-wave coupling, and entrainment in recent years (Abeysuriya et al., 2014a,b, Herrmann, 2001, Roberts and Robinson, 2012). Nonlinear effects are small in most normal brain states, but some phenomena, such as epileptic seizures, are highly nonlinear (Breakspear et al., 2006, Robinson et al., 2002). Herrmann (2001) performed a steady state visual evoked potential experiment and showed the presence of nonlinearly generated harmonics over a wide range of drive and response frequencies. A strong response of the alpha rhythm to periodic stimuli, including entrainment to a subharmonic of the drive frequency was also observed in that work. In addition, nonlinearity has been observed experimentally when the alpha oscillation is strong (Herrmann, 2001, Stam et al., 1999), and is implied by experimental observations of bistability of the alpha rhythm (Freyer et al., 2009). Nonlinear harmonic generation is also significant when driven by sleep spindles, which are strong $12-15$ Hz oscillations that mostly occur in stage 2 sleep (Contreras et al., 1997, Niedermeyer and Lopes da Silva, 1999, Steriade, 2003, Steriade et al., 1985).

This chapter focuses on harmonic generation in a neural field corticothalamic model of the brain that has successfully reproduced many features of linear and nonlinear brain dynamics and provides a natural basis for modeling and analyzing multiscale neural systems (Abeysuriya et al., 2014a, Amari, 1977, Beurle, 1956, Breakspear et al., 2006, Buice and Cowan, 2007, Deco et al., 2008, Freeman, 1975, Freyer et al., 2011, Jirsa and Haken, 1996, Nunez and Cutillo, 1995, Robinson et al., 2002, 2004, 1997, Steyn-Ross et al., 2005, Wilson and Cowan, 1973, Wright and Liley, 1996).

A previous study (Abeysuriya et al., 2014a) made a number of approximations within neural field theory (NFT) to predict the existence of a nonlinear spindle harmonic for sleep related parameters (Abeysuriya et al., 2014a). They predicted and experimentally confirmed the frequency and scalings of the harmonic peak. This work also found that nonlinear effects were strong in the sleep state but negligible in the wake state (Abeysuriya et al., 2014a). But it is found from experimental observation that nonlinearity can exist in the wake state when the alpha oscillation is sufficiently strong (Freyer et al., 2009, Herrmann,

2001, Stam et al., 1999). Hence, it is necessary to examine these cases further, relaxing approximations made in the sleep state where possible.

Robinson and Roy (2015) expanded the NFT equations in perturbations relative to a fixed point of mean neural activity to provide a systematic basis to examine nonlinear processes in brain activity, including harmonic generation. In the present paper we use this theory to calculate the intensity of harmonic emission. This extends previous work (Abeysuriya et al., 2014a, Robinson and Roy, 2015) and relaxes its approximations. We calculate the linear power spectrum by integrating the square of the transfer function. This is then convolved with itself and other factors to obtain the nonlinear power spectrum (Robinson and Roy, 2015). We then consider a number of approximations and limiting cases to find theoretical scalings for intensity, mean frequency, and bandwidth of strong spectral peaks. These are applied to harmonic generation in sleep and wake states.

The remainder of the chapter is organized as follows. Section 2.2 reviews the corticothalamic model and calculation of the linear power spectrum for this system. In Sec. 2.3 we derive the nonlinear power spectrum and present analytical results, including a variety of approximations. In Sec. 2.4 we numerically evaluate the nonlinear power spectrum and present the applications to spindle and harmonic peaks in the sleep state. Section 2.5 presents applications to alpha and beta peaks in the wake state for this model. Finally, Sec. 2.6 presents a summary and discussion.

2.2 Theory

In this section, we briefly summarize the corticothalamic model used in previous work (Abeysuriya et al., 2014a,b, Roberts and Robinson, 2012, Robinson et al., 2002, 2004, 1997) and calculate the linear power spectrum analytically for this system, prior to the nonlinear analysis in subsequent sections.

2.2.1 Corticothalamic system

The corticothalamic system illustrated in Fig. 2.1 generates many of the observable signals used to monitor brain activity, in particular electroencephalographic

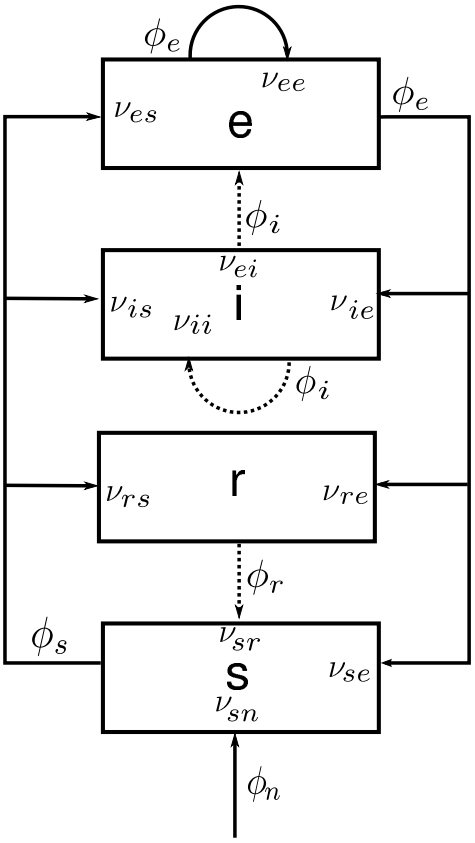

Figure 2.1: The diagram shows the connectivities of cortical (excitatory e, inhibitory i) and thalamic (relay s, reticular r) neural populations. The parameter ν_{ab} quantifies the connection to population a from population b, and the ϕ_a are axonal pulse rates. Excitatory connections are shown with solid lines, and inhibitory connections are shown with dotted lines.

signals detected through scalp electrodes. Our model includes four internal neural populations and their interactions: the cortical excitatory (e) and inhibitory (i) populations, plus thalamic reticular (r) and thalamic relay (s) populations, and external input (ϕ_n) (Kim and Robinson, 2007, Robinson et al., 2002). Each population has a mean cell body potential V_a, driven by pulse rates ϕ_b from

presynaptic populations b, with

$$D_\alpha(t)V_a(\mathbf{r},t) = \sum_b \nu_{ab}\phi_b(\mathbf{r},t-\tau_{ab}), \tag{2.1}$$

$$D_\alpha = \frac{1}{\alpha\beta}\frac{d^2}{dt^2} + \left(\frac{1}{\alpha}+\frac{1}{\beta}\right)\frac{d}{dt} + 1, \tag{2.2}$$

where $\mathbf{r}$ denotes the spatial coordinate on the 2D cortical sheet and t the time. The primary topographic map established by one-to-one reciprocal projections between cortex and thalamus enables the same $\mathbf{r}$ to be associated with points in different populations that map to one another (Robinson et al., 2005). The sum in Eq. (2.1) has b running over e, i, r, s, and all potentials are measured relative to resting. The connection strength ν_{ab} in Eq. (2.1) is defined as $\nu_{ab} = s_{ab}N_{ab}$ where N_{ab} is the mean number of synapses to each neuron in population a from neurons of type b, and s_{ab} is the mean time-integrated strength of the soma response per incoming spike. In Eq. (2.1), $\phi_b(\mathbf{r},t-\tau_{ab})$ is the mean spike arrival rate from neurons b, allowing for a time delay τ_{ab} due to any discrete anatomical separations between different populations (Rennie et al., 1999, Roberts and Robinson, 2012, Robinson et al., 2004). The parameters β and α are the characteristic rise rate and decay rate, respectively, of the cell body potential produced by an impulse at a dendritic synapse, allowing for the effects of synaptic, dendritic, and soma dynamics.

The mean potential V_a generates a mean firing rate Q_a via a sigmoid response function, with (Freeman, 1975, Wilson and Cowan, 1973)

$$Q_a(\mathbf{r},t) = S\big[V_a(\mathbf{r},t)\big], \tag{2.3}$$

$$S[V_a(\mathbf{r},t)] = \frac{Q_{\max}}{1+\exp\left[-\{V_a(\mathbf{r},t)-\theta\}/\sigma'\right]}, \tag{2.4}$$

where $Q_{\max}$ is the maximum possible firing rate, θ is the mean threshold voltage, and $\sigma = \sigma'\pi/\sqrt{3}$ is the standard deviation of the threshold distribution.

The firing rate Q_a is the source of ϕ_a, which approximately obeys the damped

wave equation (Robinson et al., 2002, 1997)

$$D_a(\mathbf{r},t)\phi_a(\mathbf{r},t) = Q_a(\mathbf{r},t), \tag{2.5}$$

$$D_a(\mathbf{r},t) = \frac{1}{\gamma_a^2}\frac{\partial^2}{\partial t^2} + \frac{2}{\gamma_a}\frac{\partial}{\partial t} + 1 - r_a^2\nabla^2, \tag{2.6}$$

where r_a is the mean axon length in the population a, v_a is the pulse velocity, $\gamma_a = v_a/r_a$ is an effective damping rate, and ∇^2 is the Laplacian operator. In populations other than e, r_a is so small that one can set $D_a = 1$.

There are 16 possible connections between the four neural populations in Fig. 2.1, but only 10 of them are nonzero in our model, as seen in Fig. 2.1. We assume that the number of connections to and between cortical populations is proportional to the number of synapses available (Braitenberg and Schüz, 1998, Liley and Wright, 1994, Wright and Liley, 1994). This random connectivity approximation implies that $N_{ib} = N_{eb}$ for all b. We express inhibitory quantities in terms of excitatory quantities and only deal with the excitatory quantities later explicitly. The connection strengths are also symmetric, with $\nu_{ie} = \nu_{ee}, \nu_{ii} = \nu_{ei}$ and $\nu_{is} = \nu_{es}$ (Robinson et al., 2004), giving eight distinct connection strengths. The connections ν_{ei} and ν_{sr} are inhibitory (negative) while the other connections in the model are excitatory (positive). For the system in Fig. 2.1, the only nonzero delays τ_{ab} are $\tau_{es} = \tau_{is} = \tau_{se} = \tau_{re} = t_0/2$ where t_0 is the total corticothalamic loop delay.

2.2.2 Steady states and linear power spectrum

We are interested in looking for steady states which corresponds to normal brain activity. We can obtain a nonlinear equation for uniform steady states of brain activity by setting all derivatives to zero in Eqs (2.2) − (2.6). The steady-state value $\phi_e^{(0)}$ of ϕ_e is then given by (Robinson et al., 2004)

$$\begin{aligned} &S^{-1}(\phi_e^{(0)}) - (\nu_{ee}+\nu_{ei})\phi_e^{(0)} \\ &= \nu_{es}S\Big\{\nu_{se}\phi_e^{(0)} + \nu_{sr}S\Big[\nu_{re}\phi_e^{(0)} \\ &\quad + \frac{\nu_{rs}}{\nu_{es}}\Big\{S^{-1}(\phi_e^{(0)}) - (\nu_{ee}+\nu_{ei})\phi_e^{(0)}\Big\}\Big] + \nu_{sn}\phi_n^{(0)}\Big\}, \end{aligned} \tag{2.7}$$

Table 2.1: Parameters for sleep-spindle state and eyes-closed (EC) wake state (Abeysuriya et al., 2014a, Robinson et al., 2002, 2004), ($ab = es, is, se, re$).

Quantity	Symbol	Spindle	Wake	Unit
Voltage decay rate	α	45	83	s^{-1}
Voltage rise rate	β	185	769	s^{-1}
Corticothalamic delay	τ_{ab}	42.5	42.5	ms
Cortical damping rates	γ_e	116	116	s^{-1}
Other damping rates	$\gamma_{i,r,s}$	12000	12000	s^{-1}
Threshold spread	σ'	3.8	3.8	mV
Maximum firing rate	$Q_{\max}$	340	340	s^{-1}
Axonal ranges:				
	r_e	86	86	mm
	$r_{i,r,s}$	1.5	1.5	mm
Connection strengths:				
e from e	ν_{ee}	3.06	1.35	mV s
e from i	ν_{ei}	-3.24	-2.32	mV s
e from s	ν_{es}	0.92	1.18	mV s
r from e	ν_{re}	0.26	0.26	mV s
r from s	ν_{rs}	2.88	0.08	mV s
s from e	ν_{se}	4.73	2.66	mV s
s from r	ν_{sr}	-1.95	-1.18	mV s
Subthalamic input to s	$\nu_{sn}\phi_n^{(0)}$	2.70	0.14	mV
Gains:				
ee	G_{ee}	6.65	2.63	-
ei	$-G_{ei}$	7.03	4.53	-
es	G_{es}	1.10	2.30	-
re	G_{re}	1.75	1.27	-
rs	G_{rs}	19.34	0.38	-
se	G_{se}	0.66	3.49	-
sr	$-G_{sr}$	0.27	1.54	-
sn	G_{sn}	0.38	0.19	-
Steady state pulse rates:				
e	$\phi_e^{(0)}$	8.5	7.6	s^{-1}
r	$\phi_r^{(0)}$	27.8	19.9	s^{-1}
s	$\phi_s^{(0)}$	0.5	5.0	s^{-1}

where $\phi_n^{(0)}$ is the steady state component of the input stimulus, which only appears in Eq. (2.7) in the combination $\nu_{sn}\phi_n^{(0)}$. Corresponding steady-state values of the other $\phi_a^{(0)}$ can be found from Eqs (2.2) – (2.6). Equation (2.7) has stable steady-state solutions and has been identified with normal brain activity (Robinson et al., 1997).

The leading terms of the Taylor expansion of Eq. (2.3) give

$$Q_a(\mathbf{r},t) \approx Q_a^{(0)} + S_a' \left[V_a(\mathbf{r},t) - V_a^{(0)}\right] + \frac{1}{2}S_a'' \left[V_a(\mathbf{r},t) - V_a^{(0)}\right]^2, \tag{2.8}$$

where S_a' and S_a'' are the first and second derivatives of Q_a with respect to V_a, evaluated at $V_a^{(0)}$. The units of $Q_a(\mathbf{r},t)$ are s^{-1}.

Previous work has successfully modeled resting brain states in the linear regime (Robinson et al., 2002, 2004, 1997, Rowe et al., 2004). In cases where one considers only the linear term of Eq. (2.8), this yields

$$Q_a^{(1)}(\mathbf{r},t) = S_a' V_a^{(1)}(\mathbf{r},t), \tag{2.9}$$

where numerical superscripts indicate the order of perturbation.

The units of $\phi_n(\mathbf{r},t)$ are s^{-1}. However, after transformation to Fourier space via

$$\phi_n(\mathbf{k},\omega) = \int d^2\mathbf{r} \int dt\ \phi_n(\mathbf{r},t)\ e^{-i\mathbf{k}.\mathbf{r}\ + i\omega t}. \tag{2.10}$$

The units of $\phi_n(\mathbf{k},\omega)$ are seen to be m^2.

The dominant contribution to EEG and fMRI signals is from the field ϕ_e, since excitatory pyramidal neurons are most numerous and aligned in the cortex (Kandel et al., 2000, Nunez and Cutillo, 1995). Hence we take the Fourier transform of Eqs (2.1) – (2.9) and eliminate other terms to get $\phi_e(\mathbf{k},\omega)$. In

particular, we find the dimensionless transfer function

$$T_{en}(\mathbf{k},\omega) = \frac{\phi_e^{(1)}(\mathbf{k},\omega)}{\phi_n^{(1)}(\mathbf{k},\omega)}, \tag{2.11}$$

$$= \frac{L^2 G_{esn} e^{i\omega t_0/2}}{(1-L^2G_{srs})(1-G_{ei}L)} \frac{1}{k^2 r_e^2 + q^2 r_e^2}, \tag{2.12}$$

$$q^2 r_e^2 = \left(1 - \frac{i\omega}{\gamma_e}\right)^2 - \frac{1}{1-G_{ei}L}\left[LG_{ee} + \frac{[L^2 G_{ese} + L^3 G_{esre}]\, e^{i\omega t_0}}{1-L^2 G_{srs}}\right], \tag{2.13}$$

$$L(\omega) = \left(1 - \frac{i\omega}{\alpha}\right)^{-1}\left(1 - \frac{i\omega}{\beta}\right)^{-1}, \tag{2.14}$$

where $\mathbf{k}$ is the wave vector ($k = 2\pi/\lambda$ where λ is the wavelength) and ω is the angular frequency ($\omega = 2\pi f$ where f is the frequency in Hz) and L incorporates the characteristics of synaptodendritic dynamics. The gain $G_{ab} = S'_a N_{ab} = S'_a \nu_{ab}$ is the average number of extra spikes produced in neurons of type a per extra incoming spike from neurons of type b. The quantities $G_{ese} = G_{es}G_{se}$, $G_{esre} = G_{es}G_{sr}G_{re}$, $G_{srs} = G_{sr}G_{rs}$, $G_{esn} = G_{es}G_{sn}$, are gains for the excitatory corticothalamic, inhibitory corticothalamic (as are products involving inhibitory terms), intrathalamic loops, and input path, respectively (Robinson et al., 2002, 2004). The gains G_{ei} and G_{sr} are negative as a result of inhibitory connections between their respective populations and the remaining gains are positive.

The spatiotemporal power spectrum of $\phi_e^{(1)}$ is

$$P_e(\mathbf{k},\omega) = |T_{en}(\mathbf{k},\omega)|^2 \; |\phi_n^{(1)}(\mathbf{k},\omega)|^2. \tag{2.15}$$

The units of $P_e(\mathbf{k},\omega)$ are m^4. To focus on the temporal frequency spectrum, we must integrate over $\mathbf{k}$, with

$$P_e(\omega) = \int d^2\mathbf{k} \; |\phi_n^{(1)}(\mathbf{k},\omega)|^2 \; |T_{en}(\mathbf{k},\omega)|^2. \tag{2.16}$$

If the input stimulus $\phi_n^{(1)}(\mathbf{k},\omega)$ is white noise (Roberts and Robinson, 2012,

Robinson et al., 2002, 2004, 1997), $|\phi_n^{(1)}(\mathbf{k},\omega)|^2 = |\phi_n|^2$ is constant for nonzero $\mathbf{k}$ and ω. The value of ϕ_n then only affects the normalization of the power spectrum. After integrating Eq. (2.16) over all $\mathbf{k}$ we get the analytic power spectrum, which is (Roberts and Robinson, 2008, 2012, Robinson et al., 2002, 2004, 1997)

$$P_e(\omega) = \frac{\pi\ |\phi_n|^2}{r_e^2} \left| \frac{L^2 G_{esn}}{(1 - G_{ei}L)(1 - L^2 G_{srs})} \right|^2 \left| \frac{\text{Arg}\ (q^2 r_e^2)}{\text{Im}\ (q^2 r_e^2)} \right|, \tag{2.17}$$

where Arg denotes the complex argument and Im is the imaginary part. The units of $P_e(\omega)$ are m^2.

When the finite size of the brain is taken into account, which it must be when k is small and the wavelengths of interest are comparable to the brain's linear dimensions, the discreteness of eigenmodes of brain activity must be taken into account and the integral in (2.15) must be replaced by a sum over modes, weighted by the volume $(\Delta k)^2$ of 2D wave-number space each represents. In this case, the uniform $\mathbf{k} = \mathbf{0}$ mode is often dominant, especially at spectral peak (Mukta et al., 2017, Robinson et al., 2001a). So one useful approximation for the linear power spectrum is to retain only the $\mathbf{k} = \mathbf{0}$ mode, which means only considering variations that occur uniformly over the entire brain. The uniform $\mathbf{k} = \mathbf{0}$ mode is the least stable and it plays a significant role in the dynamics (Robinson et al., 1997). From Eqs (2.12) and (2.16) we find, for the $\mathbf{k} = \mathbf{0}$ mode,

$$P_e(\omega) = (\Delta k)^2 |\phi_n|^2 \left| \frac{L^2 G_{esn}}{(1 - G_{ei}L)(1 - L^2 G_{srs})} \right|^2 \frac{1}{|q^4 r_e^4|}. \tag{2.18}$$

Figure 2.2 shows the analytical linear power spectrum using Eq. (2.17) for the illustrative sleep parameters listed in Table 2.1 (Abeysuriya et al., 2014a). Strong sleep spindles occur in the intrathalamic feedback loop when the loop strength approaches a critical value corresponding to a stability boundary in the model (Robinson et al., 2002). The spindle peak is found at ≈ 13.5 Hz in the linear power spectrum which agrees with numerical results (Abeysuriya et al., 2014a). Theoretically, the sleep spindle peak has a frequency f_σ related to the rate constants α and β with $f_\sigma = \sqrt{\alpha\beta}/(2\pi) \approx 14.5$ Hz (Robinson et al.,

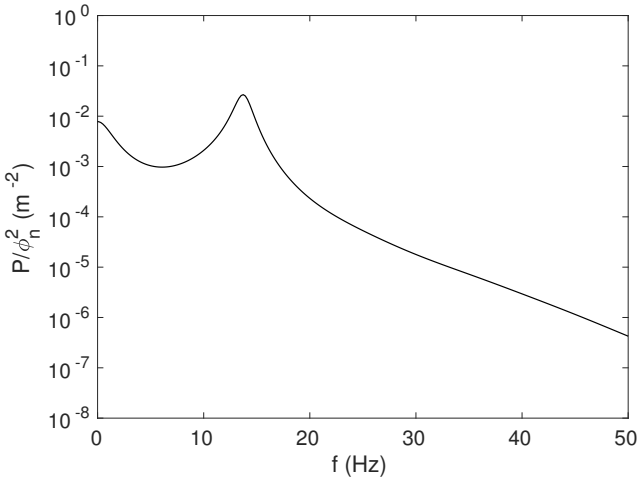

Figure 2.2: Linear power spectrum of ϕ_e on a logarithmic scale for spindle parameters from Table 2.1. The spindle peak occurs at ≈ 13.5 Hz.

2002, 2004). The reason for the discrepancy between these values is that the spindle peak is superposed on a steeply decreasing background spectrum, which has the effect of reducing its peak frequency from the resonant value.

2.3 Nonlinear analysis

In this section, we calculate the nonlinear power spectrum analytically and then derive a variety of analytic approximations and scalings to the nonlinear power spectrum.

2.3.1 Analytic nonlinear power spectrum

Robinson and Roy (2015) explored some characteristics of the nonlinear power spectrum in the case in which the only nonlinearity is in the sigmoid firing rate response. However, their work did not show all terms explicitly, so we derive the full result in this section.

The power spectrum can be written as (Robinson and Roy, 2015)

$$\begin{aligned} P_a(\kappa) &= \left| \phi_a(\kappa) - \phi_a^{(0)} \right|^2, && (2.19)\\ &\approx \left|\phi_a^{(1)}(\kappa)\right|^2 + 2 \text{ Re } \left[\phi_a^{(1)}(\kappa)\ \phi_a^{(2)*}(\kappa)\right] \\ &+ |\phi_a^{(2)}(\kappa)|^2 + 2 \text{ Re } \left[\phi_a^{(1)}(\kappa)\ \phi_a^{(3)*}(\kappa)\right], && (2.20)\\ &= \left\langle P_a^{(1)}(\kappa)\right\rangle + 2 \left\langle \text{ Re } \left[\phi_a^{(1)}(\kappa)\ \phi_a^{(2)*}(\kappa)\right]\right\rangle \\ &+ \left\langle P_a^{(2)}(\kappa)\right\rangle + 2 \left\langle \text{ Re } \left[\phi_a^{(1)}(\kappa)\ \phi_a^{(3)*}(\kappa)\right]\right\rangle, && (2.21) \end{aligned}$$

where $\kappa = (\mathbf{k}, \omega)$ and the angular brackets are averages over the phase of the inputs. We assume that the inputs to the system (ϕ_n and ϕ_m) are random-phase and uncorrelated with unit variance, without loss of generality. This corresponds to

$$\left\langle \phi_n^{(1)}(\mathbf{r}, t)\ \phi_m^{(1)*}(\mathbf{r}', t')\right\rangle = \delta_{nm}\delta^2(\mathbf{r} - \mathbf{r}')\delta(t - t'). \quad (2.22)$$

The first term in (2.21) is the usual linear power spectrum, which is a quadratic function of the external input $\phi_n^{(1)}$. The linear spectrum leads to a double sum over products of these quantities, which collapses to a single sum over n because of the factor δ_{nm} in (2.22).

The second term in (2.21) averages to zero which involves a product of three of the uncorrelated $\phi_n^{(1)}$. The factor δ_{nm} in (2.22) makes the phase average zero for different noise sources. The third term is the second order power spectrum which is a quartic function of the external input $\phi_n^{(1)}$.

The second order power spectrum can be written as

$$\begin{aligned} P_a^{(2)}(\kappa) &= \left\langle |\phi_a^{(2)}(\kappa)|^2 \right\rangle, && (2.23)\\ &= \left\langle \phi_a^{(2)}(\kappa)\ \phi_a^{(2)*}(\kappa)\right\rangle, && (2.24) \end{aligned}$$

where $\phi_a^{(2)}$ is the second order term in the expansion of ϕ_a in terms of the input perturbation to the system.

Previous work showed (Robinson and Roy, 2015),

$$\phi_a^{(2)}(\kappa) = \frac{1}{2}\sum_b \Gamma_b S_b'' \hat{T}_{ab} V_b^{(1)} \otimes V_b^{(1)}, \tag{2.25}$$

$$\Gamma_b(\kappa) = \left[\left(1 - \frac{i\omega}{\gamma_b}\right)^2 + k^2 r_b^2\right]^{-1}, \tag{2.26}$$

$$S_b'' = \frac{2Q_b^3}{\sigma'^2 Q_{\max}^2} - \frac{3Q_b^2}{\sigma'^2 Q_{\max}} + \frac{Q_b}{\sigma'^2}, \tag{2.27}$$

$$\hat{\mathbf{T}} = (\mathbf{I} - \mathbf{X})^{-1}, \tag{2.28}$$

$$X_{ab}(\kappa) = L\Gamma_a(\kappa) S_a' e^{i\omega\tau_{ab}} \nu_{ab}^{(0)}, \tag{2.29}$$

$$S_a' = \frac{Q_a}{\sigma'}\left(1 - \frac{Q_a}{Q_{\max}}\right), \tag{2.30}$$

$$V_b^{(1)}(\kappa) = T_{bx}^V(\kappa)\ \phi_n^{(1)}(\kappa), \tag{2.31}$$

where $\mathbf{I}$ is the identity matrix and $\hat{\mathbf{T}}$ and $\mathbf{X}$ are matrices of the elements T_{ab} and X_{ab}, respectively. The symbol $\otimes$ indicates a convolution, with $f \otimes g$ defined by

$$(f \otimes g)(\kappa) = \int d\kappa_1 \int d\kappa_2 f(\kappa_1) g(\kappa_2)\ \delta(\kappa - \kappa_1 - \kappa_2). \tag{2.32}$$

Using Eqs (2.25) − (2.32), Eq. (2.24) can be written as

$$\begin{aligned} P_a^{(2)}(\kappa) = \frac{1}{4}\sum_{bc} &\left[\Gamma_b(\kappa)\Gamma_c^*(\kappa) S_b'' S_c'' \hat{T}_{ab}(\kappa)\hat{T}_{ac}^*(\kappa)\right] \\ &\times \int d\kappa_1 \int d\kappa_2 \int d\kappa_3 \int d\kappa_4 \\ &\times \delta(\kappa - \kappa_1 - \kappa_2)\ \delta(\kappa - \kappa_3 - \kappa_4) \\ &\times T_{bx}^V(\kappa_1) T_{bx}^V(\kappa_2) T_{cx}^{V*}(\kappa_3) T_{cx}^{V*}(\kappa_4) \\ &\times \left\langle \phi_n(\kappa_1)\phi_n(\kappa_2)\phi_n^*(\kappa_3)\phi_n^*(\kappa_4)\right\rangle . \end{aligned} \tag{2.33}$$

The phase average in Eq. (2.33) is zero unless its four factors can be split into two pairs, each of which has a nonzero average (Robinson and Roy, 2015). For the product of two such factors to have a nonzero average, their noise sources must be the same and their phases must be equal and opposite, which in turn implies that their κ vectors must be equal and opposite (or equal if their

phases are opposite in sign), because Fourier transforms of real quantities satisfy $\phi_n^{(1)}(-\kappa) = [\phi_n^{(1)}(\kappa)]^*$. Hence, $\kappa_1 = \kappa_3$ and $\kappa_2 = \kappa_4$, or $\kappa_3 = \kappa_2$ and $\kappa_4 = \kappa_1$, which gives an equal contribution.

Upon using these relationships in Eq. (2.33) one finds

$$P_a^{(2)}(\kappa) = (\Delta\kappa)\frac{|\phi_n|^4}{4}\sum_{bc} F_{abc}(\kappa) \times \int d\kappa_1 C_{bc}(\kappa_1)C_{bc}(\kappa - \kappa_1), \tag{2.34}$$

with

$$F_{abc}(\kappa) = \Gamma_b(\kappa)\Gamma_c^*(\kappa)S_b^{''}S_c^{''}\hat{T}_{ab}(\kappa)\hat{T}_{ac}^*(\kappa), \tag{2.35}$$

$$C_{bc}(\kappa) = T_{bn}^V(\kappa)T_{cn}^{V*}(\kappa), \tag{2.36}$$

$$T_{an}^V(\kappa) = L(\omega)\left[e^{i\omega\tau_{an}}\nu_{an}^{(0)} + \sum_b e^{i\omega\tau_{ab}}\nu_{ab}^{(0)}T_{bn}(\kappa)\right], \tag{2.37}$$

with (2.14) and (2.26)−(2.30). The sum in Eq. (2.37) extends over all populations and T_{bn} is the transfer function to $\phi_b^{(1)}$ from an external input $\phi_n^{(1)}$. Equation (2.34) embodies three-wave interactions in which waves of wave vector $\mathbf{k}_1$ and $\mathbf{k} - \mathbf{k}_1$ interact to produce a response at $\mathbf{k}$.

A similar analysis to that given above shows that the terms that are nonzero in the fourth term in (2.21) in the random-phase case are ones that represent four-wave interactions in which two incoming linear waves scatter to a pair of outgoing waves with the same wave vectors and frequencies (Robinson and Roy, 2015). Since these interactions do not change the spectrum, we do not consider this term further here.

2.3.2 Approximation for $a = e$ and $b = c = s$

Nonlinearity in the system occurs when strong population voltage oscillations are present (Abeysuriya et al., 2014a). Abeysuriya et al. (2014a) found that the voltage fluctuations in the relay nuclei are over six times larger than fluctuations in any of the other populations in the sleep state in which $\sim$ 14 Hz spindle oscillations are most common (Abeysuriya et al., 2014a). They simplified

the analysis by including nonlinearity only in the relay nuclei and calculated the nonlinear power spectrum numerically with the above approximation. To compare with numerical results (Abeysuriya et al., 2014a), we consider this case $a = e$ and $b = c = s$ and simplify the analytic nonlinear power spectrum in Eq. (2.34) to

$$P_e^{(2)}(\kappa) = (\Delta\kappa)\frac{|\phi_n|^4}{4}F_{ess}(\kappa)\int d\kappa_1 C_{ss}(\kappa_1)\; C_{ss}(\kappa-\kappa_1), \tag{2.38}$$

with

$$F_{ess}(\kappa) \approx \left[S_s^{''}\right]^2 \left|\hat{T}_{es}(\kappa)\right|^2, \tag{2.39}$$

$$X_{es}(\kappa) = L\Gamma_e S_e^{'} e^{i\omega\tau_{es}}\nu_{es}^{(0)}, \tag{2.40}$$

$$C_{ss}(\kappa) = \left|T_{sn}^V(\kappa)\right|^2, \tag{2.41}$$

$$= |L(\omega)|^2 \left[\nu_{es}^{(0)}\right]^2 |T_{sn}(\kappa)|^2, \tag{2.42}$$

$$T_{sn}(\kappa) = J_{sn}/B, \tag{2.43}$$

$$J_{ab} = L(\omega)S_a^{'}\nu_{ab}e^{i\omega\tau_{ab}}, \tag{2.44}$$

$$B(\kappa) = 1 - \frac{J_{ese}}{A} - \frac{J_{esre}}{A} - J_{srs}, \tag{2.45}$$

$$J_{ese} = J_{es}J_{se}, \tag{2.46}$$

$$J_{esre} = J_{es}J_{sr}J_{re}, \tag{2.47}$$

$$J_{ese} = J_{sr}J_{rs}, \tag{2.48}$$

$$A(\kappa) = \frac{D_e - D_e J_{ei}}{D_i} - J_{ee}, \tag{2.49}$$

$$D_e(\kappa) = 1/\Gamma_e(\kappa), \tag{2.50}$$

where $\Gamma_s(\kappa) \approx 1$ has been used and L, Γ_e and $S_e^{'}$ are defined in Eqs (2.14), (2.26), and (2.30). Hence,

$$P_e^{(2)}(\kappa) = (\Delta\kappa)\frac{|\phi_n|^4}{4}\left[S_s^{''}\right]^2\left|\hat{T}_{es}(\kappa)\right|^2\int d\kappa_1 C_{ss}(\kappa_1)C_{ss}(\kappa-\kappa_1). \tag{2.51}$$

2.3.3 Approximation for $\mathbf{k} = \mathbf{k}_1 = 0$

A second approximation is to consider only the $\mathbf{k} = \mathbf{k}_1 = 0$ mode in the nonlinear power spectrum because the uniform $\mathbf{k} = \mathbf{k}_1 = 0$ mode is often

dominant, especially at spectral peaks (Mukta et al., 2017). Then the nonlinear power spectrum from Eq. (2.34) is

$$P_a^{(2)}(\omega) = (\Delta\omega)\frac{|\phi_n|^4}{4}\sum_{bc} F_{abc}(\omega)\int d\omega_1 C_{bc}(\omega_1)\; C_{bc}(\omega-\omega_1), \quad (2.52)$$

with

$$F_{abc}(\omega) = \Gamma_b(\omega)\Gamma_c^*(\omega)S_b^{''}S_c^{''}\hat{T}_{ab}(\omega)\hat{T}_{ac}^*(\omega), \quad (2.53)$$
$$C_{bc}(\omega) = T_{bn}^V(\omega)T_{cn}^{V*}(\omega), \quad (2.54)$$
$$T_{an}^V(\omega) = L(\omega)\Big[e^{i\omega\tau_{an}}\nu_{an}^{(0)} + \sum_b e^{i\omega\tau_{ab}}\nu_{ab}^{(0)}T_{bn}(\omega)\Big], \quad (2.55)$$

with (2.14) and (2.26) – (2.30).

2.3.4 Approximation for $a = e$ and $b = c = s$ and $\mathbf{k} = \mathbf{k}_1 = 0$

A third approximation is to consider the $\mathbf{k} = \mathbf{k}_1 = 0$ mode and $a = e$ and $b = c = s$ in the nonlinear power spectrum. This approximation can be made also from Eq. (2.34) separately by setting $a = e$ and $b = c = s$. The resulting nonlinear power spectrum is then

$$P_e^{(2)}(\omega) = (\Delta\omega)\frac{|\phi_n|^4}{4}F_{ess}(\omega)\int d\omega_1 C_{ss}(\omega_1)\; C_{ss}(\omega-\omega_1), \quad (2.56)$$

with

$$C_{ss}(\omega) = \left|T_{sn}^V(\omega)\right|^2, \quad (2.57)$$
$$T_{en}^V(\omega) = L(\omega)e^{i\omega\tau_{es}}\nu_{es}^{(0)}T_{sn}(\omega), \quad (2.58)$$
$$D_e(\omega) = 1/\Gamma_e(\omega) = (1 - i\omega/\gamma_e)^2, \quad (2.59)$$

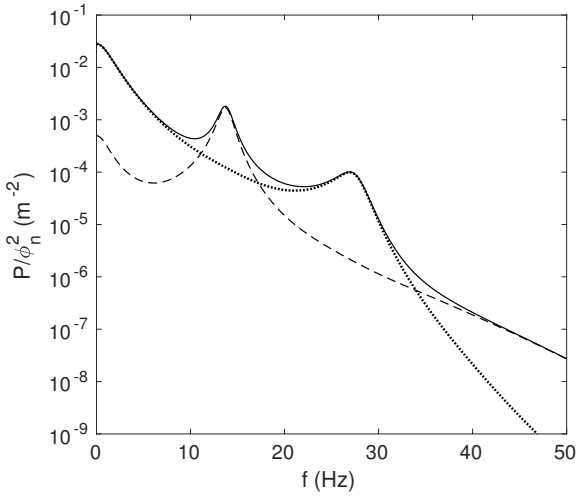

Figure 2.3: Linear, nonlinear, and total contributions to the power spectrum of ϕ_e on a logarithmic scale (dashed, dotted, and solid lines, respectively) for spindle parameters from Table 2.1 and $|\phi_n|^2 = 0.2$ m^4.

with (2.14), (2.39), and (2.43) − (2.49). We add the linear and nonlinear power spectra from Eqs (2.18) and (2.56) to get the total frequency power spectrum

$$P_{tot}(\omega) = P_e(\omega) + (\Delta\omega)\frac{|\phi_n|^4}{4}F_{ess}(\omega)\int d\omega_1 C_{ss}(\omega_1) \times C_{ss}(\omega - \omega_1). \tag{2.60}$$

2.4 Application to sleep-spindle state

In this section, we examine the production of the harmonic of the linear sleep spindle; this harmonic was recently predicted using a simpler nonlinear NFT and then detected in sleep EEG data (Abeysuriya et al., 2014a,b). In the main part of this section we numerically evaluate the nonlinear power spectrum by integrating Eq. (2.52) using Simpson's method, including all terms for the case of spatially uniform activity.

The linear and nonlinear spectra are quadratic and quartic, respectively, in ϕ_n, the amplitude of the input stimulus, a point we have directly verified numerically. Hence, by varying ϕ_n we can adjust the relative normalizations

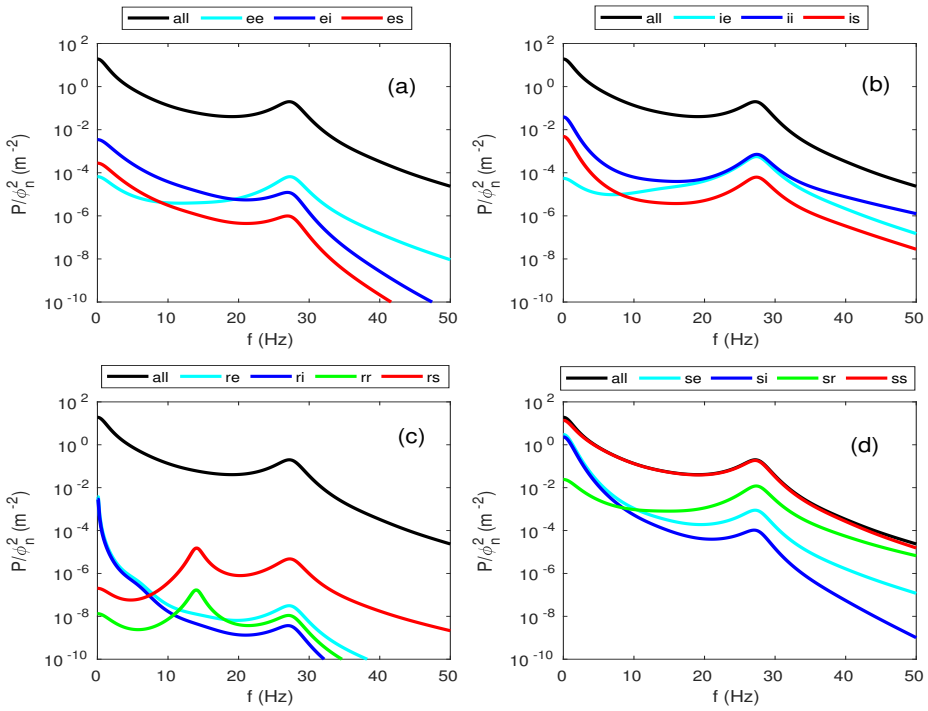

Figure 2.4: Contributions of all terms in the sum over b and c in (2.52) to the total nonlinear spectrum for the sleep spindle parameters from Table 2.1 and $|\phi_n|^2 = 0.2$ m^4 (a) $b = e$, $c = e, i, s$ (b) $b = i$, $c = e, i, s$ (c) $b = r$, $c = e, i, r, s$ (d) $b = s$, $c = e, i, r, s$. The contributions are as labeled in the legend and the highest curve is the total spectrum.

of these two spectral contributions until the ratio of the heights of the linear and nonlinear peaks matches what is seen in the data. For the parameters appropriate to intense sleep-spindles in Table 2.1, taken from (Abeysuriya et al., 2014a), we find that $|\phi_n|^2 = 0.2$ m^4 appropriately normalizes the nonlinear spectrum relative to the linear one. (Note that in (Abeysuriya et al., 2014a) the normalization was not done in Fourier space, so the quoted numerical value and dimensions of ϕ_n were different).

The above steps result in Fig. 2.3, which shows the linear, nonlinear, and total power spectra in the sleep-spindle state. In Fig. 2.3 we see the linear sleep spindle peak at ≈ 13.5 Hz, generated within the intrathalamic loop between the r and s populations in Fig. 2.1 (Abeysuriya et al., 2014a, Kim and Robinson, 2007, Robinson et al., 2002). The convolution of this peak with itself, embodying

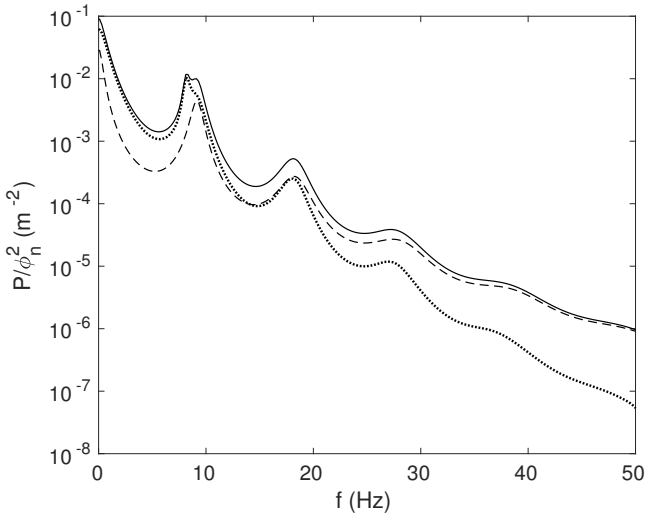

Figure 2.5: Linear, nonlinear and total contributions to the power spectrum of ϕ_e on a logarithmic scale (dashed, dotted, and solid lines, respectively) for EC wake parameters from Table 2.1 and $|\phi_n|^2 = 0.2$ m^4.

wave-wave coalescence, gives rise to the harmonic at approximately 27 Hz seen in the nonlinear spectrum, which also exhibits a zero-frequency peak due to the decay of a spindle wave into another spindle wave and a very-low frequency wave. The total power spectrum exhibits zero-frequency, spindle, and harmonic peaks, with nonlinear contributions of approximately 98%, 7%, and 98%, respectively. We have quantified the percentage of nonlinear contributions by calculating the height of the peak in the power spectrum. The frequencies and widths of the spindle and harmonic peaks match experimental data (Abeysuriya et al., 2014a,b). At high frequencies the spectra fall off steeply, with the nonlinear spectrum falling faster than the linear one.

Previous work made the approximation of neglecting all terms except $b = c = s$ in Eq. (2.52), on the basis that the strongest nonlinearities were expected to be in the s population (Abeysuriya et al., 2014a). We test this by plotting all 16 contributions in the sum over b and c in Eq. (2.52) to the nonlinear spectrum in Figs 2.4(a)−(d). It is seen in Fig. 2.4(d) that the ss term contributes at least 85% of the nonlinear spectrum at all frequencies shown, and over 93% at the spindle harmonic, thereby validating the prior approximation in this brain state. The next strongest terms at the harmonic are sr and se, both of which involve

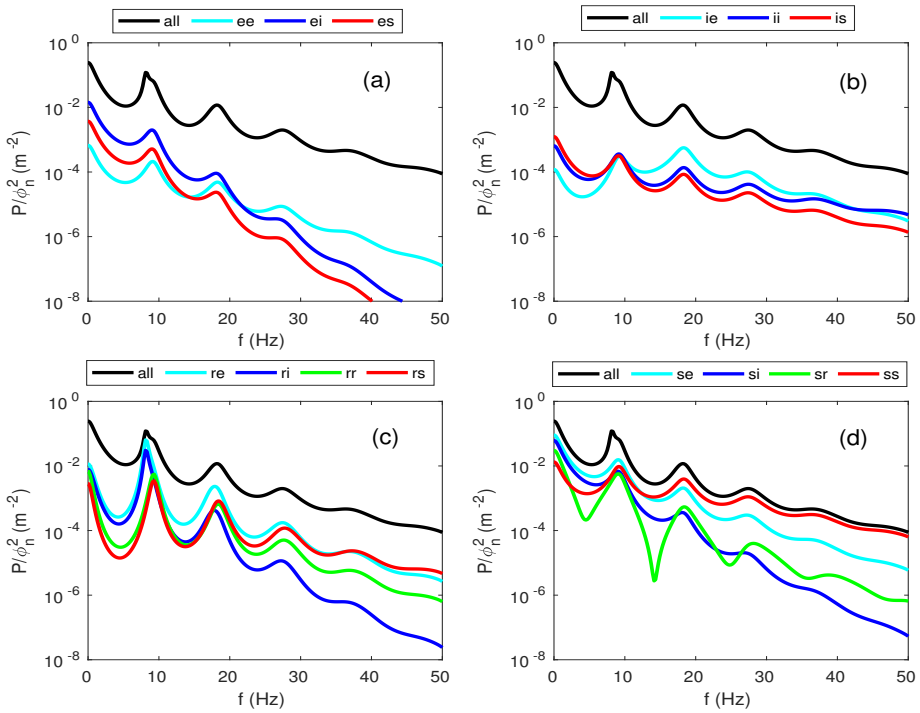

Figure 2.6: Contributions of all terms in thesum over b and c in (2.52) to the total nonlinear spectrum for the wake parameters from Table 2.1 and $|\phi_n|^2 = 0.2$ m^4 (a) $b = e$, $c = e, i, s$ (b) $b = i$, $c = e, i, s$ (c) $b = r$, $c = e, i, r, s$ (d) $b = s$, $c = e, i, r, s$. The contributions are as labeled in the legend and the highest curve is their total.

an s factor. Similarly, at zero frequency the next strongest terms are se and si.

2.5 Application to wake state

The eyes-closed (EC) relaxed waking state typically displays strong alpha and beta peaks, which arise due to positive feedback from cortex to thalamus and back via the s population when this loop is dominant in Fig. 2.1 (Robinson et al., 2002, 2004). The role of nonlinearities in these peaks has long been debated (Freyer et al., 2009, Herrmann, 2001, Stam et al., 1999), but the corticothalamic theory of their generation argues that they are primarily linear, with the beta peak being primarily a linear harmonic generated in the same corticothalamic delay loop (Freyer et al., 2009, Herrmann, 2001, Stam et al., 1999). In this

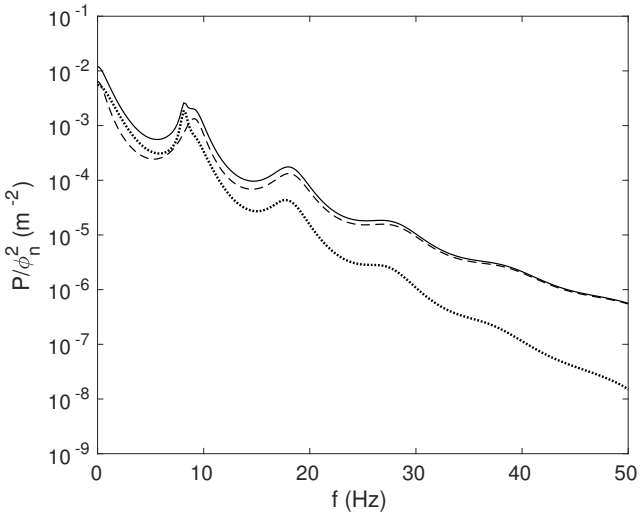

Figure 2.7: Linear, nonlinear and total contributions to the power spectrum of ϕ_e on a logarithmic scale (dashed, dotted, and solid lines, respectively) for EC wake parameters from Table 2.1, except for $G_{es} = 1.8$, and $|\phi_n|^2 = 0.2$ m^4.

section, we apply the same analysis as in the previous section to the EC wake state in order to study the linear and nonlinear spectra and their relative contributions at spectral peaks.

Figure 2.5 shows the linear, nonlinear, and total power spectra in the wake state with parameters from Table 2.1 and $|\phi_n|^2 = 0.2$ m^4, as in the previous section. The linear spectrum shows a zero-frequency peak, an alpha peak at ≈ 9 Hz, and a beta peak at ≈ 18 Hz, in accord with previous numerical results (Abeysuriya et al., 2014a). There is approximately a 10-fold fall-off in power at each harmonic, and a weak third-harmonic feature is seen near 27.5 Hz.

Turning to the nonlinear and total spectra in Fig. 2.5, we see that nonlinear terms contribute around 68% of the power at zero frequency, 46% at the beta peak, and 29% at the third harmonic. Nonlinear effects cause the alpha peak to split in two, with a 55% contribution at the frequency of the linear peak, and an 89% contribution at a new peak at 8 Hz. We explore these features further in Figs 2.6(a)−(d) which shows all 16 contributions in the sum over b and c to Eq. (2.52). In this case, no single term dominates, so the present results significantly improve on those of (Abeysuriya et al., 2014a), which used only

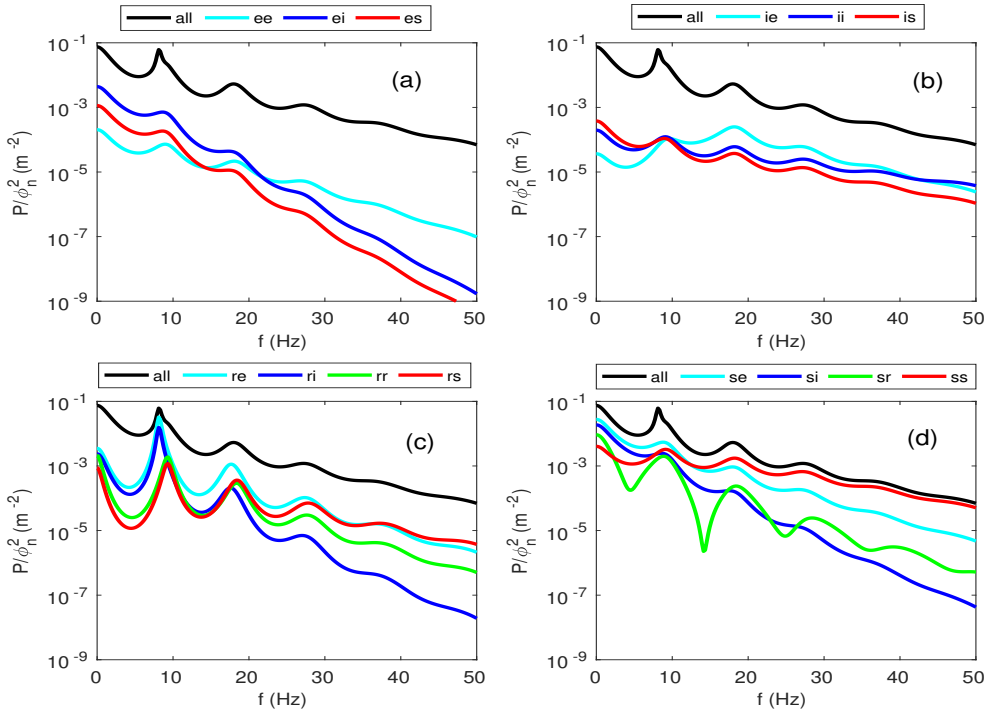

Figure 2.8: Contributions of all terms in the sum over b and c in (2.52) to the total nonlinear spectrum for the wake parameters from Table 2.1, except for $G_{es} = 1.8$, and $|\phi_n|^2 = 0.2$ m^4 (a) $b = e$, $c = e, i, s$ (b) $b = i$, $c = e, i, s$ (c)$b = r$, $c = e, i, r, s$ (d) $b = s$, $c = e, i, r, s$. The contributions are as labeled in the legend and the highest curve is the total spectrum.

the ss term. The largest contributions at zero frequency are se, si, and sr; at the beta frequency they are ss, re with a slightly lower peak frequency, and se; at high frequencies ss and se in Figs 2.6(c) and 2.6(d). The dominant terms at the 8 Hz nonlinear alpha peak are the re and ri terms in 2.6(c), with the se and ss terms providing the largest nonlinear contributions nearer the linear alpha peak in 2.6(d). Examination of the F_{ere} and F_{ese} terms in (2.52) shows that there is an extra downshift of the first term in frequency relative to the second because signals from r must pass through s to reach e in Fig. 2.1, giving rise to additional low-pass filtering relative to signals that travel directly from s to e. At high frequencies the ss term provides the dominant nonlinear contribution.

The case shown in Figs 2.5 and 2.6(a)−(d) has a very strong linear alpha peak and a correspondingly intense nonlinear spectrum. In Figs 2.7 and 2.8(a)−(d)

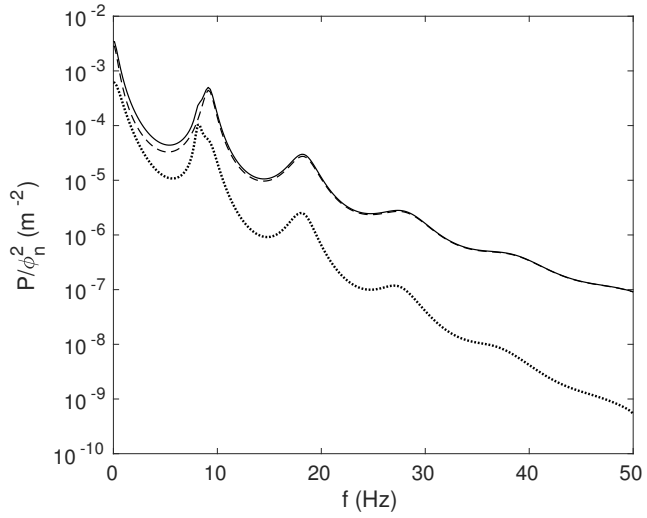

Figure 2.9: Linear, nonlinear and total contributions to the power spectrum of ϕ_e on a logarithmic scale (dashed, dotted, and solid lines, respectively) for EC wake parameters from Table 2.1 and $|\phi_n|^2 = 0.02$ m^4.

we show the corresponding results for a more typical alpha peak strength, obtained by reducing G_{es} to 1.8 from the value of 2.3 in Table 2.1. We see that similar features remain, but the nonlinear contributions are 46%, 72%, 32%, 24%, and 14% at 0, 8.1, 9.1, 18.2, and 27.3 Hz, respectively in Fig. 2.7; these are lower than in Fig. 2.5.

The results in Figs 2.7 and 2.8(a)−(d) are more in accord with the fact that the alpha peak has been found to be predominantly linear, with some nonlinear contributions (Freyer et al., 2009, Stam et al., 1999), but the nonlinear contributions here are still quite large.

The steady state component of input stimulus appears in Eq. (2.7) in the combination form of $\nu_{sn}\phi_n^{(0)}$. The value of $\phi_n^{(0)}$ is significantly smaller in wake state compared to the transient spindle state. Therefore the product of $\nu_{sn}\phi_n^{(0)}$ is found to be smaller in wake than in the spindle state (which usually only lasts a second or so at a time). Considering the possibility that ϕ_n is smaller in the wake state as a test case, we investigate the nonlinear contributions to the spectral peaks for $|\phi_n|^2 = 0.02$ m^4 in Figs 2.9 and 2.10(a)−(d). Here we see that the nonlinear contributions are reduced to 17%, 44%, 11%, 8%, and 5% at 0, 8.1, 9.1, 18.2, and 27.3 Hz, respectively in Fig. 2.9. There is a shoulder present

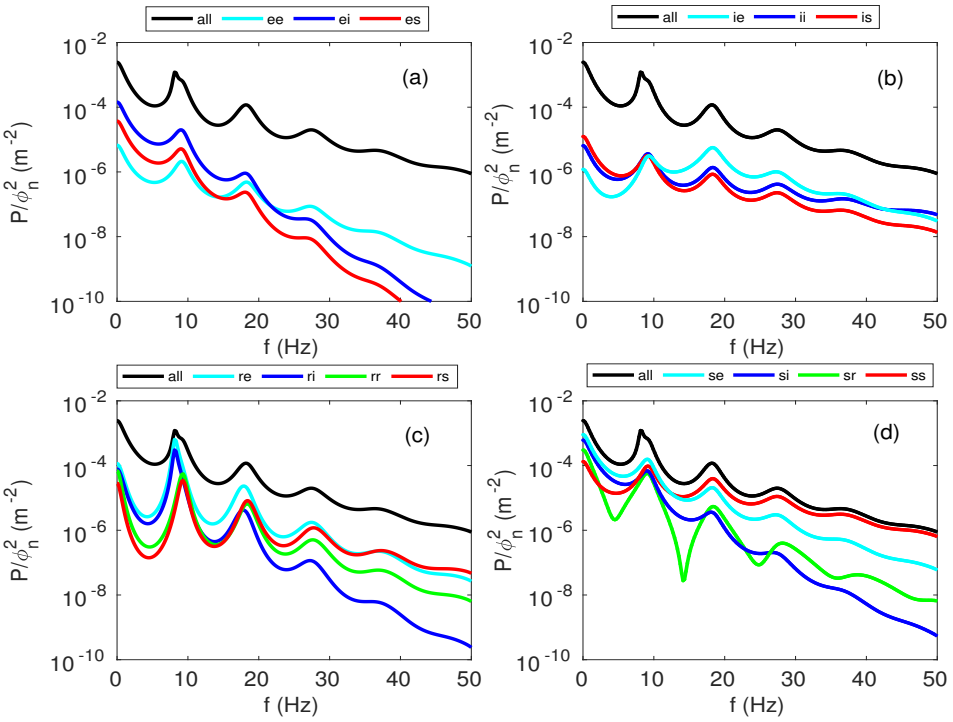

Figure 2.10: Contributions of all terms in the sum over b and c in (2.52) to the total nonlinear spectrum for the wake parameters from Table 2.1 and $|\phi_n|^2 = 0.02$ m^4. (a) $b = e$, $c = e, i, s$ (b) $b = i$, $c = e, i, s$ (c) $b = r$, $c = e, i, r, s$ (d) $b = s$, $c = e, i, r, s$. The contributions are as labeled in the legend and the highest curve is the total spectrum.

in the total power spectrum but we didn't find the double peak as in Fig. 2.5 because the nonlinear contributions are smaller. Notably, the peak at 8 Hz still dominates the nonlinear alpha contribution. The above results, coupled with the observations that the alpha peak is normally not highly nonlinear and is not usually quite sharp as seen in Fig. 2.5.

2.6 Summary and discussion

We have used neural field theory to calculate the linear, nonlinear, and total power spectra of brain activity in the corticothalamic system when firing-rate nonlinearities dominate, and have applied the results to specific wake and sleep states. This generalizes previous work (Abeysuriya et al., 2014a) to remove a

number of assumptions and approximations, and extending and applying the work of Robinson and Roy (2015) to calculate power spectra. Our main results are:

(i) We derived the nonlinear power spectrum via perturbation theory, using transfer functions obtained in previous work (Robinson and Roy, 2015). The results generalized and corrected a preliminary result obtained in that earlier work and expressed the nonlinear spectrum in terms of a sum of convolutions over factors that depend on the neural populations.

(ii) A number of simplified approximations were derived, for cases in which either one neural population and/or activity at large spatial scales dominates the nonlinearity.

(iii) In the sleep-spindle state, it was found that linear activity dominates at the 13.5 Hz spindle resonance but that nonlinearities in the thalamic relay nuclei dominate the nonlinear spectrum at the second harmonic of the linear spindle resonance at 27 Hz, in accord with previous work (Abeysuriya et al., 2014a). The ss term, involving the specific relay nuclei dominates the nonlinear response across the whole spectrum, thereby validating the approximations of (Abeysuriya et al., 2014a). Nonlinear effects also dominate near zero frequency, where a peak is produced by decay of spindle waves into low frequency waves plus other spindle waves.

(iv) Because the ratio of the linear and nonlinear spectra depends on the absolute normalization of the input signal, it proved possible to determine this normalization by fitting the theory to the data in the sleep-spindle state.

(v) In the waking state it is found that multiple terms have comparable contributions to the nonlinear spectrum, and the ss term only dominates at high frequencies, so this generalization is a significant advance over the earlier approximations. Notably, nonlinearities involving the reticular thalamic population can produce a lower-frequency alpha peak at around 8 Hz.

(vi) A better match with the most commonly observed alpha peak strengths and degrees of nonlinearity yields less nonlinearity throughout the spectrum. This implies that corticothalamic loops and/or inputs to the corticothalamic system may be weaker in the waking state than in the transient sleep-spindle state previously studied (Abeysuriya et al., 2014a,b).

Overall, the generalized results have been demonstrated to yield new and

more accurate results and to be more widely applicable than previous, simpler approximations. The observation of a zero-frequency nonlinear peak driven by three-wave decay points the way to further applications to wave decay and coalescence in situations such as steady-state visual evoked-potential experiments, where such phenomena are seen (Herrmann, 2001).

Chapter 3

Nonlinear wave-wave interactions in the brain

Abstract

Neural field theory of the corticothalamic system is used to analyze nonlinear wave-wave interactions in steady state visual evoked potential responses. The nonlinear power spectrum is analytically calculated by convolving the linear power spectrum with itself and other factors. Periodic sine and square wave stimuli are used to generate steady state visual evoked potential responses and to study stimulus-driven nonlinear corticothalamic dynamic interactions. Dual sine drives are then used to analyze the driven dynamics more clearly, without the complicating effects of a background spectrum. Numerical analysis shows that the nonlinear power spectrum embodies key nonlinear features, including harmonic and subharmonic generation, entrainment of alpha rhythm to periodic stimuli at the drive frequency, sum and difference frequencies due to wave-wave coalescence and decay. Further, the scaling properties of the key phenomena observed in nonlinear interactions are studied, verifying some of the theoretical predictions for these being generated by three-wave processes.

3.1 Introduction

Nonlinearity in large-scale brain activity is found in various brain studies including resting state activity (Freyer et al., 2009, Stam et al., 1999), Parkinson's disease (Müller and Robinson, 2018), and epileptic seizures (Breakspear et al., 2006, Robinson et al., 2002). Some experiments have used spatially unstructured periodic flashing light (flicker) to investigate nonlinearities in stimulus-driven cortical dynamics (Herrmann, 2001, Roberts and Robinson, 2012, van der Tweel and Spekreijse, 1969, van der Tweel and Verduyn Lunel, 1965). Steady state visual evoked potentials (SSVEPs) are oscillatory brain responses to such periodic stimuli observed in the measured electroencephalogram (EEG) (Nunez and Cutillo, 1995). Experiments have measured SSVEP responses over a wide range of stimulus frequency in humans (Herrmann, 2001) and animals (Rager and Singer, 1998).

SSVEPs are dominated by cortical activity concentrated at the stimulus frequency as well as its harmonics and subharmonics. Harmonic and subharmonic waves are generated by nonlinearities of the visual system, related to retinal, subcortical, and/or cortical dynamics, although they are not yet fully understood (Abeysuriya et al., 2014a, Herrmann, 2001, Rager and Singer, 1998, Regan, 1989, Roberts and Robinson, 2012). Entrainment and frequency mixing, which involve interactions between stimuli and cortical activity, are also among the nonlinear features found in SSVEP responses to flicker (Herrmann, 2001, Müller and Robinson, 2018, Regan, 1989, Roberts and Robinson, 2012), including entrainment of the alpha rhythm (Herrmann, 2001, Regan, 1989, Roberts and Robinson, 2012).

The interactions between the dynamics of nonlinear brain oscillations and periodic stimuli thus contain rich information about brain functions. Despite the wealth of experimental data characterizing the existence of such nonlinear interactions in large scale brain dynamics, the underlying neurophysiological mechanisms remain poorly understood (Abeysuriya et al., 2014a, Herrmann, 2001, Müller and Robinson, 2018, Regan, 1989, Roberts and Robinson, 2012).

In this study we use neural field theory (NFT) of the corticothalamic system to investigate nonlinear harmonic generation and wave-wave interactions which involve the coalescence ($\omega_1 + \omega_2 \to \omega$) and decay ($\omega \to \omega_1 + \omega_2$) of waves in large

scale brain activity. NFT of the corticothalamic system describes the dynamics of, and interactions between, populations of neurons in the cortex and thalamus based on experimentally measured physiological properties of the brain (Rennie et al., 2002, Robinson et al., 2002, 2004, 1997). The NFT equations are nonlinear in general, and highly nonlinear phenomena like epileptic seizures have been reproduced by them (Breakspear et al., 2006). NFT of the corticothalamic system has successfully described many nonlinear features of brain dynamics and its predictions have been compared to EEG data and other experimental results (Amari, 1977, Beurle, 1956, Breakspear et al., 2006, Buice and Cowan, 2007, Deco et al., 2008, Freeman, 1975, Freyer et al., 2011, Jirsa and Haken, 1996, Nunez and Cutillo, 1995, Robinson et al., 2002, 2004, 1997, Steyn-Ross et al., 2005, Wilson and Cowan, 1973, Wright and Liley, 1996). NFT has also successfully reproduced nonlinear features in seizure dynamics (Breakspear et al., 2006, Robinson et al., 2002), and explained harmonic generation during sleep spindles (Abeysuriya et al., 2014a). NFT of the corticothalamic system was also previously used to reproduce many phenomena seen in SSVEP experiments (Roberts and Robinson, 2012, Robinson et al., 2002, 1997). In (Roberts and Robinson, 2012), periodic stimuli were used to drive the system and resulted in many nonlinear interactions consistent with experiments (Herrmann, 2001). A recent study (Müller and Robinson, 2018) found similar nonlinear interactions between the drive frequency and a Parkinsonian beta (≈ 26 Hz) resonance using a neural field model of the corticothalamic-basal ganglia system.

Although NFT of the corticothalamic system was used in a previous numerical study (Roberts and Robinson, 2012) to explore some nonlinear interactions in large scale brain activity, much remains to be understood regarding nonlinear features in SSVEPs, including scaling properties and relationships to recent analytic perturbation expansions (Robinson and Roy, 2015). In this paper NFT of the corticothalamic system is applied to quantitatively understand harmonic generation in the wake state and the wider question of wave-wave interactions in SSVEP experiments. We verify key results from Roberts and Robinson (2012), more recent theoretical analyses (Ferdousi et al., 2019, Robinson and Roy, 2015), and new predictions obtained here, using the recently published NFTsim software (Sanz-Leon et al., 2018) and explain nonlinear interactions between brain activity and periodic driving by incorporating sinusoidal and square-wave

stimulation into the corticothalamic model. In order to isolate nonlinear interactions more clearly, we study the interactions between two sinusoidal drives to avoid the complicating effects of interactions with the background activity spectrum. Predictions of the scalings of the strong peaks seen in the SSVEP power spectra are made and tested and new wave-wave interactions are also identified.

The structure of the chapter is as follows. Section 3.2 reviews the corticothalamic neural field model. In Sec. 3.3 we calculate the linear and nonlinear power spectrum for this system. Section 3.4 presents the theory for sinusoidal drive. The periodically driven nonlinear features of the SSVEP spectra are explored in Sec. 3.5, while in Sec. 3.6 we study the scalings of the power of spectral peaks for sine drive. Section 3.7 presents the theory for square drive and explored nonlinear features. In Sec. 3.8, we use two sine drives to study the nonlinear interactions in SSVEPs responses. Section 3.9 concludes and discusses future directions.

3.2 Theory

In this section, we briefly summarize the corticothalamic model used in previous work (Abeysuriya et al., 2014a, Roberts and Robinson, 2012, Robinson et al., 2002, 2004, 1997).

3.2.1 Corticothalamic system

The corticothalamic system illustrated in Fig. 3.1 generates many of the observable signals used to monitor brain activity, in particular electroencephalographic signals detected through scalp electrodes. Our model includes four internal neural populations and their interactions: the cortical excitatory (e) and inhibitory (i) populations, plus thalamic reticular (r) and thalamic relay (s) populations, and external input (ϕ_n) (Robinson et al., 2002). The external input driven the system via thalamic relay population.

Each population has a mean cell-body potential V_a, driven by pulse rates ϕ_b

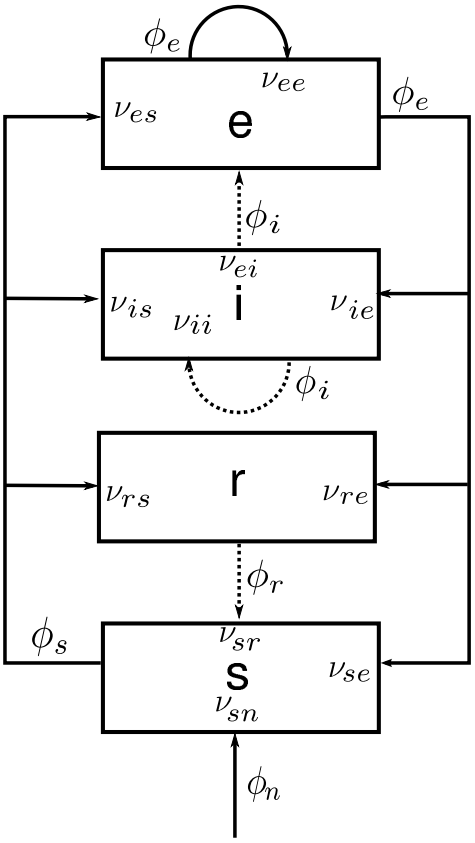

Figure 3.1: The diagram shows the connectivities of cortical (excitatory e, inhibitory i) and thalamic (relay s, reticular r) neural populations. The parameter ν_{ab} quantifies the connection to population a from population b and the ϕ_a are axonal pulse rates. Excitatory connections are shown with solid lines, and inhibitory connections are shown with dotted lines.

from presynaptic populations b, with

$$D_\alpha(t)V_a(\mathbf{r},t) = \sum_b \nu_{ab}\phi_b(\mathbf{r}, t-\tau_{ab}), \tag{3.1}$$

$$D_\alpha = \frac{1}{\alpha\beta}\frac{d^2}{dt^2} + \left(\frac{1}{\alpha}+\frac{1}{\beta}\right)\frac{d}{dt} + 1, \tag{3.2}$$

where $\mathbf{r}$ denotes the spatial coordinate on the 2D cortical sheet and t the time. The primary topographic map established by one-to-one reciprocal projections between cortex and thalamus enables the same $\mathbf{r}$ to be associated with points in different populations that map to one another. The sum in Eq. (3.1) has b

running over e, i, r, s, n, and all potentials are measured relative to resting. The connection strength ν_{ab} in Eq. (3.1) is defined as $\nu_{ab} = s_{ab}N_{ab}$ where N_{ab} is the mean number of synapses to each neuron in population a from neurons of type b, and s_{ab} is the mean time-integrated strength of the soma response per incoming spike. In Eq. (3.1), $\phi_b(\mathbf{r}, t - \tau_{ab})$ is the mean spike arrival rate from neurons b, allowing for a time delay τ_{ab} due to any discrete anatomical separations between different populations (Roberts and Robinson, 2012, Robinson et al., 2004). The parameters β and α are the characteristic rise rate and decay rate, respectively, of the cell-body potential produced by an impulse at a dendritic synapse, allowing for the effects of synaptic, dendritic, and soma dynamics. For the system in Fig. 3.1, the only nonzero delays τ_{ab} are $\tau_{es} = \tau_{is} = \tau_{se} = \tau_{re} = t_0/2$ where t_0 is the total corticothalamic loop delay.

The mean potential V_a generates a mean firing rate Q_a via a sigmoid response function, with

$$Q_a(\mathbf{r}, t) = S\big[V_a(\mathbf{r}, t)\big], \tag{3.3}$$

where S expresses the nonlinearity. We approximate this function as (Freeman, 1975, Wilson and Cowan, 1973)

$$S[V_a(\mathbf{r}, t)] = \frac{Q_{\max}}{1 + \exp\left[-\{V_a(\mathbf{r}, t) - \theta\}/\sigma'\right]}, \tag{3.4}$$

where $Q_{\max}$ is the maximum possible firing rate for the population, θ is the mean threshold voltage, and $\sigma = \sigma'\pi/\sqrt{3}$ is the standard deviation of the distribution of thresholds in the population.

The firing rate Q_a is the source of ϕ_a, which approximately obeys the damped wave equation (Robinson et al., 2002, 1997)

$$D_a(\mathbf{r}, t)\phi_a(\mathbf{r}, t) = Q_a(\mathbf{r}, t), \tag{3.5}$$

$$D_a(\mathbf{r}, t) = \frac{1}{\gamma_a^2}\frac{\partial^2}{\partial t^2} + \frac{2}{\gamma_a}\frac{\partial}{\partial t} + 1 - r_a^2\nabla^2, \tag{3.6}$$

where r_a is the mean axon length in the population a, v_a is the pulse velocity, $\gamma_a = v_a/r_a$ is an effective damping rate, and ∇^2 is the Laplacian operator. In populations other than e, r_a is so small that one can set $D_a = 1$.

There are 16 possible connections between the four neural populations in

Fig. 3.1, but only 10 of them are nonzero in our model, as seen in Fig. 3.1. We assume that the number of connections to and between cortical populations is proportional to the number of synapses available (Braitenberg and Schüz, 1998, Wright and Liley, 1996). This random connectivity approximation implies that $N_{ib} = N_{eb}$ for all b. If the synaptic strengths only depend on the presynaptic population then $\nu_{ee} = \nu_{ie}, \nu_{ei} = \nu_{ii}$, and $\nu_{es} = \nu_{is}$ (Robinson et al., 2004), giving eight distinct connection strengths. The connections ν_{ei} and ν_{sr} are inhibitory (negative) while the other connections in the model are excitatory (positive).

3.3 Power spectrum

In this section, we briefly review the calculation of the linear power spectrum (Abeysuriya et al., 2014a, Robinson et al., 2004) using the system transfer function, then its use to calculate the nonlinear power spectrum for the stimulus-driven system via perturbation expansion.

3.3.1 Linear spectrum

Previous work has successfully modeled normal brain states by considering their activity to be due to perturbations from steady states (Deco et al., 2008, Robinson et al., 2002, 2004, 1997). Hence, we expand the fields ϕ_a in perturbations relative to a fixed point as

$$\phi_a(\kappa) = \phi_a^{(0)}(\kappa) + \phi_a^{(1)}(\kappa) + \phi_a^{(2)}(\kappa) + ..., \tag{3.7}$$

where $\kappa = (\mathbf{k}, \omega)$ and the superscripts indicate the order of perturbation due to external activity, ϕ_n which are taken to have only zeroth and first order perturbations.

Transfer functions for the systems shown in Fig. 3.1 have been derived before,

mainly in the form required to express ϕ_e in terms of ϕ_n as

$$T_{en}(\mathbf{k},\omega) = \frac{\phi_e^{(1)}(\mathbf{k},\omega)}{\phi_n^{(1)}(\mathbf{k},\omega)}, \tag{3.8}$$

$$= \frac{L^2 G_{esn} e^{i\omega t_0/2}}{(1-L^2G_{srs})(1-G_{ei}L)} \frac{1}{k^2 r_e^2 + q^2 r_e^2}, \tag{3.9}$$

$$q^2 r_e^2 = \left(1-\frac{i\omega}{\gamma_e}\right)^2 - \frac{1}{1-G_{ei}L}\left[LG_{ee} + \frac{\left[L^2G_{ese}+L^3G_{esre}\right]e^{i\omega t_0}}{1-L^2G_{srs}}\right], \tag{3.10}$$

$$L(\omega) = \left(1-\frac{i\omega}{\alpha}\right)^{-1}\left(1-\frac{i\omega}{\beta}\right)^{-1}. \tag{3.11}$$

The spatiotemporal power spectrum of $\phi_e^{(1)}$ is then

$$P_e(\mathbf{k},\omega) = |T_{en}(\mathbf{k},\omega)|^2 \; |\phi_n^{(1)}(\mathbf{k},\omega)|^2. \tag{3.12}$$

To focus on the temporal frequency spectrum, we must integrate over $\mathbf{k}$, with

$$P_e(\omega) = \int d^2\mathbf{k} \; |\phi_n^{(1)}(\mathbf{k},\omega)|^2 \; |T_{en}(\mathbf{k},\omega)|^2. \tag{3.13}$$

The background system is estimated by integrating Eq. (3.13) over all $\mathbf{k}$ for white noise input with $|\phi_n^{(1)}(\mathbf{k},\omega)| =$ constant. We get the analytic power spectrum, which is (Roberts and Robinson, 2012, Robinson et al., 2002, 2004, 1997)

$$P_e(\omega) = \frac{\pi \; |\phi_n|^2}{r_e^2}\left|\frac{L^2G_{esn}}{(1-G_{ei}L)(1-L^2G_{srs})}\right|^2 \left|\frac{\text{Arg }(q^2r_e^2)}{\text{Im }(q^2r_e^2)}\right|, \tag{3.14}$$

where Arg denotes the complex argument and Im is the imaginary part. The uniform $\mathbf{k} = \mathbf{0}$ mode is the least stable and it plays a significant role in the dynamics (Robinson et al., 1997). For the $\mathbf{k} = \mathbf{0}$ mode, the first order power spectrum is

$$P_e(\omega) = (\Delta k)^2 |\phi_n|^2 \left|\frac{L^2G_{esn}}{(1-G_{ei}L)(1-L^2G_{srs})}\right|^2 \frac{1}{|q^4 r_e^4|}. \tag{3.15}$$

3.3.2 Nonlinear spectrum

Since the work in (Roberts and Robinson, 2012), systematic perturbation expansion of the nonlinear wave-wave interactions in NFT has been carried out (Robinson and Roy, 2015) and nonlinear harmonics in sleep and wake states have been verified in (Ferdousi et al., 2019). Here we extend this approach to derive scalings of spectral features due to specific wave-wave interactions and briefly summarize the form of the nonlinear spectrum.

The power spectrum of ϕ_a can be written as (Robinson and Roy, 2015)

$$\begin{aligned} P_a(\kappa) &= \left|\phi_a(\kappa) - \phi_a^{(0)}\right|^2, && (3.16)\\ &= \left|\phi_a^{(1)}(\kappa) + \phi_a^{(2)}(\kappa) + ...\right|^2, && (3.17)\\ &\approx \left|\phi_a^{(1)}(\kappa)\right|^2 + 2\ \mathrm{Re}\ \left[\phi_a^{(1)}(\kappa)\ \phi_a^{(2)*}(\kappa)\right] \\ &\quad + |\phi_a^{(2)}(\kappa)|^2 + ..., && (3.18) \end{aligned}$$

where $\phi_a^{(0)}$ is the steady state value of ϕ_a, and terms beyond fourth order have been omitted from Eq. (3.18).

We drive our system by adding a periodic stimulus ϕ_d to ϕ_n to calculate the SSVEPs vs. stimulus frequency and amplitude. The field ϕ_a has parts ϕ_A and ϕ_D due to $\phi_n^{(1)}$ and $\phi_d^{(1)}$, respectively, with

$$\begin{aligned} \phi_a^{(1)}(\kappa) &= T_{an}(\kappa)\phi_n^{(1)}(\kappa) + T_{an}(\kappa)\phi_d^{(1)}(\kappa), && (3.19)\\ &= \phi_A + \phi_D. && (3.20) \end{aligned}$$

The second order term in the expansion of ϕ_a is

$$\phi_a^{(2)}(\kappa) = (\phi_A + \phi_D) \otimes (\phi_A + \phi_D), \quad (3.21)$$

where $\otimes$ denotes a weighted convolution whose exact from is not relevant to this part of our argument, which focuses only on which terms are nonzero and their scalings (Robinson and Roy, 2015); details of this convolution can be found in (Robinson and Roy, 2015) and below.

Table 3.1: Model parameter values from (Roberts and Robinson, 2012), ($ab = es, is, se, re$).

Quantity	Symbol	Wake	Unit
Voltage decay rate	α	80	s^{-1}
Voltage rise rate	β	800	s^{-1}
Voltage decay rate	α_{sr}	10	s^{-1}
Voltage rise rate	β_{sr}	60	s^{-1}
Corticothalamic delay	τ_{ab}	40	ms
Cortical damping rates	γ_e	116	s^{-1}
Other damping rates	$\gamma_{i,r,s}$	12000	s^{-1}
Threshold spread	σ'	3.8	mV
Maximum firing rate	$Q_{\max}$	250	s^{-1}
Axonal ranges:			
	r_e	86	mm
	$r_{i,r,s}$	1.5	mm
Connection strengths:			
e from e	ν_{ee}	1.3	mV s
e from i	ν_{ei}	-2.9	mV s
e from s	ν_{es}	0.13	mV s
r from e	ν_{re}	0.67	mV s
r from s	ν_{rs}	2.9	mV s
s from e	ν_{se}	2.9	mV s
s from r	ν_{sr}	-0.57	mV s
Subthalamic input to s	$\nu_{sn}\phi_n^{(0)}$	0.14	mV
Steady state spike rates:			
e	$\phi_e^{(0)}$	1.4	s^{-1}
r	$\phi_r^{(0)}$	12.4	s^{-1}
s	$\phi_s^{(0)}$	1.5	s^{-1}
Drive amplitude	A_D	2.8	s^{-1}
Standard deviation	σ_n	1	s^{-1}
Mean value of noise	$\phi_n^{(0)}$	18	s^{-1}

We next expand the second term in (3.18) in terms of ϕ_A and ϕ_D as

$$\begin{aligned}2\mathrm{Re}\left[\phi_a^{(1)}\phi_a^{(2)*}\right] = 2\mathrm{Re}\Big[&\phi_A(\phi_A\otimes\phi_A)^* + \phi_A(\phi_A\otimes\phi_D)^* \\ &+\phi_D(\phi_A\otimes\phi_D)^* + \phi_D(\phi_A\otimes\phi_A)^* + \phi_A(\phi_D\otimes\phi_D)^* \\ &+\phi_D(\phi_D\otimes\phi_D)^* + \phi_A(\phi_D\otimes\phi_A) + \phi_D(\phi_D\otimes\phi_A)\Big],\end{aligned} \tag{3.22}$$

where we have omitted the arguments κ for compactness. Each of the terms on the right of (3.22) involves the product of three ϕ_A and ϕ_D. If ϕ_A is random-phase, any term with an odd number of factors of ϕ_A averages to zero for any nonzero frequency. This leaves terms with two factors of ϕ_A and one of ϕ_D, or three factors of ϕ_D, both of which also average to zero because they contain odd numbers of factors of ϕ_D. An exception to this conclusion would occur when the phase of ϕ_A is changed by ϕ_D (e.g., via entrainment), but we do not consider this case analytically here.

To lowest nonlinear order, now the power spectrum can now be written as

$$\begin{aligned}P_a(\kappa) &\approx |\phi_A|^2 + |\phi_D|^2 + 2\ \mathrm{Re}\Big[\ldots\Big] + |\phi_A\otimes\phi_A|^2 \\ &+ |\phi_D\otimes\phi_D|^2, \qquad (3.23)\\ &= \left\langle P_a^{(1)}\right\rangle + \left\langle P_d^{(1)}\right\rangle + \left\langle 2\mathrm{Re}\Big[\ldots\Big]\right\rangle + \left\langle P_a^{(2)}\right\rangle \\ &+ \left\langle P_d^{(2)}\right\rangle, \qquad (3.24)\end{aligned}$$

where the angle brackets denote averages over the phase of the inputs and the ellipsis stands for the terms in Eq. (3.22), which are zero in the random-phase limit. The terms on the right of Eq. (3.24) scale as powers of ϕ_D, with the first and fourth terms being independent of ϕ_D, the second being quadratic in ϕ_D, the third having contributions from constant up to cubic for special case where $\omega_D = 2\omega$ and $\omega = 2\omega_D$, and the last being quartic.

The second order power spectrum can be written as (Ferdousi et al., 2019)

$$P_a^{(2)}(\kappa) = (\Delta\kappa)\frac{|\phi_n|^4}{4}\sum_{bc} F_{abc}(\kappa)\int d\kappa_1 C_{bc}(\kappa_1)C_{bc}(\kappa-\kappa_1), \tag{3.25}$$

with

$$F_{abc}(\kappa) = \Gamma_b(\kappa)\Gamma_c^*(\kappa)S_b^{(2)}S_c^{(2)}\hat{T}_{ab}(\kappa)\hat{T}_{ac}^*(\kappa), \tag{3.26}$$

$$\Gamma_b(\kappa) = \left[\left(1 - \frac{i\omega}{\gamma_b}\right)^2 + k^2 r_b^2\right]^{-1}, \tag{3.27}$$

$$S_b^{(2)} = \frac{2Q_b^3}{\sigma'^2 Q_{\max}^2} - \frac{3Q_b^2}{\sigma'^2 Q_{\max}} + \frac{Q_b}{\sigma'^2}, \tag{3.28}$$

$$\hat{\mathbf{T}} = (\mathbf{I} - \mathbf{X})^{-1}, \tag{3.29}$$

$$X_{ab}(\kappa) = L_a\Gamma_a(\kappa)S_a^{(1)}e^{i\omega\tau_{ab}}\nu_{ab}^{(0)}, \tag{3.30}$$

$$S_a^{(1)} = \frac{Q_a}{\sigma'}\left(1 - \frac{Q_a}{Q_{\max}}\right), \tag{3.31}$$

$$C_{bc}(\kappa) = T_{bn}^V(\kappa)T_{cn}^{V*}(\kappa), \tag{3.32}$$

$$T_{an}^V(\kappa) = L_a\left[e^{i\omega\tau_{an}}\nu_{an}^{(0)} + \sum_b e^{i\omega\tau_{ab}}\nu_{ab}^{(0)}T_{bn}(\kappa)\right], \tag{3.33}$$

where $\mathbf{I}$ is the identity matrix and $\hat{\mathbf{T}}$ and $\mathbf{X}$ are matrices of the elements T_{ab} and X_{ab}, respectively. The sum in Eq. (3.33) extends over all populations and T_{bn} is the transfer function to $\phi_b^{(1)}$ from an external input $\phi_n^{(1)}$ and $\phi_d^{(1)}$. Equation (3.25) embodies three-wave interactions at κ, and $\kappa - \kappa_1$, wave-wave coalescence and decay.

3.4 SSVEPs for sinusoidal drive

In this section we drive the system with periodic external stimuli plus background noise to generate SSVEP responses in the presence of normal brain activity. The key features of such stimulus-driven activity then can be used to evaluate the predictions made in the previous section. External stimuli ϕ_n drive the brain via the thalamic relay nucleus. Resting state EEG spectra have been successfully generated for white noise drive (Roberts and Robinson, 2012, Robinson et al., 2002, 2004, 2005, 1997), where the external stimuli ϕ_n are so complex that they do not favor any particular frequency in the range of interest (Lopes da Silva et al., 1974, Stam et al., 1999). Sinusoidally modulated periodic stimuli generate SSVEPs, also predicted by the NFT model, and their features in the

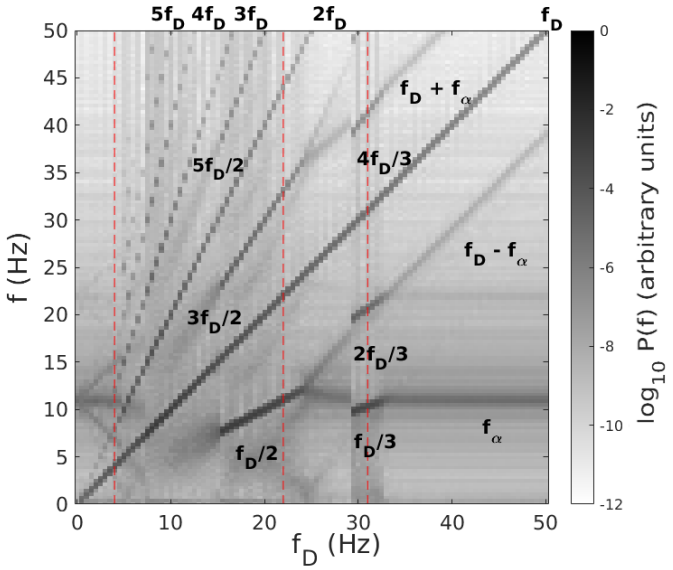

Figure 3.2: Spectral response for $f_D = 0 - 50$ Hz. The physiological parameters are adapted from (Roberts and Robinson, 2012). Darker shading denotes higher power. The three vertical dashed red lines mark the 4, 22, and 31 Hz drive frequencies that are investigated in more detail in subsequent sections.

linear regime have been shown to be consistent with experiment (Robinson et al., 2008).

Here we study their nonlinear regime where the drive is strong by modeling the external input ϕ_n as

$$\phi_n(t) = \phi_n^{noise}(t) + \phi_d(t), \tag{3.34}$$

where ϕ_n^{noise} is Gaussian white noise with mean $\phi_n^{(0)}$, standard deviation σ_n, and ϕ_d is a periodic signal with zero mean. We use the sinusoidal drive

$$\phi_d(t) = A_D \sin(2\pi f_D t), \tag{3.35}$$

where A_D is the amplitude and f_D is the frequency. A major benefit of using a single sinusoid to drive the system is that we avoid ambiguity between harmonic peaks present in any nonsinusoidal periodic drive and harmonic peaks generated by the nonlinear interactions.

Roberts and Robinson (2012) used a similar method to explore SSVEP

responses to sine wave stimuli and studied particular nonlinear properties present in the responses. Their results reproduced multiple nonlinear features seen in experiments performed by Herrmann (2001) using a square-wave drive over a wide range of drive frequency. In order to verify our methods and reconfirm some of the key results in (Roberts and Robinson, 2012), we use the recently published NFTsim software (Sanz-Leon et al., 2018) to reproduce their Fig. 3.2. We then further study the nonlinear responses in the light of subsequent theoretical developments (Ferdousi et al., 2019, Robinson and Roy, 2015) and compare the results with the resulting predictions, including those made in Sec. 3.3.2.

We use the parameters from previous work (Roberts and Robinson, 2012) and calculate the power spectra for responses evoked by a range of drive frequencies $1-50$ Hz. We then change stimulus variables to investigate their impacts. Figure 3.2 shows the model response spectrum as a function of f_D for the drive given by Eq. (3.35). Key features include:

(i) Generation of harmonics, subharmonics, fractional harmonics, entrainment, and sum and difference frequencies due to wave-wave coalescence and decay, in very good agreement with those reported by Roberts and Robinson (2012), all superposed on the background linear spectrum given by Eqs (3.14) and (3.15).

(ii) The main harmonics generated by the drive are the first to fifth, which were also seen previously (Herrmann, 2001). Subharmonics and fractional harmonics found in the spectra include $1/3, 2/3, 4/3$, and $1/2, 3/2, 5/2$, of which only the $1/2$ subharmonic was clearly visible in that earlier study's corresponding response spectrum (Herrmann, 2001).

(iii) Entrainment to f_D is observed in various regions. We see that resulting suppression of the background alpha activity at $f_\alpha \approx 11$ Hz in favor of f_D happens for 4 Hz $\lesssim f_D \lesssim$ 15 Hz. Entrainment of alpha activity is observed by the $1/2$ subharmonic for 15 Hz $\lesssim f_D \lesssim$ 25 Hz, and by the $1/3$ subharmonic for 29 Hz $\lesssim f_D \lesssim$ 32.5 Hz.

(iv) Sum and difference frequencies, $f_\pm = |f_D \pm f_\alpha|$ are seen at $f_D \lesssim 5$ Hz $(f_\alpha \pm f_D)$ and $f_D \gtrsim 30$ Hz $(f_D \pm f_\alpha)$. These peaks are due to nonlinear interactions between the drive signal and background activity, expressed via the convolution in Eq. (3.25). These interactions are equivalent to wave coalescence

and decay (i.e., wave mixing) in other branches of nonlinear wave physics and have also been observed in SSVEP experiments using two distinct drive frequencies (Regan, 1989, Roberts and Robinson, 2012). Strong peaks at $f_\pm$ demand a sharp alpha peak (Roberts and Robinson, 2012), so in regions where the alpha peak is either broadened or suppressed, peaks at $f_\pm$ are not observed, as can be seen for 5 Hz $\lesssim f_D \lesssim$ 25 Hz.

(v) The strong response observed at $f_D/2$ for 15 Hz $\lesssim f_D \lesssim$ 25 Hz, where the alpha rhythm is suppressed due to entrainment, can be attributed to the occurrence of a triple resonance involving entrained alpha activity with $f_\alpha \approx f_D/2 \approx f_D - f_\alpha$. Similar strong responses at $f_D/3$, $2f_D/3$, and $4f_D/3$ are also seen for 29 Hz $\lesssim f_D \lesssim$ 32.5 Hz. These enhancements can be attributed to double resonances between f_α and $f_D/3$, between $f_D - f_\alpha$ and $2f_D/3$, and between $f_D + f_\alpha$ and $4f_D/3$.

3.5 Spectral features

In the previous section we saw strong peaks in the power spectrum of the SSVEP responses at harmonics, subharmonics, and fractional harmonics of the drive frequency, plus sum and difference peaks that involve the linear alpha peak, as seen in Fig. 3.2. Hence, in this section, we focus on these dominant peaks.

A stimulus frequency of 4 Hz, marked by a dashed red line in Fig. 3.2, produces several peaks below 20 Hz. To explore these features in more detail, the corresponding power spectrum is plotted in Fig. 3.3(a). The main peaks correspond to f_D, $f_\alpha - f_D \approx 7$ Hz, $2f_D$, $f_\alpha \approx 11$ Hz, $3f_D$, and $f_\alpha + f_D \approx 15$ Hz, thus reflecting multiharmonic generation and wave coalescence and decay. These nonlinear features were also seen in earlier theoretical and experimental studies (Herrmann, 2001, Roberts and Robinson, 2012).

Figure 3.3(b) shows the power spectrum for $f_D = 22$ Hz, with strong peaks seen at subharmonic and fractional harmonic frequencies of $f_D/2 \approx 11$ Hz (which makes a double resonance with f_α), $3f_D/2 \approx 33$ Hz (which makes a double resonance with $f_\alpha + f_D$), and $5f_D/2 \approx 55$ Hz. The 1/2 subharmonic was also reported experimentally (Herrmann, 2001) for square wave drive as

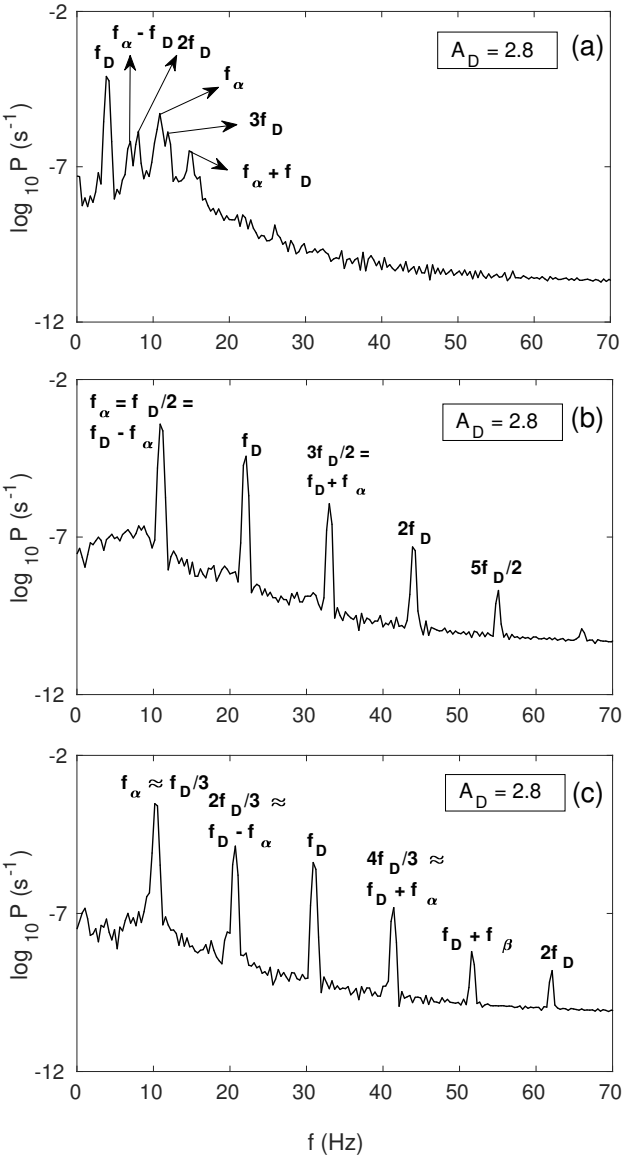

Figure 3.3: Power spectra of model SSVEPs for the three drive frequencies marked by dashed red lines in Fig. 3.2. (a) $f_D = 4$ Hz. (b) $f_D = 22$ Hz. (c) f_D= 31 Hz.

well as in simulations of sine wave drive (Roberts and Robinson, 2012).

The last case we consider has $f_D = 31$ Hz, also marked by a dashed red line in Fig. 3.2. The power spectrum of the response exhibits multiple fractional subharmonics in Fig. 3.3(c), at $f_D/3 \approx 10.3$ Hz (which makes a double resonance

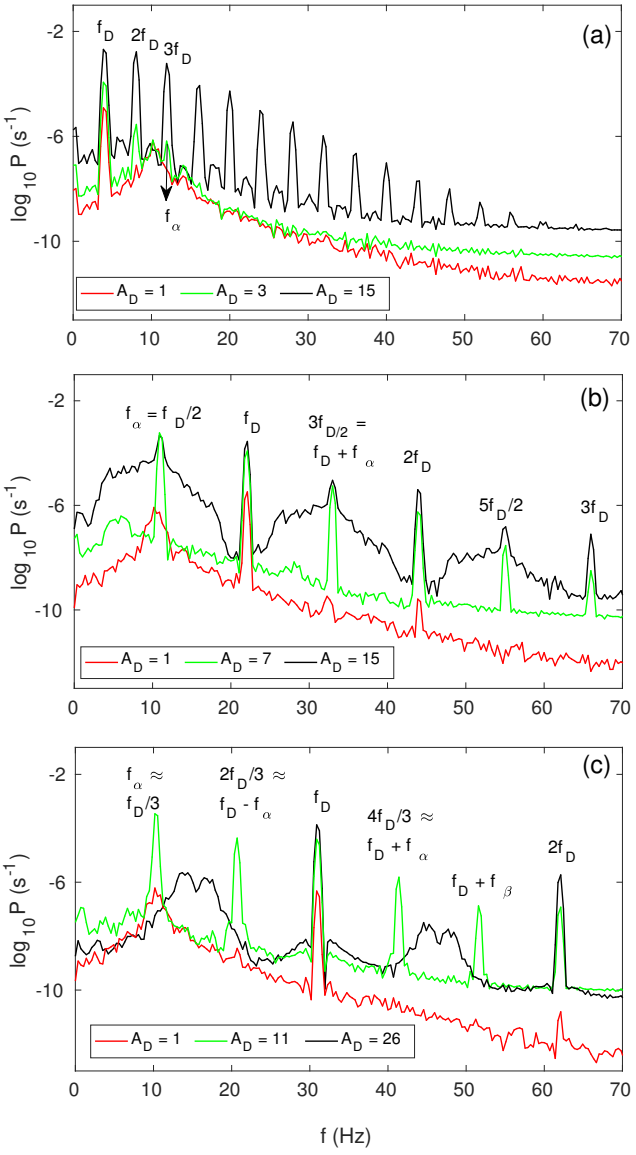

Figure 3.4: Power spectra of SSVEP responses calculated for three distinct drive frequencies, with various amplitudes as shown in the legends, using the parameters in Table 3.1. (a) $f_D = 4$ Hz. (b) $f_D = 22$ Hz. (c) $f_D = 31$ Hz.

with f_α), $2f_D/3 \approx 20.7$ Hz (which makes a double resonance with $f_\alpha - f_D$), and $4f_D/3 \approx 41.3$ Hz (which makes a double resonance with $f_\alpha + f_D$). These nonlinear features were not visible in the experiment (Herrmann, 2001). In their study (Roberts and Robinson, 2012), these phenomena were visible, but were significantly weaker.

The amplitude of the periodic stimulus also affects the nonlinear spectral features. Going beyond earlier analyses, we probe its impact on the power spectra for $f_D = 4$, 22, and 31 Hz. Figure 3.4(a) shows spectra calculated for $f_D = 4$ Hz and varying amplitude A_D. For $A_D = 1$, spectral peaks are found at f_D and $f_\alpha \approx 10$ Hz and nonlinear harmonic and subharmonic peaks are not observed. At $A_D = 3$, strong peaks are present at f_D, $2f_D$, and $f_\alpha \approx 10$ Hz, with smaller peaks seen at $2f_D$ and $f_D + f_\alpha \approx 14$ Hz. Note that this spectrum is similar to Fig. 3.3(a) which had the same f_D and a similar drive amplitude, $A_D = 2.8$. Increasing A_D to 15 causes multiple harmonics to appear in the spectrum, which persist and sharpen at higher A_D (not shown).

We observed in Fig. 3.3(b) that $f_D = 22$ Hz and $A_D = 2.8$ gave rise to harmonics and half-harmonics. However, $A_D = 1$ only produces strong peaks at $f_\alpha \approx 10$ Hz, f_D, and $2f_D$, as seen in Fig. 3.4(b). At $A_D = 7$ strong peaks are seen at $f_\alpha \approx 11$ Hz, f_D, $3f_D/2 \approx 33$ Hz, $2f_D$, $5f_D/2 \approx 55$ Hz, and $3f_D$, similar to those in Fig. 3.3(b) for $A_D = 2.8$. The alpha peak is shifted from 10 Hz for higher amplitude and a triple resonance occurs at $f_D/2$ because for this particular frequency $f_\alpha = f_D/2 = f_D - f_\alpha = 11$ Hz. A further increase of A_D gradually broadens the fractional subharmonics at $f_D/2$, $3f_D/2$, and $5f_D/2$, while the peaks at multiples of f_D remain narrow and sharp, as shown in Fig. 3.4(b) for $A_D = 15$.

For $f_D = 31$ Hz, Fig. 3.4(c) shows that $A_D = 1$ only produces a broad peak at $f_\alpha \approx 10$ Hz and a relatively small but narrow peak at $2f_D \approx 62$ Hz. The spectrum also shows small peaks at $f_D - f_\alpha \approx 20$ Hz and $f_D + f_\alpha \approx 42$ Hz. Multiple subharmonics of $f_D/3$ are seen for $A_D = 11$. It should be noted that $2f_D/3 \approx f_D - f_\alpha \approx 20$ Hz while $4f_D/3 \approx f_D + f_\alpha \approx 42$ Hz, which implies that double resonances are possible between these peaks. At $A_D = 26$ there are strong peaks at fundamental and harmonic frequencies $2f_D$ and $3f_D$. The alpha peak is shifted from 10 Hz for higher amplitude and is seen at ≈ 13.7 Hz. The spectrum also shows peaks at $f_D - f_\alpha \approx 20$ Hz, $f_D + f_\alpha \approx 44.6$ Hz, and $f_D + f_\beta \approx 47.7$ Hz.

3.6 Scalings

Previous theoretical analysis has shown that simple scalings of the harmonic power can be expected when the peaks involved are narrow and dominate the adjacent spectrum, enabling the latter to be neglected in the calculations — e.g., causing a quartic scaling of second harmonic power with A_D (Robinson and Roy, 2015). The fact that the terms in Eqs (3.16) – (3.21) all involve integer powers of ϕ_D (and hence of A_D) thus motivates us to examine the scalings of power in narrow, dominant spectral peaks more generally, seeking power-law relationships of the form

$$P_{peak} \sim A_D^m, \tag{3.36}$$

where P_{peak} is the peak power and m is a scaling exponent, which should be an integer for sufficiently narrow and dominant peaks. Power-law relationships between power and drive amplitude enable different classes of nonlinear processes to be distinguished, which is not the case for power vs. frequency. For instance, the power at the fundamental should have $m = 2$, while the second harmonic peak is expected to have $m = 4$, based on Eq. (3.36). Similarly, the third harmonic peak, which arises through wave-wave interactions between fundamental and second-harmonic peaks, is expected to have $m = 6$. To test Eq. (3.36), we drive the system with the same external stimuli as used above, with a range of A_D in each case, and fit Eq. (3.36) to the resulting scalings in ranges where the peaks involved are narrow and dominant.

Stimuli with $f_D = 4$ Hz generate only integer harmonics as clear peaks, as seen in Fig. 3.4(a). Using the range $A_D = 1 - 15$, where the peaks are narrow and dominant, the powers at f_D, $2f_D$, and $3f_D$ are found to satisfy $m = 2.14 \pm 0.01$, $m = 3.76 \pm 0.07$, and $m = 5.68 \pm 0.07$, respectively; these are close to the expected integers 2, 4, and 6, but not to within the numerical error bars, most likely owing to lack of absolute sharpness and dominance of the peaks that were assumed in deriving the scaling in Eq. (3.36). Outside the range $A_D = 1 - 15$, power-law fits break down completely because the peaks are no longer sufficiently narrow and/or dominant.

At $f_D = 22$ Hz there are peaks at f_α, f_D, $f_D + f_\alpha$, $2f_D$, and $5f_D/2$, as seen in

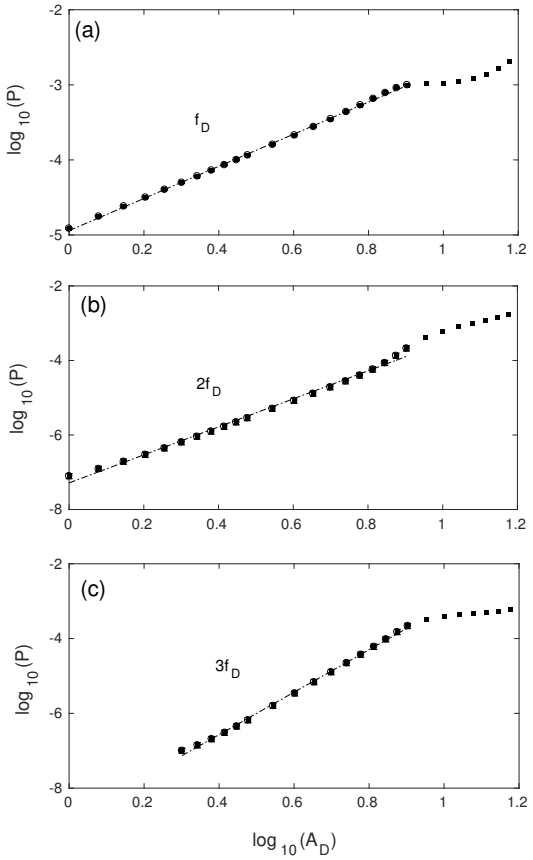

Figure 3.5: Peak powers versus the drive amplitude A_D for $f_D = 4$ Hz, using the parameters in Table 3.1. (a) Powers at f_D. (b) Powers at $2f_D$. (c) Powers at $3f_D$.

Fig. 3.4(b). For $A_D = 1 - 15$ the peaks at f_D and $2f_D$ have scaling exponents of 1.61 ± 0.06 and 3.54 ± 0.09, respectively, as shown in Fig. 3.6(a). Here the second harmonic peak arises through wave-wave interactions between 1/2 subharmonic and 3/2 fractional harmonic. Alpha peak powers have $m = 1.21 \pm 0.06$ for the limited range $3 \leq A_D \leq 9$, as shown in Fig. 3.6(b); this is not consistent with the expected value $m = 0$. The nonlinearities arise due to the resonance at $f_D/2 = f_D - f_\alpha = 3f_D/2 - f_D \approx 11$ Hz. Thus, multiple processes are consistent with the second term in (3.22) for phase correlations of ϕ_A and ϕ_D and expected to have $m = 1$. The peaks found at $3f_D/2 = f_D + f_\alpha \approx 33$ Hz and $5f_D/2 \approx 55$ Hz yield $m = 2.74 \pm 0.17$ and $m = 4.37 \pm 0.18$, as shown in Fig. 3.6(c), for $2.4 \leq A_D \leq 12$. These scaling exponents are close to the integers

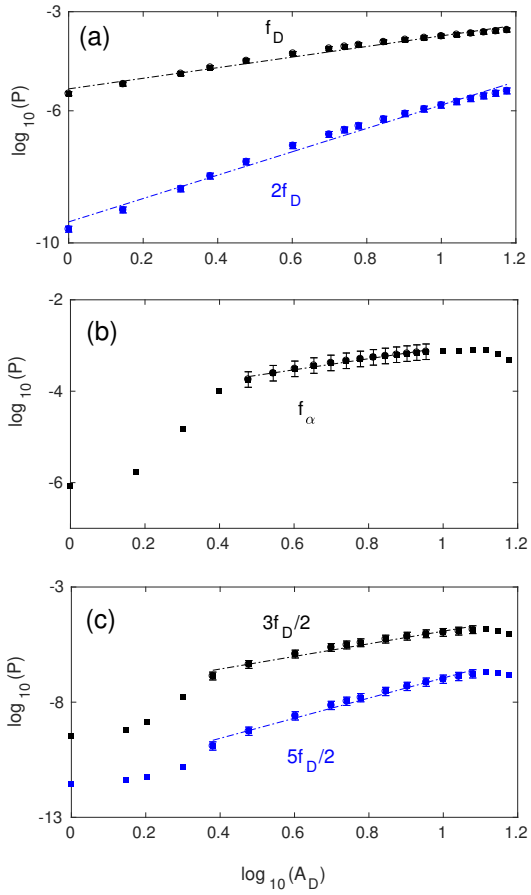

Figure 3.6: Peak powers versus the drive amplitude A_D for $f_D = 22$ Hz, using the parameters in Table 3.1. (a) Powers at f_D and $2f_D$. (b) Powers at f_α. (c) Powers at $3f_D/2$ and $5f_D/2$.

3 and 4, respectively, but not to within the numerical uncertainties, again likely because of incomplete dominance of the spectrum and the simultaneous contribution of multiple processes with different scalings.

For $f_D = 31$ Hz peaks at f_D, $2f_D$, f_α, $f_D/3$, $f \pm f_\alpha$, $2f_D/3$, and $4f_D/3$ are seen in Figs 3.2 and 3.3(c). The f_D and $2f_D$ peaks yield $m = 1.64 \pm 0.03$ and $m = 3.51 \pm 0.04$, respectively, for $A_D = 1 - 25$, as shown in Fig. 3.7(a). The second harmonic peak arises through wave-wave interactions between 2/3 and 4/3 fractional harmonics. For $A_D = 1 - 10$ the alpha peaks are sharp and dominant, as seen in Fig. 3.4 giving $m = 0.29 \pm 0.17$, as shown in Fig. 3.7(b),

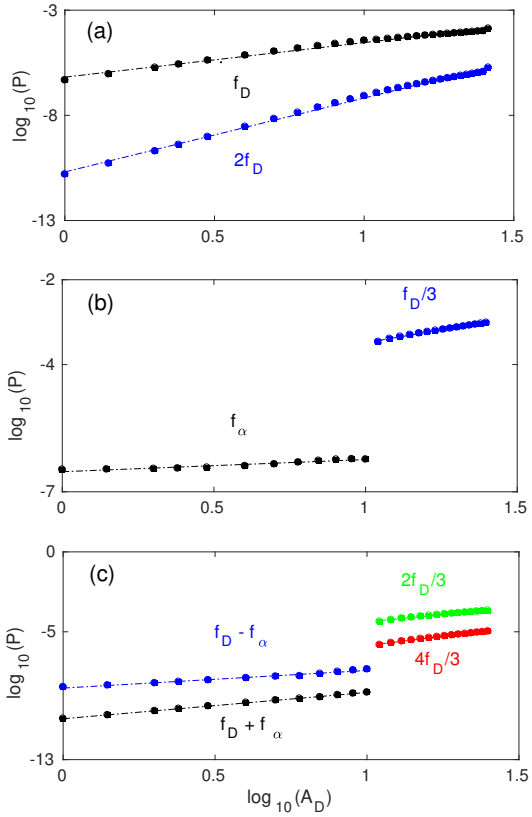

Figure 3.7: Peak powers versus the drive amplitude A_D for $f_D = 31$ Hz, using the parameters in Table 3.1. (a) Powers at f_D and $2f_D$. (b) Powers at f_α and $f_D/3$. (c) Powers at $f_D + f_\alpha$, $4f_D/3$, $f_D - f_\alpha$, $2f_D/3$, respectively.

broadly consistent with the expected value $m = 0$. For $A_D \geq 10$ a sudden break point occurs and the alpha peak is shifted from 11 Hz to near ≈ 10.3 Hz due to the double resonances of $f_\alpha \approx 11$ Hz and $f_D/3 \approx 10.22$ Hz as seen in Fig. 3.4(c). For $A_D = 11 - 25$ peaks are found at $f_D/3$, with $m = 1.20 \pm 0.03$ as seen in Fig. 3.7(b).

The drive with $f_D = 31$ Hz generates peaks at $f_D \pm f_\alpha$, $2f_D/3$, and $4f_D/3$, as seen in Fig. 3.7(c). We find the peaks at $f_D \pm f_\alpha$ for $A_D = 1 - 10$ give $m = 1.64 \pm 0.01$ and $m = 1.10 \pm 0.05$, respectively. For $A_D \leq 10$ peaks at sum and difference frequencies are strong and follow approximately power-law relationships. At $A_D \approx 11$ a sudden break point occurs in parallel with the sudden change in the spectral shape seen between the green and black curves in Fig. 3.4(c). This resonance arises due to the closeness of the frequencies

Table 3.2: Parameters observed from results where the first and second column presents the drive frequency and spectral peaks values. The third and fourth column shows the scaling exponent and the range of fit in spectral peaks from numerical results. The fifth column presents the expected scaling exponent from calculation.

f_D (Hz)	Peak	m	A_D range of fit	Theoretical m
4	f_D	2.14 ± 0.01	1−15	2
4	$2f_D$	3.76 ± 0.07	1−15	4
4	$3f_D$	5.68 ± 0.07	1−15	6
22	f_α	1.21 ± 0.06	3−9	0
22	f_D	1.61 ± 0.06	1−15	2
22	$2f_D$	3.54 ± 0.09	1−15	4
22	$3f_D/2$	2.74 ± 0.17	2.4−12	-
22	$5f_D/2$	4.37 ± 0.18	2.4−12	-
31	f_α	0.29 ± 0.17	1−10	0
31	f_D	1.64 ± 0.03	1−26	2
31	$2f_D$	3.51 ± 0.04	1−26	4
31	$f_D + f_\alpha$	1.64 ± 0.01	1–10	-
31	$f_D - f_\alpha$	1.10 ± 0.05	1−10	-
31	$f_D/3$	1.20 ± 0.03	11−25	-
31	$2f_D/3$	1.87 ± 0.05	11−25	-
31	$4f_D/3$	2.23 ± 0.05	11−25	-

$f_D + f_\alpha = 42$ Hz and $4f_D/3 = 41.3$ Hz and of the frequencies $f - f_\alpha = 20$ Hz and $2f_D/3 = 20.7$ Hz, respectively. The peaks at $2f_D/3$ and $4f_D/3$ for $A_D = 11 - 25$ yield $m = 1.87 \pm 0.05$ and $m = 2.23 \pm 0.05$ follow approximately power-law relations.

The overall results are summarized in Table 3.2. The scaling exponents of fundamental frequencies are close to the expected value predicted by the calculation of nonlinear power spectrum. In particular the relation follows power-laws in ranges where peaks are sharp and dominant and deviates where the peaks are broader. Multiple processes contribute at the same time which may affect integer value; e.g., the scaling exponents of second harmonic for drive frequencies 22 and 31 Hz are far from the expected theoretical value $m = 4$. This deviation is not unexpected because multiple wave-wave interactions with different scalings in general, contribute to the second harmonic, with $2f_D = f_D + f_D = f_D/2 + 3f_D/2 = f_\alpha + 3f_D/2$ relevant at $f_D = 22$ Hz, for example. The same complexity applies at $f_D = 31$ Hz, where $2f_D = f_D + f_D = 2f_D/3 + 4f_D/3$. Likewise, phase correlation of ϕ_A and ϕ_D can modify the exponents; for example, the alpha peak's scaling exponents are expected to be zero, but for $f_D = 22$ Hz this exponent is 1.21 ± 0.06 and multiple wave-wave processes also occur at the alpha frequency where $f_\alpha = f_D/2 = f_D - f_\alpha = 3f_D/2 - f_D$.

Prediction of the scaling exponents for subharmonics and fractional harmonics is beyond the scope of our present analysis, which does not include possible phase correlations between ϕ_A and ϕ_D in (3.22). However, we note that such correlations would result in terms with $m = 1$, 3 arising from that equation. Notably, for $f_D = 31$ Hz the scaling exponent at $3f_D/2$ is close to 3 and the scaling exponents at $f_D - f_\alpha$ and $f_D/3$ are close to 1.

3.7 Square wave drive

In this section we drive the system with periodic square wave plus background noise to generate SSVEP responses in the presence of normal brain activity. The square wave is given by

$$\phi_d(t) = A_D \ \mathrm{sgn}[\sin(2\pi f_D t)], \tag{3.37}$$

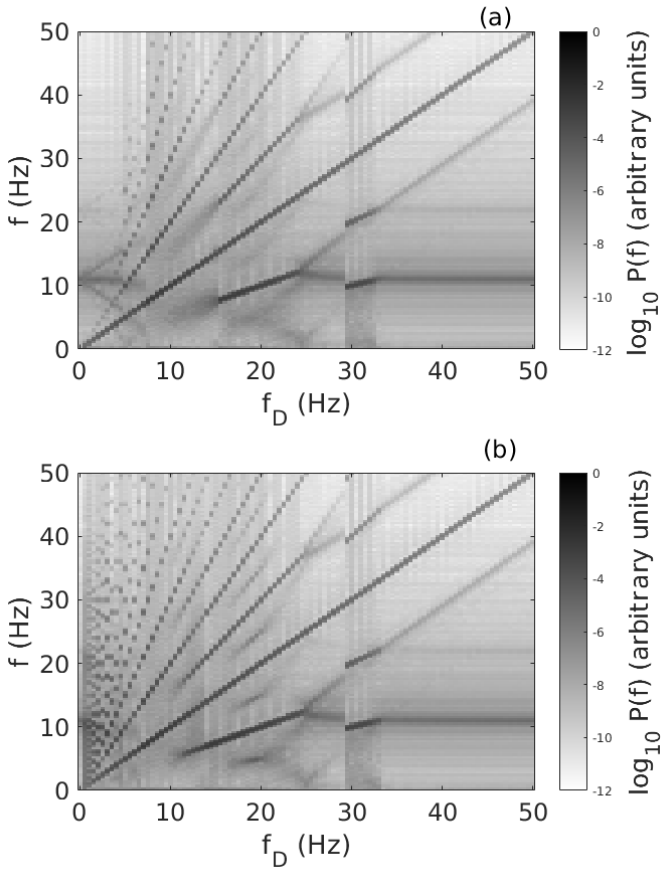

Figure 3.8: Spectral response for $f_D = 0 - 50$ Hz. The physiological parameters are adapted from (Roberts and Robinson, 2012). Darker shading denotes higher power. (a) For sine drive of amplitude $A_D = 2.8$. (b) For square drive of amplitude $A_D = 2.8$.

where sgn is the sign function and the square wave consists of a sum of sinusoids, such that the drive contains power at all odd multiples of f_D in the form

$$\phi_d(t) = \frac{4}{\pi} \sum_{n=1,3,5,..}^{\infty} \frac{1}{n} \sin(2\pi n f_D t). \tag{3.38}$$

Hence, system responses at even multiples are necessarily nonlinear, while those at odd harmonic frequencies contain both linear and nonlinear components.

3.7.1 Sinusoidal vs. square wave drive

In this subsection we compare the results for sine and square wave drive in more detail. Figures 3.8(a) and (b) show the model response spectrum vs. f_D for a sinusoidal and square drive given by Eqs (3.35) and (3.38), respectively. The same model parameters from Table 3.1 are used in Fig. 3.8(b) and $4/\pi$ is multiplied in Eq. (3.38) to normalize the amplitude of square wave. The key features of Figs 3.8(a) and (b) are:

(i) Key nonlinear features harmonics, subharmonics, entrainment, and sum and difference frequencies are observed in both cases. In Fig. 3.8(b), higher harmonics are present in the square drive whereas the sine drive generates 5:1 harmonics, in good agreement with previous work (Herrmann, 2001, Roberts and Robinson, 2012).

(ii) For square drive, the suppression of the background alpha activity is seen at $f_\alpha \approx 11$ Hz for $f_D \lessapprox 11.5$ Hz whereas in sine drive it is seen in the range of 4 Hz $\lessapprox f_D \lessapprox 15$ Hz. For square drive, entrainment of alpha activity is observed by the 1/2 subharmonic for 11.5 Hz $\lessapprox f_D \lessapprox 25$ Hz, and by the 1/3 subharmonic for 29.5 Hz $\lessapprox f_D \lessapprox 33$ Hz. For sine drive, entrainment of alpha activity is observed by the 1/2 subharmonic for 15 Hz $\lessapprox f_D \lessapprox 25$ Hz, and by the 1/3 subharmonic for 29 Hz $\lessapprox f_D \lessapprox 32.5$ Hz.

(iii) For square drive, $f_\pm = |f_D \pm f_\alpha|$ are seen at $f_D \gtrapprox 25$ Hz whereas for sine drive, $f_\pm = |f_D \pm f_\alpha|$ are seen at $f_D \lessapprox 5$ Hz ($f_\alpha \pm f_D$) and $f_D \gtrapprox 25$ Hz ($f_D \pm f_\alpha$). These interactions are equivalent to wave coalescence and decay (i.e., wave mixing) in other branches of nonlinear wave physics and have been observed in SSVEP studies using two distinct drive frequencies (Regan, 1989).

(iv) Strong responses at $f_D/3$, $2f_D/3$, and $4f_D/3$ are seen for 29 Hz $\lessapprox$

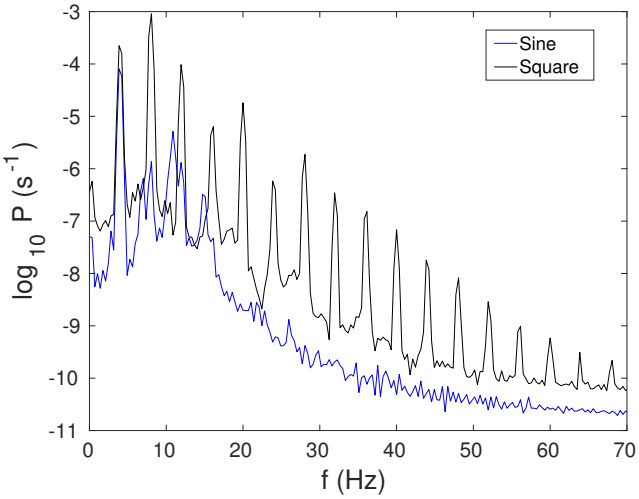

Figure 3.9: Power spectra of model SSVEPs for sine and square drive of amplitude $A_D = 2.8$ at $f_D = 4$ Hz, using the parameters in Table 3.1.

$f_D \lesssim 32.5$ Hz for both cases. For square drive, additional fractional harmonics are found at $f_D = 1/4, 3/4, 5/4, 7/4$ in the spectra which are not present in Fig. 3.8(a).

Figure 3.9 shows the power spectra for square and sine drives, respectively, at $f_D = 4$ Hz. We see that the power spectrum of the response exhibits many more peaks for square drive than for the sinusoidal case. Since the square wave input signal contains only odd harmonics, the even harmonics in the output must be generated nonlinearly, whereas power at the odd harmonic frequencies can contain both linear and nonlinear components.

3.7.2 Wave coalescence and decay

In order to see how much of the spectrum seen in Fig. 3.8(b) is nonlinear, and how much is simply due to the presence of harmonics of f_D in the square-wave drive, we subtract the spectrum due to a sine wave drive from that of the square-wave drive in Fig. 3.10(a), setting the amplitude of the sine drive to that of the fundamental term in Eq. (3.38). Strong third and fifth harmonics are seen and weak higher harmonics are also visible. Subharmonics and fractional harmonics are not present here as seen in Fig. 3.8(b). Therefore, the fundamental frequency plays a key role in generating subharmonics and fractional harmonics.

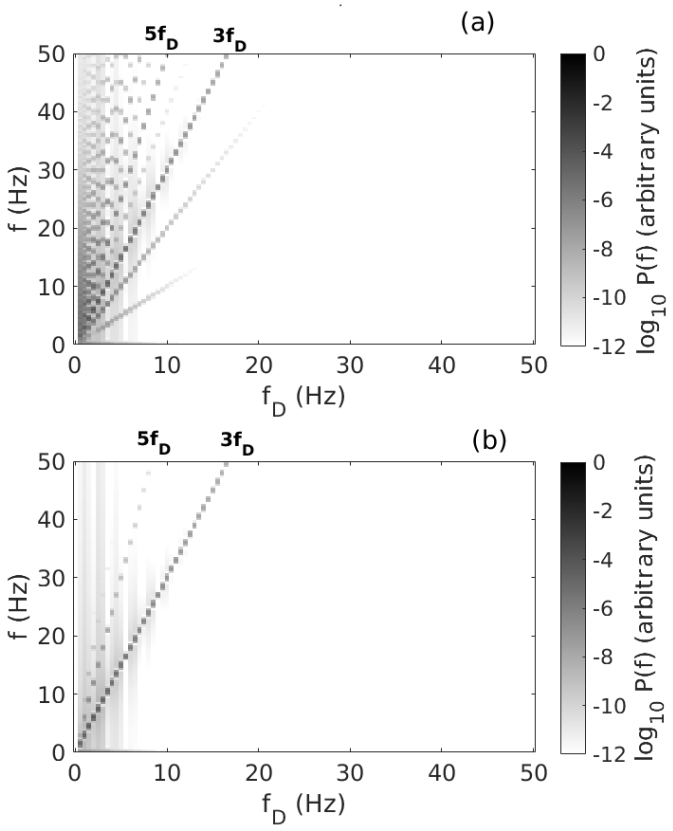

Figure 3.10: Spectral response for $f_D = 0 - 50$ Hz. The physiological parameters are adapted from Roberts and Robinson (2012). Darker shading denotes higher power. (a) Subtracting the spectrum due to a sinusoid from that due to a square wave with the same frequency. (b) Third harmonic response alone.

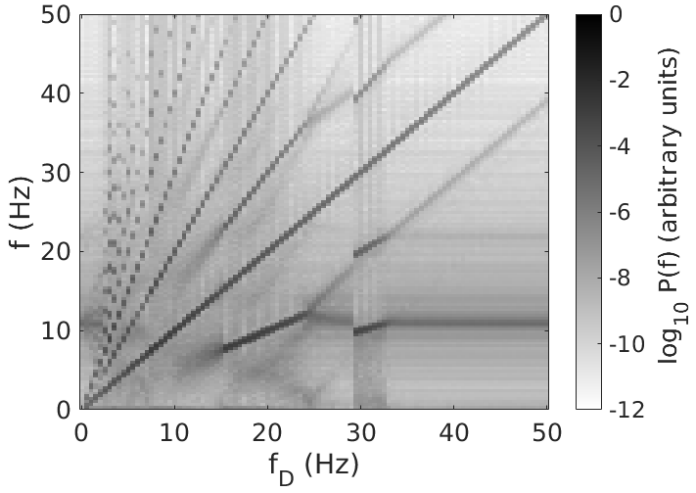

Figure 3.11: Spectral response of fundamental and third harmonic of sine wave for $f_D = 0 - 50$ Hz. The physiological parameters are adapted from (Roberts and Robinson, 2012). Darker shading denotes higher power.

Figure 3.10(b) shows the response for third harmonic alone for $A_D = 2.8$. A strong third harmonic is seen indicates that the system is driven by stimulus at the stimulation frequency. In addition, a fifth harmonic is marginally detected. The other nonlinear features including subharmonics and fractional harmonics are not seen here.

In order to see the linear and nonlinear effects in presence of f_D and $3f_D$ in square-wave drive more clearly, we drive the system with fundamental and third harmonic of sine wave of $A_D = 2.8$ in Fig. 3.11. The nonlinear features harmonics, subharmonics, entrainment, and $|f_D \pm f_\alpha|$ are clearly observed as seen in Fig. 3.8(b). We see that removing higher harmonics from the square drive reduces power at high frequencies. The fractional harmonics at $f_D = 1/4, 3/4, 5/4, 7/4$ in the spectra are not present here, while the case seen in Fig. 3.8(b).

3.8 Nonlinear interactions of two sinusoidal drives

In this section, we drive the system by dual sine drives of narrow bandwidth, also reducing the value of background noise to attenuate the background spectrum and its interactions with drives. Together, these modifications make the

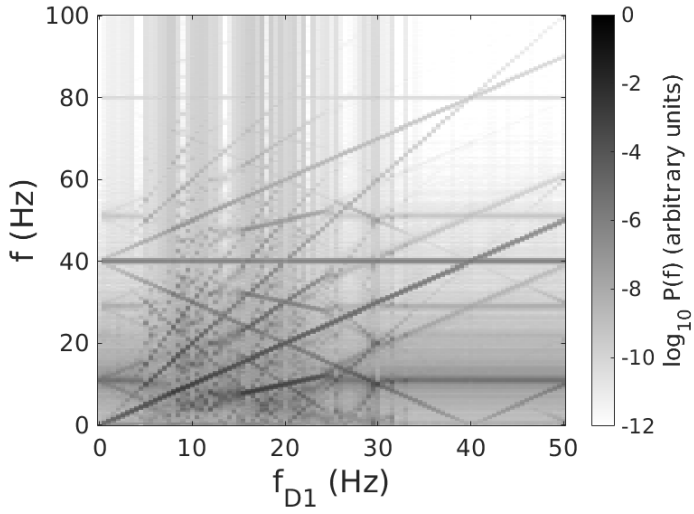

Figure 3.12: Spectral response of two sine drives of amplitude $A_{D1} = A_{D2} = 2.8$ for $f_{D1} = 0 - 50$ Hz, $f_{D2} = 40$ Hz, and $\phi_n^{noise} = 18$ s^{-1}. The other physiological parameters are adapted from (Roberts and Robinson, 2012). Darker shading denotes higher power.

drives more narrowband and dominant and thus enable us to see the nonlinear interactions and their scalings more clearly. Aside from these changes, we use the model parameters from Table 3.1 and analyze the nonlinear interactions in Figs 3.12−3.18.

Figure 3.12 shows the spectral response for two sine drives with $A_{D1} = A_{D2} = 2.8$, $f_{D1} = 0 - 50$ Hz and $f_{D2} = 40$ Hz, and $\phi_n^{noise} = 18$ s^{-1}. Strong responses at f_{D1} and f_{D2} are seen in Fig. 3.12. The clearest nonlinear effect is the generation of harmonics $(2f_{D1}, 3f_{D1}, 4f_{D1}, 2f_{D2})$, subharmonics, and fractional harmonics $(f_{D1}/2, 3f_{D1}/2, 5f_{D1}/2)$. Entrainment to f_{D1} is also exhibited by suppression of background activity $f_\alpha \approx 11$ Hz for 4.5 Hz $\lesssim f_{D1} \lesssim$ 15.5 Hz. Figure 3.12 displays complex nonlinear interactions and to see the clear nonlinear features we turn down the value of background noise $\phi_n^{noise} = 5$ s^{-1} in Fig. 3.13.

The clear nonlinear effect in Fig. 3.13 is the generation of sum and difference of two drive frequencies and its harmonics by nonlinear processes. To briefly explain how frequency mixing occurs in a general setting, consider a signal $y(t) = \sin(\omega_1 t) + \sin(\omega_2 t)$ comprising two sinusoids with frequencies ω_1 and ω_2. If this signal is passed through a quadratic nonlinearity, the resulting signal is

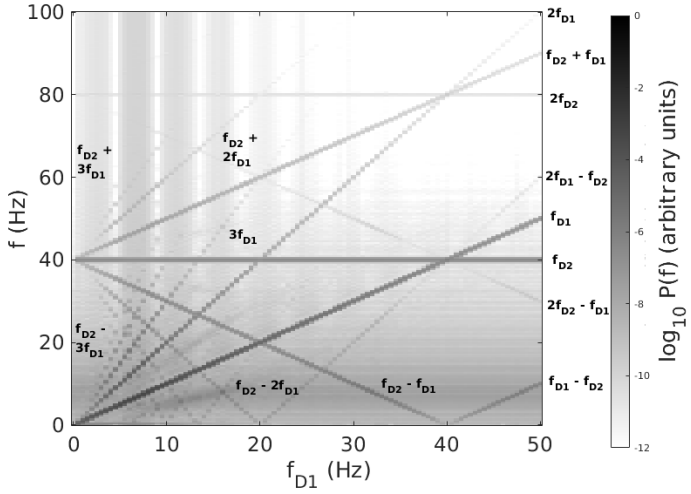

Figure 3.13: Spectral response of two sine drives of $A_{D1} = A_{D2} = 2.8$ for $f_{D1} = 0 - 50$ Hz, $f_{D2} = 40$ Hz, and $\phi_n^{noise} = 5\ \mathrm{s}^{-1}$. The physiological parameters are adapted from (Roberts and Robinson, 2012). Darker shading denotes higher power.

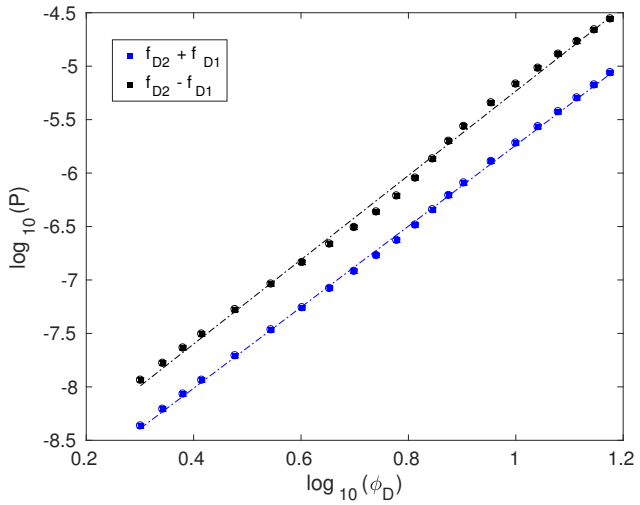

Figure 3.14: Peak power of $|f_{D2} \pm f_{D1}|$ versus the drive amplitude A_D for $f_{D1} = 5$ Hz and $f_{D2} = 40$ Hz, using the parameters in Table 3.1. The black line shows the power at $f_{D2} - f_{D1}$ and the blue line shows the power at $f_{D2} + f_{D1}$.

$y^2(t) = 1 - \cos(2\omega_1 t)/2 - \cos(2\omega_2 t)/2 + \cos[(\omega_1 - \omega_2)t] - \cos[(\omega_1 + \omega_2)t]$ and thus contains second harmonics $2\omega_1$ and $2\omega_2$, $\omega_1 + \omega_2$, and $\omega_1 - \omega_2$, respectively.

As an example of the clear scalings obtained using dual sine drives, Fig. 3.14

shows the scalings of the power at $|f_{D2} \pm f_{D1}|$ for $f_{D1} = 5$ Hz and $f_{D2} = 40$ Hz. The peak at $f_{D2} + f_{D1}$ arises through wave-wave interactions between f_{D1} and f_{D2}, and is expected to have $m = 4$. The peak at $f_{D2} - f_{D1}$ also arises due to wave-wave coalescence of f_{D1} and $-f_{D2}$, and is expected to have $m = 4$. For $A_D = 2{-}15$, the peaks at $f_{D2} + f_{D1} = 45$ Hz and $f_{D2} - f_{D1} = 35$ Hz yield $m = 3.79 \pm 0.02$ and $m = 3.94 \pm 0.03$, respectively; these are very close to the expected integer because of the very sharp and dominant peaks involved.

We perform a similar analysis to see the nonlinear interactions for $f_{D1} = 0 - 50$ Hz and $f_{D2} = 10$ Hz as a second example in Figs 3.15−3.18. Figure 3.15 shows the spectral response for two drives with $A_{D1} = 2.8$ and $A_{D2} = 0.5$. Strong responses at fundamental (f_{D1}, f_{D2}), harmonics ($2f_{D1}$, $3f_{D1}$, $4f_{D1}$, $2f_{D2}$), $|f_{D1} \pm f_{D2}|$, and $f_{D2} - f_{D1}$ are seen. Weak responses at $|f_{D1} \pm 2f_{D2}|$ and $f_{D2} - 2f_{D1}$ are also observed. In order to see these weak responses more clearly we increase the amplitude $A_{D2} = 1.5$ in Fig. 3.16.

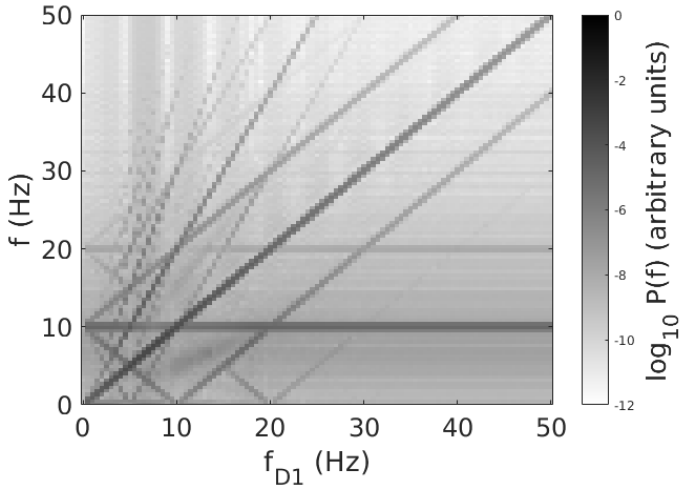

Figure 3.15: Spectral response of two sine drives of $A_{D1} = 2.8$ and $A_{D2} = 0.5$ for $f_{D1} = 0 - 50$ Hz and $f_{D2} = 10$ Hz. The physiological parameters are adapted from (Roberts and Robinson, 2012). Darker shading denotes higher power.

Figure 3.16 generate strong nonlinear responses at $|f_{D1} \pm f_{D2}|$, $|f_{D1} \pm 2f_{D2}|$, $|f_{D1} \pm 3f_{D2}|$, $f_{D2} - f_{D1}$, $f_{D2} - 2f_{D1}$, $2f_{D2} - f_{D1}$, and $3f_{D2} - f_{D1}$, which arises due to wave-wave coalescence and decay. At $f_{D1} = 10$ Hz spectral responses are seen at numerous frequencies which are all multiples of 5 Hz. We plot the power spectrum for $f_{D1} = f_{D2} = 10$ Hz in Fig. 3.17 which shows strong

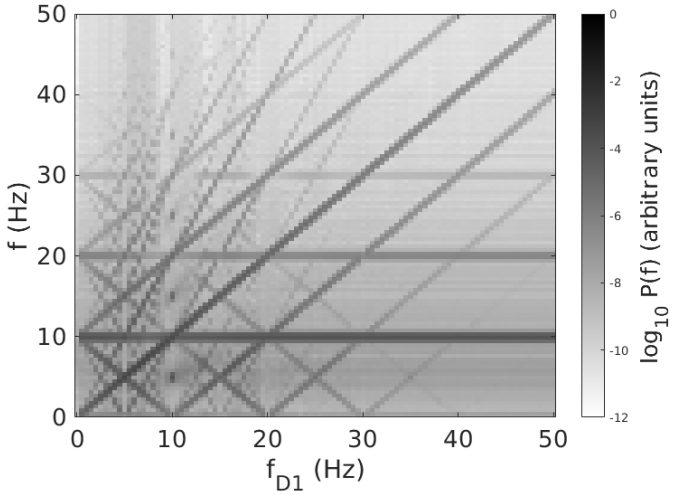

Figure 3.16: Spectral response of two sine drives for $f_{D1} = 0-50$ Hz, $f_{D2} = 10$ Hz, $A_{D1} = 2.8$, and $A_{D2} = 1.5$. The physiological parameters are adapted from (Roberts and Robinson, 2012). Darker shading denotes higher power.

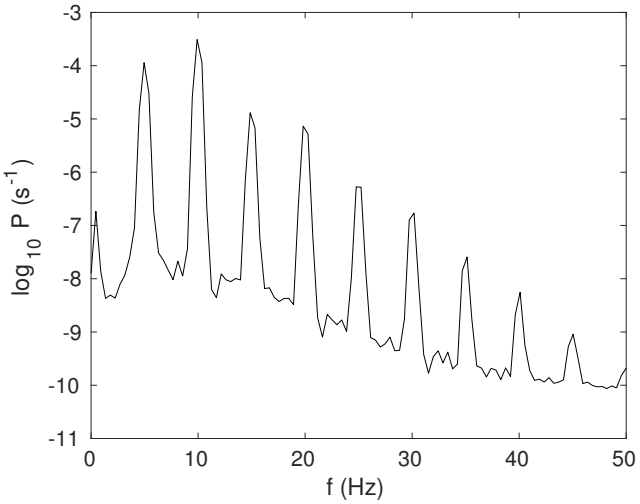

Figure 3.17: Power spectra of model SSVEPs for $f_{D1} = f_{D2} = 10$ Hz and $A_{D2} = 1.5$, using the parameters in Table 3.1.

peaks at 5 Hz and at all multiples of 5 Hz. Figure 3.18 shows the scalings of the power at $|f_{D2} \pm f_{D1}|$ for $f_{D1} = 5$ Hz and $f_{D2} = 10$ Hz. For $A_D = 2$ - 15, peaks at $f_{D2} + f_{D1} = 15$ Hz and $f_{D2} - f_{D1} = 5$ Hz yield $m = 2 \pm 0.05$ and $m = 1.23 \pm 0.03$, respectively. The peak at $f_{D2} + f_{D1}$ arises through wave-wave interactions between f_{D1} and f_{D2} where $f_{D2} = 10$ Hz which is the linear alpha

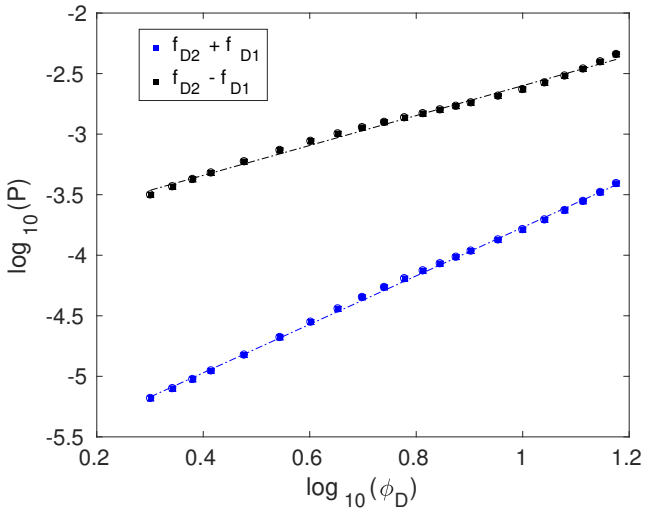

Figure 3.18: Peak power of $|f_{D2} \pm f_{D1}|$ versus the drive amplitude A_D for $f_{D1} = 5$ Hz and $f_{D2} = 10$ Hz, using the parameters in Table 3.1. The black line shows the power at $f_{D2} - f_{D1}$ and the blue line shows the power at $f_{D2} + f_{D1}$.

frequency. The peak at $f_{D2} - f_{D1}$ also arises due to wave-wave coalescence of f_{D1} and $-f_{D2}$.

3.9 Summary and discussion

We have studied nonlinear wave-wave interactions in large scale brain activity using a physiologically based corticothalamic neural field model. We verified key earlier results from (Roberts and Robinson, 2012) and more recent theoretical analysis (Ferdousi et al., 2019, Robinson and Roy, 2015), and derived new predictions here by employing sinusoidal and square-wave stimulation into the corticothalamic model. Our results demonstrated nonlinear key features including harmonics, subharmonics, fractional harmonics, and sum and difference frequencies. The nonlinear power spectrum was calculated numerically to investigate spectral peaks and their scalings. The main results are:

(i) The linear power spectrum was convolved with itself and other factors to calculate the nonlinear power spectrum for the driven dynamics of this model via perturbation expansion. Nonlinear analysis predicts an approximately quadratic relationship of the power in the fundamental peak to the amplitude of the

periodic stimuli. The second and third harmonic peaks follow the relation in the form $P \propto \phi_D^4$ and $P \propto \phi_D^6$ where the peaks are narrow and dominant.

(ii) Numerical analysis of the power spectrum found multiple harmonics ($2f_D$, $3f_D$, $4f_D$, and $5f_D$) and fractional harmonics ($f_D/3$, $f_D/2$, $2f_D/3$, $4f_D/3$, $3f_D/2$, and $5f_D/2$) in the responses to a periodic sinusoidal stimuli, of which only the 1/2, 3/2, and 5/2 fractional harmonics were visible in a previous study (Roberts and Robinson, 2012). The background activity of the alpha rhythm was also suppressed due to entrainment to the drive frequency for 15 Hz $\lesssim f_D \lesssim$ 25 Hz. Other observed key components of nonlinear interactions in the brain are sum and difference frequencies $|f_D \pm f_\alpha|$ at high f_D and $|f_\alpha \pm f_D|$ at low f_D. This numerical analysis confirmed earlier results (Roberts and Robinson, 2012) using the recently published NFTsim software (Sanz-Leon et al., 2018).

(iii) The scaling properties corresponding to strong peaks were investigated which verified the analytically derived predictions and identified several new wave-wave interactions. We found that the power in the peaks follows approximately power-law relationships to the amplitude of the stimuli, albeit only in ranges where the peaks are narrow and dominant. The scaling of alpha, fundamental, second, and third harmonic peaks have values near 0, 2, 4, and 6, respectively, for individual types of wave-wave interactions and dominant narrow peaks. However, multiple wave-wave interactions and/or phase correlations can occur at some frequencies, resulting in noninteger or odd-integer exponents. These exponents can be directly compared with clinical data on response strength vs. drive amplitude to test them and infer the nonlinear interactions that underlie the experimental observations.

(iv) Numerical analysis of square wave exhibited more complex nonlinear interactions than for the sinusoidal case which motivated us to simplify the case. Subtraction of sine wave from square wave with the amplitude of sine drive presented clear nonlinear interactions and removed the complicating effects of the background spectrum.

(v) Two sine drives were employed and turned down the value of background noise in SSVEPs to study spectral features and scaling. This analysis presented clear nonlinear features including harmonics, fractional harmonics, sum and difference of two drive frequencies due to wave-wave coalescence and decay and enabled quantitative analysis in terms of underlying physiology. The

scaling of peaks at $|f_{D2} \pm f_{D1}|$ verified the analytically derived predictions. Our analysis provided new verifications of the model, and of neural field theory more generally, complementary to recent studies. A recent study of two sinusoids of slightly different high frequencies (e.g. 2000 and 2010 Hz) exhibited temporal interference at the beat frequencies in deep regions of brain (Cao and Grover, 2018, Grossman et al., 2017). Here we focused on two sinusoids of low frequencies, but the same model and analysis should be applicable to high frequencies with appropriate parameters.

Overall, this study has illustrated the rich variety of interactions of nonlinear SSVEPs that can be tested in future experiments. Our model reproduces many features of observed EEG responses to periodic visual stimuli and yields more nonlinear features than previous studies (Roberts and Robinson, 2012).

Chapter 4

Concluding remarks and future directions

The main focus of this thesis has been on investigating the nonlinear dynamics that underlie wave-wave process such as harmonic and subharmonic generation, period doubling, wave-wave coupling, entrainment, and generation of sum and difference frequencies due to wave-wave coalescence and decay. Neural field theory of the corticothalamic system (Robinson et al., 2002, 2004, 1997, 1998, Robinson and Roy, 2015) is used to analyze nonlinear responses in Chapters 2−3. Some key results and possible future research directions are outlined in this chapter.

4.1 Summary

In Chapter 2 we explored the nonlinear dynamics in normal sleep and wake states using corticothalamic neural field theory (Abeysuriya et al., 2014a, Robinson et al., 2002, 2004, Robinson and Roy, 2015). Nonlinearity arises in many brain states such as sleep spindles (Freyer et al., 2009, Stam et al., 1999). We extended previous work (Abeysuriya et al., 2014a, Robinson and Roy, 2015) and relaxed some previous approximations to calculate the nonlinear contributions in the strong spectral peaks. The linear power spectrum was calculated analytically via the transfer function and then convolved with itself and other factors to calculate the nonlinear power spectrum analytically via a recent perturbation

expansion. Our results showed that the experimentally observed sleep spindle harmonic peak is nonlinear and the strongest nonlinearities were found in the thalamic relay nuclei, thus validating the prior prediction in this brain state (Abeysuriya et al., 2014a). The zero-frequency peak due to wave decay and a very low frequency wave were also found in the nonlinear spectrum.

Quantitative comparison of corticothalamic theory predictions with experiment implies that alpha and beta peaks are primarily linear, with the beta peak being primarily a linear harmonic generated in the same corticothalamic delay loop. But our analysis found that both alpha and beta peaks have significant nonlinear contributions in the nonlinear spectrum. The nonlinear terms can contribute up to about 50% of the power of both peaks. Unlike the sleep case, nonlinear contributions were not dominated by any one neural population. Nonlinearities in alpha and beta peaks have long been debated (Freyer et al., 2009, Stam et al., 1999), and it is important to know to what extent nonlinear processes play a role in their generation.

In Chapter 3 a similar model was used to study nonlinear wave-wave interactions in large scale brain activity by periodic stimuli. Periodic stimuli are widely used to probe sensory processing including the frequency and wave-number structure of the sensor-brain transfer function, and changes connected with attention, cognition, and disorders (Nunez and Cutillo, 1995, Regan, 1989), but the underlying mechanisms of the brain's responses are still poorly understood. The nonlinear power spectrum for a driven system was calculated analytically. The theory predicted an approximately quadratic relationship of the power in the fundamental peak to the amplitude of the periodic stimuli. Periodic sinusoidal and square drive have been used to generate SSVEP responses and the stimulus-driven nonlinear corticothalamic dynamic interactions were studied. The numerical analysis of scaling properties of the strong peaks verified the analytically derived predictions and identified several new wave-wave interactions. To our knowledge, this is the first study of scaling properties in nonlinear SSVEP dynamics. The observed nonlinear features including harmonics, subharmonics, entrainment, and frequency mixing agreed with experimental results, where available (Herrmann, 2001). Further, to see the nonlinear interactions more clearly, we (i) turned down the value of background noise to remove its interactions with drives; (ii) evoked dual sine drives and explored effects of a

second drive in SSVEPs. This revealed many features more clearly, including harmonics of the second drive, the sum and difference of two drive frequencies, and harmonics generated by nonlinear processes.

Overall, this analysis unifies linear and nonlinear dynamics with nonlinear SSVEPs in large scale brain activity and provides model predictions which are verified numerically. Moreover, this work opens new insights by predicting a rich variety of nonlinear dynamics that should be experimentally verifiable in human subjects.

4.2 Future directions

Nonlinear effects are commonly observed in abnormal brain activity, but observing nonlinearity in normal brain states is more challenging. The model used in Chapter 2 reveals nonlinear effects in normal brain states and focuses on nonlinearities only at strong and dominant peaks. The numerical analysis of the nonlinear power spectrum has mostly considered the $\mathbf{k} = 0$ mode, which is often dominant at spectral peaks. Nonlinear effects for non zero $\mathbf{k}$ (spatially varying) could be studied in future using the present theory. We have found significant nonlinear contributions to alpha and beta peaks but further theoretical and numerical analysis of the nonlinear spectrum need to be done to fully explore the precise origins of these effects in the wake state. The quantitative analysis in this thesis also lays the foundations for treatment of a large variety of other wave-wave interactions in normal and driven brain activity.

The model used in Chapter 3 reproduces and extends previous results on SSVEPs on the corticothalamic system and is open for further extension to include different drives rather than sine or square to analyze nonlinear effects. For example, the square-wave-driven SSVEP experiments of Herrmann (2001) could be modified to use sine drives in future to observe nonlinearities more clearly and the scalings of responses vs. drive strength could be explored in order to identify the physical nonlinear processes active in experiment.

The use of two sinusoidal drives as in Chapter 3 opens up a new research direction for the study of deep brain stimulation. For example, recent studies observed that in deep regions of the brain where two sinusoids of slightly different

high frequencies (e.g., 2000 and 2010 Hz) have similar amplitudes, neurons fire at the resulting beat frequency — a process called temporal interference stimulation (Cao and Grover, 2018, Grossman et al., 2017). Future work using the present theory could analyze temporal interference stimulation in terms of nonlinear wave-wave and wave-neuron processes to better understand and optimize it for use in clinical research and treatment (e.g., for Parkinson's disease).

On the theoretical front, the present model still needs to be extended to predict scalings of subharmonics and fractional harmonics and resulting predictions will need to be further analyzed. Further numerical analysis of cases with multiple simultaneous nonlinear resonances is also called for to better understand their dynamics.

Bibliography

Abeysuriya RG. Physiologically-based Brain State Modeling. Ph.D. thesis, University of Sydney, 2014.

Abeysuriya RG, Rennie CJ, Robinson PA. Prediction and verification of nonlinear sleep spindle harmonic oscillations. J Theor Biol 2014a; 344:70–77.

Abeysuriya RG, Rennie CJ, Robinson PA. Physiologically based arousal state estimation and dynamics. J Neurosci Meth 2015; 253:55–69.

Abeysuriya RG, Rennie CJ, Robinson PA, Kim JW. Experimental observation of a theoretically predicted nonlinear sleep spindle harmonic in human EEG. Clin Neurophysiol 2014b; 125:2016–2023.

Adrian ED, Matthews BHC. The Berger rhythm: Potential changes from the occipital lobes in man. Brain 1934; 57:355–385.

Afifi AK, Bergman RA. Functional Neuroanatomy: Text and Atlas. New York: McGraw-Hill, 2nd ed., 2005.

Allen NJ, Barres BA. Glia - more than just brain glue. Nature 2009; 457:675–677.

Amari S. Dynamics of pattern formation in lateral-inhibition type neural fields. Biol Cybern 1977; 27:77–87.

Barres BA. The mystery and magic of glia: a perspective on their roles in health and disease. Neuron 2008; 60:430–440.

Basar E. EEG-Brain Dynamics: Relation between EEG and brain evoked potentials. New York: Elsevier North-Holland, 1980.

Bear MF, Connors BW, Paradiso MA. Neuroscience: Exploring the brain. Philadelphia: Lippincott Williams and Wilkins, 2nd ed., 2001.

Berger H. Über das Elektrenkephalogramm des Menschen. Arch Psychiatr Nervenkr 1929; 87:527–570.

Beurle RL. Properties of a mass of cells capable of regenerating pulses. Phil Trans Roy Soc B 1956; 240:55–94.

Boyd RW. Nonlinear Optics. Boston: Academic, 2nd ed., 1992.

Braitenberg V, Schüz A. Cortex: Statistics and Geometry of Neuronal Connectivity. Berlin: Springer, 2nd ed., 1998.

Breakspear M, Roberts JA, Terry JR, Rodrigues S, Mahant N, Robinson PA. A unifying explanation of primary generalized seizures through nonlinear brain modeling and bifurcation analysis. Cereb Cortex 2006; 16:1296–1313.

Bressloff PC, Cowan JD. The visual cortex as a crystal. Physica D 2002; 173:226–258.

Buice MA, Cowan JD. Field-theoretic approach to fluctuation effects in neural networks. Phys Rev E 2007; 75:051919.

Buzsáki G, Anastassiou CA, Koch C. The origin of extracellular fields and currents–EEG, ECoG, LFP and spikes. Nat Rev Neurosci 2012; 13:407–420.

Campbell NA, Reece JB, Meyers BB. Biology. Pearson Education Australia, Frenchs Forest, 7th ed., 2006.

Cao J, Grover P. Do single neuron models exhibit temporal interference stimulation? IEEE Biomed Circuits Syst Conf (BioCAS) 2018; to appear.

Caton R. Electric currents of the brain. J Nerv Ment Dis 1875; 2:610.

Contreras D, Destexhe A, Sejnowski TJ, Steriade M. Spatiotemporal patterns of spindle oscillations in cortex and thalamus. J Neurosci 1997; 17:1179–1196.

Coombes S. Waves, bumps, and patterns in neural field theories. Biol Cybern 2005; 93:91–108.

David O, Friston KJ. A neural mass model for MEG/EEG:: coupling and neuronal dynamics. NeuroImage 2003; 20:1743–1755.

David O, Harrison L, Friston KJ. Modelling event-related responses in the brain. Neuroimage 2005; 25:756–770.

Dayan P, Abbott LF. Theoretical Neuroscience: Computational and Mathematical Modeling of Neural Systems. Cambridge: MIT Press, 2001.

Deco G, Jirsa VK, Robinson PA, Breakspear M, Friston K. The dynamic brain: from spiking neurons to neural masses and cortical fields. PLoS Comput Biol 2008; 4:e1000092.

Deeba F, Sanz-Leon P, Robinson PA. Dependence of absence seizure dynamics on physiological parameter evolution. J Theor Biol 2018; 454:11–21.

Ferdousi M, Babaie Janvier T, Robinson PA. Nonlinear harmonic generation in the corticothalamic system. J Theor Biol 2019; 460:184–194.

Freeman J, Holmes P. Nonlinear Oscillations, Dynamical Systems, and Bifurcations of Vector Fields. New York: Springer, 7th ed., 2002.

Freeman WJ. Mass Action in the Nervous System. New York: Academic Press, 1975.

Freyer F, Aquino K, Robinson PA, Ritter P, Breakspear M. Bistability and non-Gaussian fluctuations in spontaneous cortical activity. J Neurosci 2009; 29:8512–8524.

Freyer F, Roberts JA, Becker R, Robinson PA, Ritter P, Breakspear M. Biophysical mechanisms of multistability in resting-state cortical rhythms. J Neurosci 2011; 31:6353–6361.

Friston KJ, Holmes AP, Worsley KJ, Poline JP, Frith CD, Frackowiak RSJ. Statistical parametric maps in functional imaging: a general linear approach. Hum Brain Mapp 1995; 2:189–210.

Griffith JS. A field theory of neural nets: I: Derivation of field equations. Bull Math Biophys 1963; 25:111–120.

Griffith JS. A field theory of neural nets: II: Derivation of field equations. Bull Math Biophys 1965; 27:187–195.

Grossman N, Bono D, Dedic N, Kodandaramaiah SB, Rudenko A, Suk H, Cassara AM, Neufeld E, Kuster N, Tsai L, Pascual-Leone A, Boyden ES. Noninvasive deep brain stimulation via temporally interfering electric fields. Cell 2017; 169:1029–1041.

Haines DE. Fundamental Neuroscience for Basic and Clinical Applications. Philadelphia: Churchill Livingstone Elsevier, 4th ed., 2006.

Harrison L, Penny WD, Friston K. Multivariate autoregressive modeling of fMRI time series. NeuroImage 2003; 19:1477–1491.

Herrmann CS. Human EEG responses to 1-100 Hz flicker: resonance phenomena in visual cortex and their potential correlation to cognitive phenomena. Exp Brain Res 2001; 137:346–353.

Hodgkin AL, Huxley AF. A quantitative description of membrane current and its application to conduction and excitation in nerve. J Physiol 1952; 117:500–544.

Jansen BH, Rit VG. Electroencephalogram and visual evoked potential generation in a mathematical model of coupled cortical columns. Biol Cybern 1995; 73:357–366.

Jansen BH, Zouridakis G, Brandt ME. A neurophysiologically-based mathematical model of flash visual evoked potentials. Biol Cybern 1993; 68:275–283.

Jenkins S, Brown R, Rutterford N. Comparing thermographic EEG and subjective measures of affective experience during simulated product interactions. Int J Des 2009; 3:53–65.

Jirsa VK, Haken H. Field theory of electromagnetic brain activity. Phys Rev Lett 1996; 77:960–963.

Jirsa VK, Haken H. A derivation of a macroscopic field theory of the brain from the quasimicroscopic neural dynamics. Physica D 1997; 99:503–526.

Kandel ER, Schwartz JH, Jessell TM. Principles of Neural Science. New York: McGraw-Hill, 4th ed., 2000.

Kim JW, Robinson PA. Compact dynamical model of brain activity. Phys Rev E 2007; 75:031907.

Koch C. Biophysics of Computation: Information Processing in Single Neurons. New York: Oxford, 1999.

Liley DTJ, Wright JJ. Intracortical connectivity of pyramidal and stellate cells: estimates of synaptic densities and coupling symmetry. Netw: Comput Neural Syst 1994; 5:175–189.

Lopes da Silva FH, Hoeks A, Smits H, Zetterberg LH. Model of brain rhythmic activity. The alpha-rhythm of the thalamus. Kybernetik 1974; 15:27–37.

Macdonell RAL, Donnan GA, Bladin PF. A comparison of somatosensory evoked and motor evoked potentials in stroke. Ann Neurol 1989; 25:68–73.

Mendel JM. Tutorial on higher-order statistics (spectra) in signal processing and system theory: theoretical results and some applications. Proc IEEE 1991; 79:278–305.

Mignard M, Malpeli JG. Paths of information flow through visual cortex. Science 1991; 251:1249–1251.

Morocutti C, Rizzo PA. Evoked Potentials: Neurophysiological and Clinical Aspects. New York: Elsevier, 1985.

Mukta KN, MacLaurin JN, Robinson PA. Theory of corticothalamic brain activity in a spherical geometry: Spectra, coherence, and correlation. Phys Rev E 2017; 96:052410.

Müller EJ, Robinson PA. Quantitative theory of deep brain stimulation of the subthalamic nucleus for the suppression of pathological rhythms in Parkinson's disease. PLoS Comput Biol 2018; 14:e1006217.

Niedermeyer E, Lopes da Silva FH. Electroencephalography: Basic Principles, Clinical Applications, and Related Fields. Baltimore: Williams and Wilkins, 4th ed., 1999.

Nolte J. The Human Brain: An Introduction to its Functional Anatomy. Philadelphia: Mosby Elsevier, 6th ed., 2009.

Norcia AM, Appelbaum LG, Ales JM, Cottereau BR, Rossion B. The steady-state visual evoked potential in vision research: A review. J Vis 2015; 15:1–46.

Nunez PL. The brain wave equation: a model for the EEG. Math Biosci 1974; 21:279–297.

Nunez PL, Cutillo BA. Neocortical Dynamics and Human EEG Rhythms. New York: Oxford University Press, 2nd ed., 1995.

Nunez PL, Srinivasan R. Electric Fields of the Brain: The Neurophysics of EEG. New York: Oxford University Press, 2nd ed., 2006.

Pfefferbaum A, Wenegrat BG, Ford JM, Roth WT, Kopell BS. Clinical application of the P3 component of event-related potentials. II. Dementia, depression and schizophrenia. Electroencephalogr Clin Neurophysiol 1984; 59:104–124.

Phyllis JW. The Pharmacology of Synapses. Oxford: Pergamon Press, 1970.

Pikovsky A. Synchronization: A Universal Concept in Nonlinear Sciences. New York: Cambridge, 2003.

Purves D, George J, Fitzpatrick D, Hall WC, LaMantia AS, White LE. Neuroscience. Massachusetts: Sinauer Associates, 5th ed., 2012.

Rager G, Singer W. The response of cat visual cortex to flicker stimuli of variable frequency. Eur J Neurosci 1998; 10:1856–1877.

Regan D. Human Brain Electrophysiology. New York: Elsevier, 1989.

Rennie CJ, Robinson PA, Wright JJ. Effects of local feedback on dispersion of electrical waves in the cerebral cortex. Phys Rev E 1999; 59:3320–3329.

Rennie CJ, Robinson PA, Wright JJ. Unified neurophysical model of EEG spectra and evoked potentials. Biol Cybern 2002; 86:457–471.

Rennie CJ, Wright JJ, Robinson PA. Mechanisms of cortical electrical activity and emergence of gamma rhythm. J Theor Biol 2000; 205:17–35.

Roberts JA, Robinson PA. Modeling absence seizure dyamics: Implications for basic mechanisms and measurement of thalamocortical and corticothalamic latencies. J Theor Biol 2008; 253:189–201.

Roberts JA, Robinson PA. Quantitative theory of driven nonlinear brain dynamics. NeuroImage 2012; 62:1947–1955.

Robinson PA. Neurophysical theory of coherence and correlations of electroencephalographic and electrocorticographic signals. J Theor Biol 2003; 222:163–175.

Robinson PA, Chen P, Yang L. Physiologically based calculation of steady-state evoked potentials and cortical wave velocities. Biol Cybern 2008; 98:1–10.

Robinson PA, Loxley PN, O'Connor SC, Rennie CJ. Modal analysis of corticothalamic dynamics, electroencephalographic spectra, and evoked potentials. Phys Rev E 2001a; 63:041909.

Robinson PA, Rennie CJ, Rowe DL. Dynamics of large-scale brain activity in normal arousal states and epileptic seizures. Phys Rev E 2002; 65:041924.

Robinson PA, Rennie CJ, Rowe DL, O'Connor SC. Estimation of multiscale neurophysiologic parameters by electroencephalographic means. Hum Brain Mapp 2004; 23:53–72.

Robinson PA, Rennie CJ, Rowe DL, O'Connor SC, Gordon E. Multiscale brain modelling. Phil Trans Roy Soc B 2005; 360:1043–1050.

Robinson PA, Rennie CJ, Rowe DL, O'Connor SC, Wright JJ, Gordon E, Whitehouse RW. Neurophysical modeling of brain dynamics. Neuropsychopharmacol 2003a; 28:S74–S79.

Robinson PA, Rennie CJ, Wright JJ. Propagation and stability of waves of electrical activity in the cerebral cortex. Phys Rev E 1997; 56:826–840.

Robinson PA, Rennie CJ, Wright JJ, Bahramali H, Gordon E, Rowe DL. Prediction of electroencephalographic spectra from neurophysiology. Phys Rev E 2001b; 63:021903.

Robinson PA, Rennie CJ, Wright JJ, Bourke PD. Steady states and global dynamics of electrical activity in the cerebral cortex. Phys Rev E 1998; 58:3557–3571.

Robinson PA, Roy N. Neural field theory of nonlinear wave-wave and wave-neuron processes. Phys Rev E 2015; 91:062719.

Robinson PA, Whitehouse RW, Rennie CJ. Nonuniform corticothalamic continuum model of electroencephalographic spectra with application to split-alpha peaks. Phys Rev E 2003b; 68:021922.

Rowe DL, Robinson PA, Rennie CJ. Estimation of neurophysiological parameters from the waking EEG using a biophysical model of brain dynamics. J Theor Biol 2004; 231:413–433.

Sanz-Leon P, Robinson PA, Knock SA, Drysdale PM, Abeysuriya RG, Fung FK, Rennie CJ, Zhao X. NFTsim: Theory and Simulation of Multiscale Neural Field Dynamics. PLoS Comput Biol 2018; 14:e1006387.

Schomer DL, Lopes da Silva FH. Niedermeyer's electroencephalography: basic principles, clinical applications, and related fields. Lippincott Williams and Wilkins, 6th ed., 2012.

Sherman SM, Guillery RW. Exploring the Thalamus. New York: Academic Press, 1st ed., 2001.

Siegel A, Sapru HN. Essential Neuroscience. Philadelphia: Lippincott Williams and Wilkins, 1st ed., 2006.

Stam CJ. Nonlinear dynamics analysis of EEG and MEG: Review of an emerging field. Clin Neurophysiol 2005; 116:2266–2301.

Stam CJ, Pijn JPM, Suffczynski P, Lopes da Silva FH. Dynamics of the human alpha rhythm: evidence for non-linearity? Clin Neurophysiol 1999; 110:1801–1813.

Stephan KE, Kasper L, Harrison LM, Daunizeau J, den Ouden HEM, Breakspear M, Friston KJ. Nonlinear dynamic causal models for fMRI. Neuroimage 2008; 42:649–662.

Steriade M. The corticothalamic system in sleep. Front Biosci 2003; 8:d878–d899.

Steriade M, Deschênes M, Domich L, Mulle C. Abolition of spindle oscillations in thalamic neurons disconnected from nucleus reticularis thalami. J Neurophysiol 1985; 54:1473–1497.

Steriade M, Gloor P, Llinás RR, Lopes da Silva FH, Mesulam MM. Basic mechanisms of cerebral rhythmic activities. Electroencephalogr Clin Neurophysiol 1990; 76:481–508.

Steyn-Ross ML, Steyn-Ross DA, Sleigh JW, Whiting DR. Theoretical predictions for spatial covariance of the electroencephalographic signal during the anesthetic-induced phase transition: Increased correlation length and emergence of spatial self-organization. Phys Rev E 2003; 68:021902.

Steyn-Ross ML, Steyn-Ross DA, Sleigh JW, Wilcocks LC. Toward a theory of the general-anesthetic-induced phase transition of the cerebral cortex. I. A thermodynamics analogy. Phys Rev E 2001; 64:011917.

Steyn-Ross ML, Steyn-Ross DA, Sleigh JW, Wilson MT, Wilcocks LC. Proposed mechanism for learning and memory erasure in a white-noise-driven sleeping cortex. Phys Rev E 2005; 72:061910.

Teplan M. Fundamentals of EEG Measurement. Meas Sci Rev 2002; 2:1–11.

Townsend RE, Lubin A, Naitoh P. Stabilization of alpha frequency by sinusoidally modulated light. Electroencephalogr Clin Neurophysiol 1975; 39:515–518.

van Albada SJ, Kerr CC, Chiang AKI, Rennie CJ, Robinson PA. Neurophysiological changes with age probed by inverse modeling of EEG spectra. Clin Neurophysiol 2010; 121:21–38.

van der Tweel LH, Spekreijse H. Signal transport and rectification in the human evoked-response system. Ann N Y Acad Sci 1969; 156:678–695.

van der Tweel LH, Verduyn Lunel HFE. Human visual responses to sinusoidally modulated light. Electroencephalogr Clin Neurophysiol 1965; 18:587–598.

Vespa PM, Nenov V, Nuwer MR. Continuous EEG Monitoring in the Intensive Care Unit: Early Findings and Clinical Efficacy. J Clin Neurophysiol 1999; 16:1–13.

Vialatte FB, Maurice M, Dauwels J, Cichocki A. Steady-state visually evoked potentials: focus on essential paradigms and future perspectives. Prog Neurobiol 2010; 90:418–438.

Walsh P, Kane N, Butler S. The clinical role of evoked potentials. J Neurol Neurosurg Psychiatry 2005; 76:ii16–ii22.

Wendling F, Bartolomei F, Bellanger JJ, Chauvel P. Epileptic fast activity can be explained by a model of impaired GABAergic dendritic inhibition. Eur J Neurosci 2002; 15:1499–1508.

Wendling F, Bellanger JJ, Bartolomei F, Chauvel P. Relevance of nonlinear lumped-parameter models in the analysis of depth-EEG epileptic signals. Biol Cybern 2000; 83:367–378.

Whitham GB. Linear and Nonlinear Waves. New York: Wiley, 1974.

Wilson HR, Cowan JD. Excitatory and inhibitory interactions in localized populations of model neurons. Biophys J 1972; 12:1–24.

Wilson HR, Cowan JD. A mathematical theory of the functional dynamics of cortical and thalamic nervous tissue. Kybernetik 1973; 13:55–80.

Wright JJ, Liley DTJ. A millimetric-scale simulation of electrocortical wave dynamics based on anatomical estimates of cortical synaptic density. Netw: Comput Neural Syst 1994; 5:191–202.

Wright JJ, Liley DTJ. Dynamics of the brain at global and microscopic scales: Neural networks and the EEG. Behav Brain Sci 1996; 19:285–320.